STUDIES OF ELECTRONIC STRUCTURE AND THERMAL PROPERTIES OF HEUSLER THERMOELECTRIC MATERIALS

Ph.D. THESIS

by

MOHD ZEESHAN

DEPARTMENT OF CHEMISTRY
INDIAN INSTITUTE OF TECHNOLOGY ROORKEE
ROORKEE-247 667 (INDIA)
OCTOBER, 2018

STUDIES OF ELECTRONIC STRUCTURE AND THERMAL PROPERTIES OF HEUSLER THERMOELECTRIC MATERIALS

A THESIS

Submitted in partial fulfilment of the requirements for the award of the degree

of

DOCTOR OF PHILOSOPHY

in

CHEMISTRY

by

MOHD ZEESHAN

DEPARTMENT OF CHEMISTRY
INDIAN INSTITUTE OF TECHNOLOGY ROORKEE
ROORKEE-247 667 (INDIA)
OCTOBER, 2018

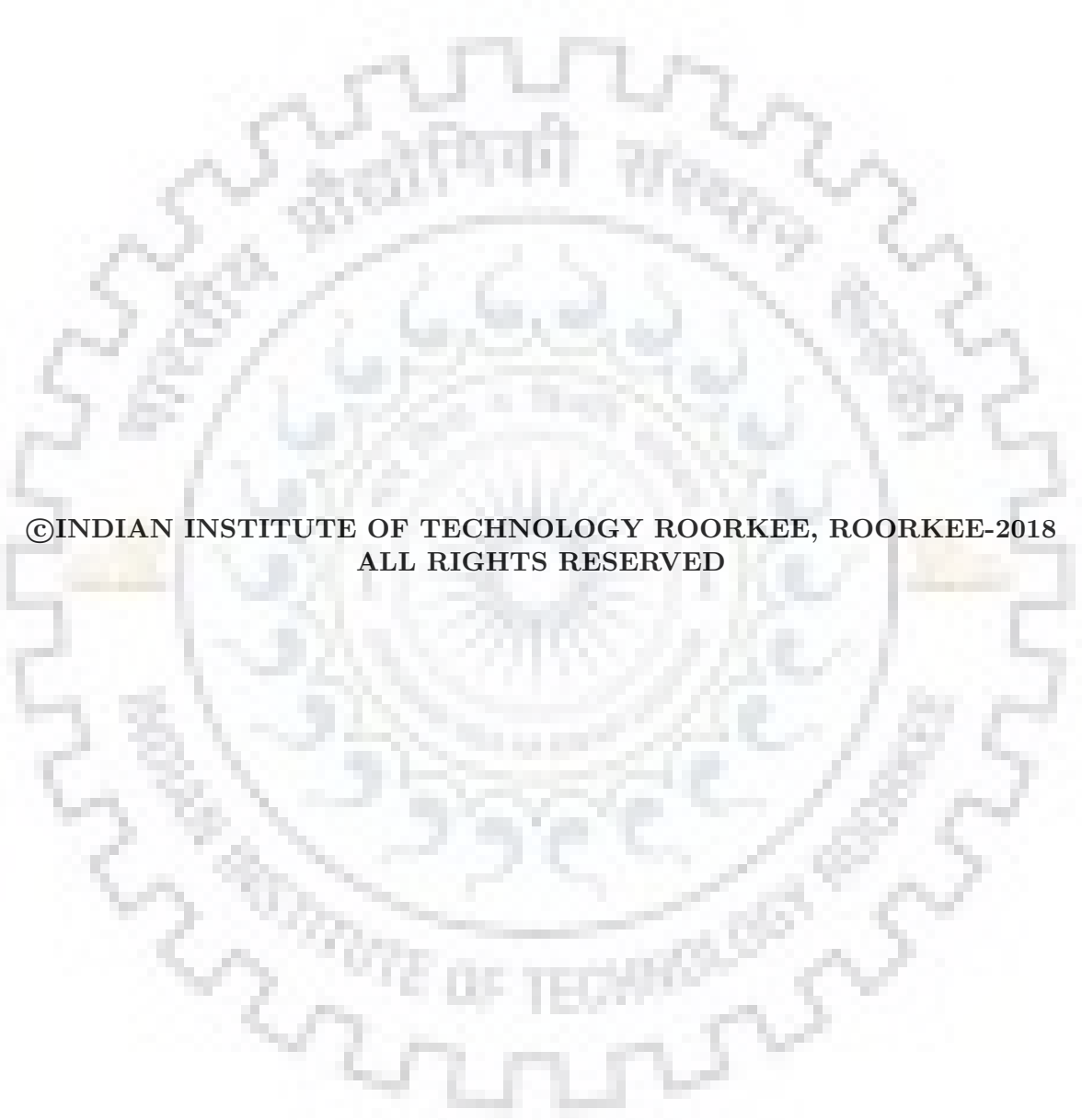

INDIAN INSTITUTE OF TECHNOLOGY ROORKEE
ROORKEE

CANDIDATE'S DECLARATION

I hereby certify that the work being presented in the current thesis entitled **"STUDIES OF ELECTRONIC STRUCTURE AND THERMAL PROPERTIES OF HEUSLER THERMOELECTRIC MATERIALS"** in partial fulfilment of the requirement for the award of the Degree of Doctor of Philosophy and submitted in the Department of Chemistry of the Indian Institute of Technology Roorkee, Roorkee, is an authentic record of my own work during the period from July, 2013 to October, 2018 under the supervision of Dr. Hem C. Kandpal, Assistant Professor, Department of Chemistry, Indian Institute of Technology Roorkee, Roorkee.

The matter presented in this thesis has not been submitted by me for award of any other degree of this or any other Institute.

(MOHD ZEESHAN)

This is to certify that above statement made by the candidate is correct to the best of my knowledge.

(Hem C. Kandpal)
Supervisor

The Ph.D. Viva-Voce examination of Mr. **Mohd Zeeshan**, Research Scholar, has been held on April 16, 2019.

Chairperson, SRC **External Examiner**

This is to certify that the student has made all the corrections in the thesis.

Supervisor **Head of the Department**
Dated:

Thesis advisor

Dr. Hem C. Kandpal

Author

Mohd Zeeshan

STUDIES OF ELECTRONIC STRUCTURE AND THERMAL PROPERTIES OF HEUSLER THERMOELECTRIC MATERIALS

Abstract

Thermoelectricity can address the global energy crisis and climate changes by directly converting the waste heat into electricity. Despite the extensive research, Heusler alloys as potential thermoelectric materials are yet to meet the threshold efficiency for commercialization. Therefore, in addition to improving the existing materials, the search for new potential Heusler alloys is of key importance – the motivation of the thesis. In search of new prospects for thermoelectric materials, using *ab initio* calculations, semiclassical Boltzmann transport theory, and constant relaxation time approach, the systematic investigation of the ground state properties, electronic structure, and electrical and thermal transport properties of six cobalt-based (CoVSn, CoNbSn, CoTaSn, CoCrIn, CoMoIn, and CoWIn), two iron-based (FeTaSb and FeMnTiSb) Heusler alloys, and a special derivative of half-Heusler alloys LiZnX (X = N, P, As, Sb, and Bi) has been carried out. Further, the polytypism and its impact on transport properties have been questioned in LiZnX family.

The investigations on 18 valence electron count cobalt-based systems revealed some interesting features. It was found that all the cobalt-based systems (except metallic CoCrIn) were promising as p-type thermoelectric material and more competitive than the well-known CoTiSb. The proposed doping levels in all the cases are quite pragmatic and could be realized experimentally. This assures that the calculated numbers are not entirely hypothetical but achievable in reality. In particular, the better thermoelectric properties of p-type CoNbSn, as compared to the existing n-type, can be seen as an important implication in this class. This would motivate the experimentalists to consider the hole-doped compositions of CoNbSn. Further, the electronic band structure of CoCrIn indicates the possiblity

of a topological insulator, thus, may interest researchers.

In addition to cobalt-based half-Heusler alloys, the two iron-based Heusler alloys, FeTaSb and FeMnTiSb were found to be promising thermoelectric candidates. The 18 valence electron count FeTaSb was expected to show the similar properties as that of FeNbSb on account of similar sizes of Nb and Ta. Indeed, it was found that n-type FeTaSb can actually complement the best performing half-Heusler alloy FeNbSb. Whereas the low-cost FeMnTiSb was found to have comparable thermoelectric properties on either n-type or p-type doping. Thus, the FeMnTiSb can be used as both n-type and p-type legs in a thermoelectric module, which is rare. As 24-valence electron count Heusler alloys have not been much explored in the context of thermoelectricity, the findings of FeMnTiSb could be an interesting perspective.

Most interesting features were obtained in a special derivative of half-Heusler alloys, LiZnX systems. The first instance of polytypism was recently reported in LiZnSb system. In order to understand the driving force behind polytypism and its possible existence in other Li-based systems with particular emphasis on thermoelectric properties, the LiZnX (X = N, P, As, Sb, and Bi) systems were investigated in cubic and hexagonal symmetry. Interestingly, the hitherto hexagonal LiZnBi was found to be more stable in cubic geometry. Though metallic, the band structure of cubic-LiZnBi indicates the topological properties. Nevertheless, the cubic-hexagonal phase transition was not limited to LiZnBi but could be achieved in other systems on the application of hydrostatic and internal pressure. Further, the transport properties were improved on cubic-hexagonal phase transition in LiZnX family which validates that polytypism may affect better thermoelectric performance. The most promising system turned out to be LiZnSb as the figure of merit values were quite impressive in both cubic and hexagonal symmetry. Since the required pressure for cubic-hexagonal phase transition in LiZnSb is 4.3 GPa, the cubic-hexagonal phase transition might be possible in realistic application conditions. However, the high efficiency of both cubic and hexagonal LiZnSb ensures that the overall efficiency of the device is not

affected.

All in all, some of the findings of the present work can be seen as the significant contribution toward the thermoelectric research and will motivate researchers for their experimental realization in the quest of materials with the better figure of merit.

Contents

List of Figures

List of Tables

Publications

1. Mohd Zeeshan, Harish K. Singh, Jeroen van den Brink, and Hem C. Kandpal
   Ab initio design of new cobalt-based half-Heusler materials for thermoelectric applications
   Phys. Rev. Materials **1** (2017) 075407.

2. Mohd Zeeshan, Jeroen van den Brink, and Hem C. Kandpal
   Hole-doped cobalt-based Heusler phases as prospective high-performance high-temperature thermoelectrics
   Phys. Rev. Materials **1** (2017) 074401.

3. Mohd Zeeshan, Tashi Nautiyal, Jeroen van den Brink, and Hem C. Kandpal
   FeTaSb and FeMnTiSb as promising thermoelectric materials: An *ab initio* approach
   Phys. Rev. Materials **2** (2018) 065407.

4. Mohd Zeeshan*, Uday Chopra*, Shambhawi Pandey, Harish K. Singh, Jeroen van den Brink, and Hem C. Kandpal
   Polytypism at its best: improved thermoelectric performance in Li-based Nowotony-Juza phases
   Phys. Rev. Materials (submitted) 2018.

5. Sapna Singh*, Mohd Zeeshan*, Jeroen van den Brink, and Hem C. Kandpal
   First-principles investigations of orthorhombic-cubic phase transition and its effect on thermoelectric properties in cobalt-based ternary alloys
   Phys. Rev. Materials (submitted) 2019.

6. Sapna Singh*, Mohd Zeeshan*, Jeroen van den Brink, and Hem C. Kandpal
   Ab initio study of Bi-based half Heusler alloys as potential thermoelectric prospects
   Phys. Rev. Materials (submitted) 2019.

Acknowledgments

Firstly, I would like to express my sincere gratitude to my supervisor Dr. Hem C. Kandpal. I am really thankful to him for his constant motivation and unwavering support throughout this period. Without his guidance and sincere efforts, this thesis would not have been possible. Not only I learned a new aspect of science and working techniques, but his suggestions and advice had been really helpul in my personal life also. I am highly indebted to him. Overall, it was a wonderful experience to work with him.

I would like to thanks my committee members Dr. P. Jeevanandam, Dr. T. K. Mandal, and B. S. S. Daniel for their kind support and valuable guidance from time to time. My sincere thanks also go to Prof. G. Fecher, Max Planck Institute for Chemical Physics of solid, for his expert opinions and suggestions regarding computational techniques and modern research in thermoelectrics. I extend my thanks to Prof. J. van den Brink, IFW Dresden, for his valuable suggestions in all my publications. Further, I would like to thanks Prof. J. van den Brink and Prof. K. Nielsch, for providing me an opportunity to explore the research opportunities at IFW Dresden.

Lastly, I thank all my colleagues for their help and support in the laboratory. In particular, I thank Uday, Harish, and Sapna for assistance in theoretical work, and Haseeb for assistance in experimental works.

Mohd Zeeshan
October, Roorkee

Dedicated to my family

Chapter 1

Introduction

1.1 Motivation

The world's energy consumption is increasing day by day and likely to become manifold by the end of the century [164]. Currently, around 90% of world's energy demand is met by the combustion of fossil fuels. However, the growing population's demand and enormous exploitation of fossils are alarming. With the present rate of consumption and limited resources, the fossils are not going to last forever. Moreover, the combustion of fossils has the adverse impact on the environment and may lead to irreversible climate change and global warming. The current energy crisis and global climate change renewed the interest of researchers in alternate sources of power generation and developing new technologies [160]. Whereas the potential alternate sources of power generation are hydrogen gas, tidal energy, biomass energy to name a few, the new promising technologies emerged are hydrogen storage materials, solar cells, and lithium ion batteries etc. One promising technology to emerge out in 19th century was thermoelectricity.

Thermoelectricity is the direct conversion of heat into electricity and vice versa. The significance of thermoelectric (TE) devices lies in the consumption of waste heat into the useful form of energy [120, 4]. Around 66% of the energy which we consume is lost in the form of waste heat. This way the fuel efficiency is reduced and waste heat also contribute to climate changes [34, 69]. By utilizing the waste heat, we can greatly improve the fuel efficiency which will lessen the burden on existing sources of power generation. Further, the waste heat will not be dissipated into the environment. Thus, thermoelectricity offers a clean alternative source of power generation by utilizing the waste heat into electricity, Fig. 1.1 [117]. TE devices have no movable parts, compact in design, and easily scalable [131, 55, 33]. These devices can be used in automobiles or power plants to tap the waste

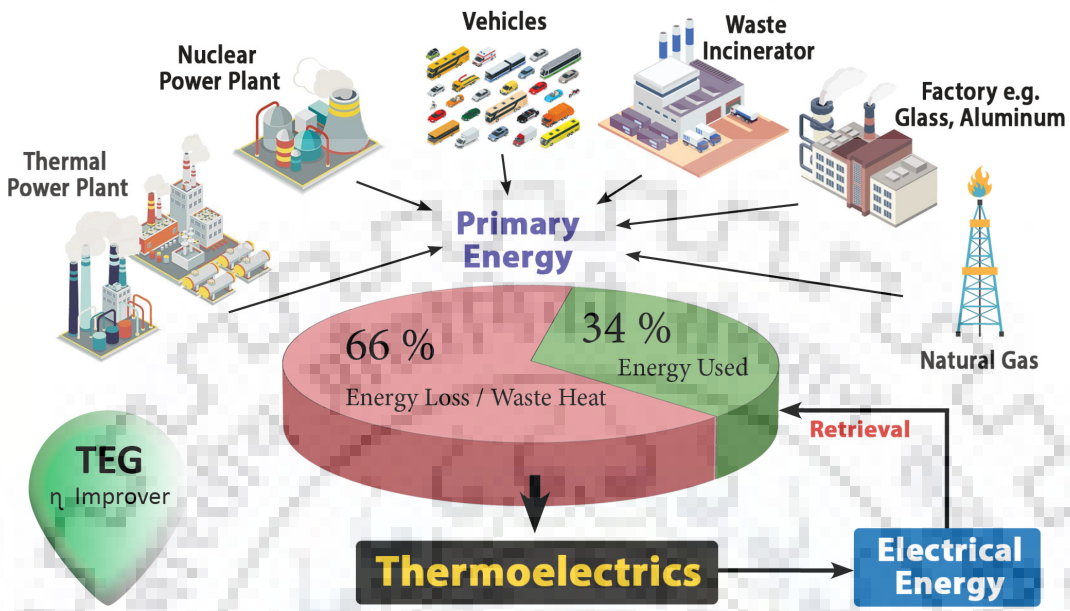

Figure 1.1: Waste heat utilization by thermoelectricity.
Source: https://prometeon.it/advanced-clean-technologies-tech-chip/

heat into electricity, as power sources in space exploration, for portable applications such as wrist watches, and military operations [34].

1.2 Brief History

In 1821, a German physicist Thomas Johann Seebeck, for the first time demonstrated the TE effect [123]. He observed that if two dissimilar metals are connected together to make a circuit and the ends are kept at different temperatures, a potential difference will be generated which produces electric current. The phenomenon is known as Seebeck effect. The potential difference (ΔV) created when the two junctions are kept at different temperatures T_1 and T_2 ($T_2 > T_1$) is given by

$$\Delta V = S\Delta T \tag{1.1}$$

where the constant of proportionality is known as Seebeck coefficient. Later, in 1834, a French watchmaker and part-time physicist Jean Charles Athanase Peltier discovered an exactly opposite behavior [111]. He found that if current, I, passes through a circuit of two dissimilar metals, heat will be absorbed or liberated at the two junctions. The heat liberated or absorbed, Q, at the junctions is proportional to the current passed and given by

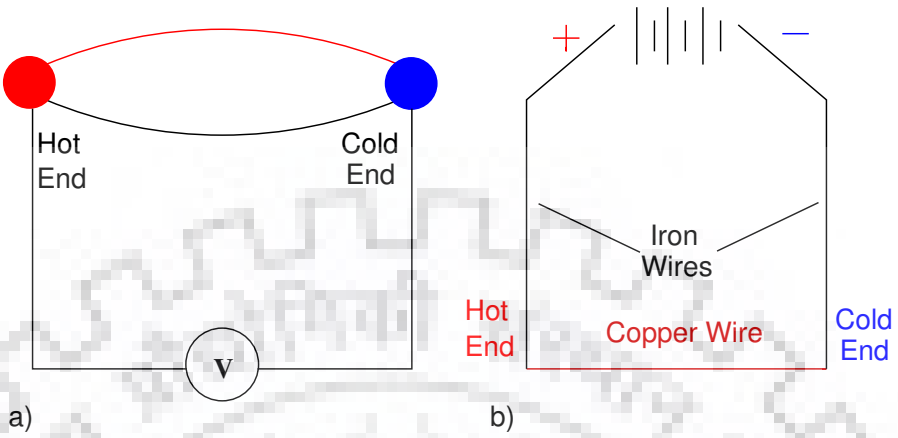

Figure 1.2: Two fundamental thermoelectric effects: a) Seebeck and b) Peltier effect.

$$Q = \pi I \tag{1.2}$$

where the constant π is known as Peltier coefficient. Seebeck effect concerns the generation of potential difference by creating a temperature difference whereas in Peltier effect heat is absorbed or liberated by application of current Fig. 1.2. In 1851, William Thomson established that the two effects are connected to each other and proposed a third TE effect [133]. He showed that a temperature gradient in a material will result in heat absorption or evolution when current passes through it. It was Edmund Altenkirch, in 1909, who calculated the efficiency of a TE device which was later put on a systematic footing by Abram Fedorovich Ioffe [1]. Ioffe proposed that the performance of a TE material is given by a dimensionless parameter called the figure of merit, ZT, i.e.,

$$ZT = S^2\sigma T/\kappa \tag{1.3}$$

where S is Seebeck coefficient, σ is electrical conductivity, and κ is thermal conductivity. Ioffe further recommended the use of heavily doped semiconductors to attain the best efficiency of TE materials [140]. During 1920-1970, TE was mainly explored in the context of cooling and power generation for military uses. The initial TE devices were used in the form of heat pumps for the cooling purpose (Peltier Effect) where efficiency was not of much concern. In 1961, in a major breakthrough, the National Aeronautics and Space Administration for the first time utilized the TE technology for space exploration. Thereafter, the technology found its place in conventional industries and found applications in wrist watches, diode lasers, cooling and heating in trains, automobiles, defense, and many others. It was speculated that TE materials may soon replace the heat engines and ther-

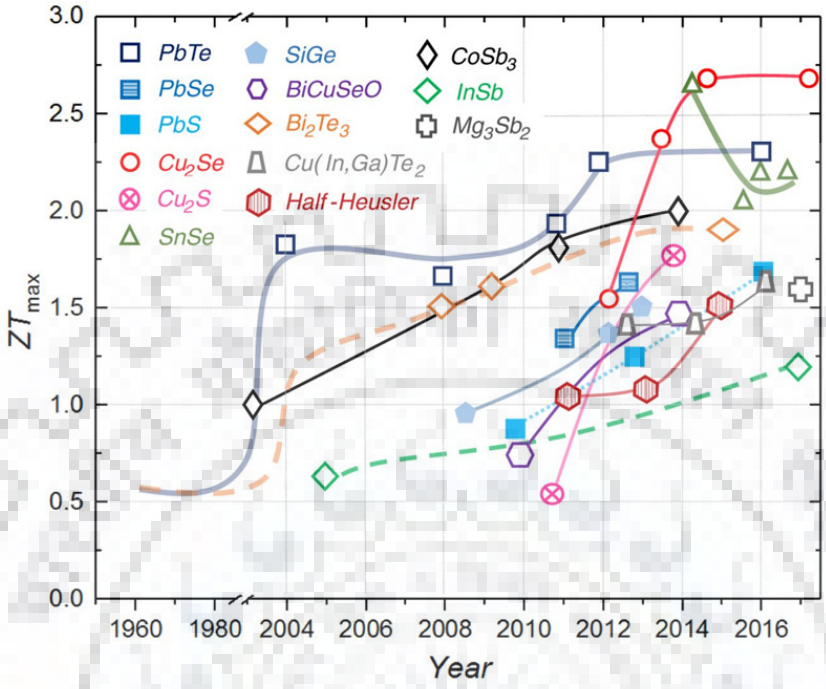

Figure 1.3: The ZT values over the years of different thermeoelectric materials [61].

moelectricity became a new fascinating area for researchers. Unfortunately, the progress was not substantial and it was assumed that upper limit of ZT was close to 1. This was the major setback and led to a dull phase in the history of thermoelectricity. However, the interest in TE materials was rekindled with the new set of ideas and exploration of new materials [34, 130]. The prime interest was somehow to maximize the figure of merit. New materials were being explored, however, the question arises what are the best prospects for a higher TE efficiency. What kind of materials can be the best choices? To analyze this, the parameters governing the figure of merit and accordingly the most suitable materials are discussed in the next section.

1.3 Thermoelectric Figure of Merit, *ZT*

According to Eq. 1.3, for good performance of a TE material, the numerator part $S^2\sigma$, also called as power factor (PF), should be maximum whereas the denominator, i.e., thermal conductivity should be minimum. Theoretically, there is no upper limit on the ZT value, however, the ZT values reported till date are less than 3, as shown in Fig. 1.3 [61, 101, 118]. The limited efficiency of TE materials can be attributed to the conflicting parameters governing the figure of merit, i.e., S, σ, and κ. Ideally, S and σ should be increased and κ should be lowered at the same time. However, practically it is not an

easy task since all three parameters are coupled with each other [126, 131]. If one tends to improve the σ, the values of κ may also increase. Therefore, the prima facie is to search materials which have high Seebeck coefficient, electrical conductivity and at the same time possess minimum thermal conductivity. In this regard, the parameters ranking figure of merit and their numbers for different type of materials namely metals, semiconductors, and insulators are discussed below.

1.3.1 Seebeck Coefficient

The Seebeck coefficient can be considered as the heat per carrier over temperature. In case of metals, the heat carrier is the product of electronic specific heat and temperature which is divided by number of charge carriers and can be given as

$$S \approx \left(\frac{k_B}{e}\right)\frac{k_B T}{E_F} \tag{1.4}$$

where k_B is Boltzmann constant, e is the charge of an electron, T is the temperature, and E_F is the Fermi energy. The value of k_B/e is around 87 μV K^{-1} and represent the Seebeck coefficient of the classical electron gas. Typically, the values of Seebeck coefficient of metals lies in the range of 1-10 μV K^{-1}. In case of semiconductors, the Seebeck coefficient is given by

$$S \approx \left(\frac{k_B}{e}\right)\frac{E_g}{k_B T} \tag{1.5}$$

because charge carriers are first needed to be excited across the band gap E_g. Here, the Seebeck coefficient values are higher than $k_B/e \approx 87$ μV K^{-1}. Since the semiconductors can show both electron (e) and hole conductivity (p), the average value of Seebeck coefficient is given by

$$S \approx \frac{S_e\sigma_e + S_p\sigma_p}{\sigma_e + \sigma_p} \tag{1.6}$$

The Seebeck coefficient values in the range of 150-250 μV K^{-1} are considered to be good for an efficient TE performance [139].

1.3.2 Electrical Conductivity

The electrical conductivity of a material is given by

$$\sigma = ne\mu \tag{1.7}$$

where n is the charge carrier density, e is the electronic charge, and μ is the mobility of charge carriers. The mobility of charge carriers further depends on average relaxation time τ and effective mass m_e of charge carriers by the relation

$$\mu = \frac{e\tau}{m_e} \tag{1.8}$$

In order to have high electrical conductivity, a material should have high carrier density and low effective mass of charge carriers. The metals have a high electrical conductivity of the order of 10^6 S cm^{-1} because of a large number of charge carriers present, i.e., $n \approx 10^{22}$ cm^{-3}. For semiconductors, the charge carriers are required to be excited across the band gap. Thus, to achieve high electrical conductivity in semiconductors it is desirable to have either low band gap ($E_g < k_BT$) or high mobility of charge carriers. A very small band gap ($E_g < k_BT$) ensures the excitation of more number of charge carriers. The electrical conductivity of semiconductors lies in the range of 10^{-4}-10^4 S cm^{-1}. For a good TE performance, the values of electrical conductivity should be of the order of 10^4 S cm^{-1} [139].

1.3.3 Thermal Conductivity

Thermal conductivity, κ, comprises two components, one is electronic and other is lattice component. The electronic thermal conductivity, κ_e, comes from the movement of electrons in the lattice whereas the lattice part, κ_l, stems from the lattice vibrations, also called as phonons.

$$\kappa = \kappa_e + \kappa_l \tag{1.9}$$

According to Wiedemann-Franz relation, the electrical conductivity and thermal conductivity are related by the expression

$$\kappa_e = L_0 \sigma T \tag{1.10}$$

where L_0 is the Lorentz number. For κ_e and σ are tied to each other, as discussed above, any increase in the value of κ_e will also be reflected in σ whereas lattice thermal conductivity, κ_l, is given by

$$\kappa_l \approx v_s C L_{ph} \tag{1.11}$$

where v_s is the sound velocity, C is the heat capacity and L_{ph} is the mean free path of phonons. At temperatures higher than 300 K, the sound velocity and heat capacity

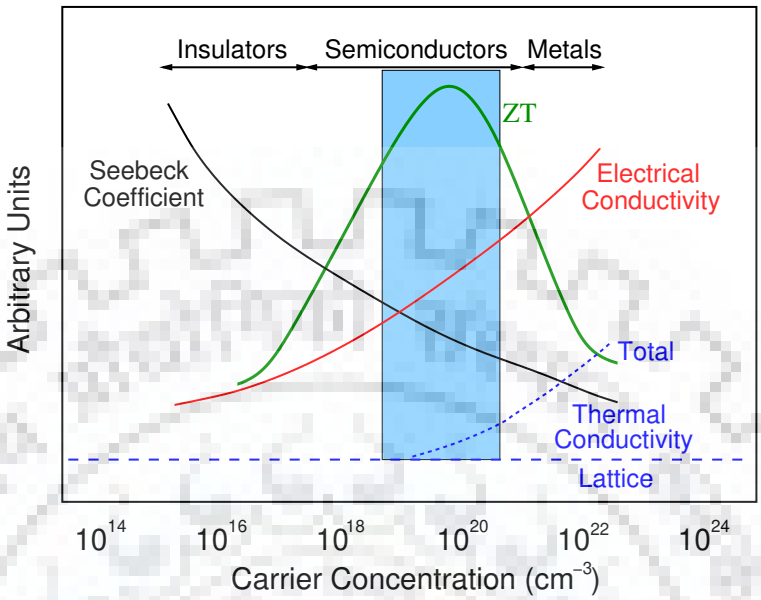

Figure 1.4: A comparison of the figure of merit of metals, semiconductors, and insulators as a function of carrier concentration [38].

are temperature independent and behave differently with different materials. Hence, the thermal conductivity is predominantly determined by the mean free path of phonons. For good TE performance, the values of $\kappa < 2$ W m^{-1} K $^{-1}$ are considered to be good [139]. Overall, taking the Seebeck coefficient, electrical conductivity, and thermal conductivity of different materials into consideration, a comparison of TE efficiency of metals, insulators, and semiconductors is depicted in Fig. 1.4.

Insulators have highest Seebeck coefficient and lowest thermal conductivity, however, their low electrical conductivity reduces their TE performance. Metals have high electrical conductivity but low Seebeck coefficient values and their thermal conductivity is also high whereas the semiconductors have moderate values of Seebeck coefficient and electrical conductivity but their low thermal conductivity in comparison to metals make them most favorable choices for better TE efficiency. Ioffe also recommended the use of semiconductors for attaining high values of ZT. However, for commercialization of TE materials, there was a dire need to improve the efficiency of a TE device. The various approaches to maximize the efficiency of TE materials are presented in next section.

1.4 Ways To Improve ZT

It is established in the previous section that the semiconductors are the best TE candidates, the further investigations for higher ZT are governed by a number of factors.

The two most important approaches to obtain high ZT values in existing materials and designing new potential TE materials are briefly discussed here.

1.4.1 Phonon-Glass:Electron-Crystal Approach

Slack, in 1995 [128, 129], proposed the phonon-glass electron-crystal (PGEC) concept. He suggested that to attain a high ZT, a material should have electronic properties as that of a crystal and thermal properties similar to an amorphous glass-like material. The characteristics of such features demand narrow band gap semiconductors with high mobility of charge carriers and minimum thermal conductivity. The requisite for high mobility is the small electronegativity difference between the constituent elements. The heavy atoms from the periodic table such as Bi, Te, Sb, Sn, Se, Ge are most likely choices to fulfill Slack's criteria. The electronegativity difference between them is small and most of their compounds possess narrow band gaps [139]. Slack further postulated that a material in line with PGEC concept would have $ZT \sim 4$ in the temperature range 77-300 K [129]. Ideally, it's not easy to always fulfill the Slack's hypothesis. Therefore, an alternate but effective strategy is to minimize the thermal conductivity of the materials having good power factor.

1.4.2 Minimize Thermal Conductivity

Much modern-day research is based on minimizing the thermal conductivity of materials with a good power factor value. As discussed, semiconductors are the best choice of TE materials and the major contribution to their κ comes from lattice contribution, i.e., phonons. Hence, it is more beneficial to aim at the lattice thermal conductivity in semiconductors. According to equation 1.11, the κ_l depends upon sound velocity, heat capacity, and phonon mean free path. The mean free path in a crystal depends upon three mechanisms namely phonon-phonon interaction, phonon-impurity interaction, and phonon-boundaries of crystal. At low temperatures (T < 300 K), the specific heat capacity decreases with temperature. Only phonon-boundary scattering is the dominant mechanism where the mean free path of phonons is equivalent to the interatomic distance and almost independent of temperature. Thus, the κ depends entirely on heat capacity in the low-temperature region. However, in the high-temperature range (T > 300 K), the sound velocity and heat capacity are independent of material and temperature according to Dulong-Petit's law. Thus, the contributing factor toward κ_l is mean free path of phonon. The dominant process at high temperatures is the phonon-phonon mechanism. The various strategies adopted to minimize this mechanism involves scattering of phonons by mass fluctuations, grain bound scattering, rattler atoms, and nanostructuring. Over the years, the thermal

conductivity has been significantly reduced by these approaches. The phonon-impurity interactions are maximum when more number of impurities are present or introduced into the crystal through doping [139].

1.4.3 Materials of Interest

The consideration of these two approaches suggests that a potential TE material should comprise at least three atoms. The two atoms shall form the covalent framework facilitating the high mobility of charge carriers whereas the third atom should occupy voids or interstitial spaces in order to scatter the phonons by introducing disorder or as rattlers. Overall, the material should have optimal carrier concentration with high mobility and low thermal conductivities. These conditions are best found in intermetallic compounds. Based on these guidelines, i) the existing potential TE materials were tuned by doping or alloying to minimize their thermal conductivity. For instance, Si and Ge have a high mobility of charge carriers but their κ values are also quite high. However, the alloys of Si and Ge have significantly lower thermal conductivities and improved ZT values. Historically, the most studied Bi_2Te_3 and PbTe were reported to have high ZT values by either hole or electron doping. (ii) the new potential classes of TE materials were explored. Some of the potential classes of TE materials explored over the years include complex inorganic structures such as $CsBi_4Te_6$ [26] and $AgPb_mMnTe_{2+m}$ (M = Sb, Bi) [74], crystal structures with rattler atoms, e.g., chalcogenides [120], skutterudites [102], oxides [122], antimonides [12], half-Heusler alloys [18], thin films [146], and nanostructures [11]. Each class has its own merits and demerits. A detailed review of these classes can be seen in a review by T. M. Tritt [139].

The advent of modern ideas and new materials reignited the spark in TE materials and the ZT values have seen a progressive increment over the years, Fig. 1.3. The highest reported ZT value till now is 2.6 [163] in SnSe crystals and considering the growing trend, it is likely to be surpassed in near future. Among the various classes of TE materials, as mentioned above, half-Heusler alloys have gained significant interest in recent years, on which this thesis is based. Therefore, the next section of this chapter is dedicated entirely to this particular class – half-Heusler alloys.

1.5 Half-Heusler Alloys: Potential Thermoelectric Materials

This part of the chapter explains the crystal structure, interesting features, and recent progress in half-Heusler (hH) alloys.

1.5.1 Crystal Structure

In 1903, Fritz Heusler, a German mining engineer, and chemist discovered that Cu_2MnAl behaves like a ferromagnet despite none of the constituent elements is magnetic in nature. Since then, a large number of compounds based on this material are reported and collectively known as Heusler alloys [18]. Heusler alloys can be categorized broadly into three classes depending on their constituents.

I) X_2YZ, full Heusler or $L2_1$ Heusler alloys.

II) XYZ, half-Heusler (hH) or $C1_b$ Heusler alloys.

III) XX′YZ, quaternary Heusler alloys.

where X, X′, Y, comes from the transition metals and Z belongs to the main group elements. In some derivatives of these alloys, Y may also belong to alkali/alkaline or rare earth metals. As all the structures are derived from one family, the understanding of any one of them can easily guide to its other relative. Here, the variants of Heusler alloys are discussed in terms of the hH crystal structure. The hH family crystallizes in cubic $F\bar{4}3m$ (space group 216) symmetry and can be accounted in a number of ways. The simplest illustration of the crystal structure of hH alloys can be visualized as the most electropositive atom, Y, and most electronegative atom, Z, forming a rock salt type sublattice wherein X atoms occupy half of the tetrahedral voids. The Y and Z are situated at (0,0,0) and (1/2, 1/2, 1/2) positions, respectively, while the X atoms at the tetrahedral voids, (1/4, 1/4, 1/4). The other half vacant tetrahedral voids are located at (3/4, 3/4, 3/4) position. In case all the tetrahedral voids are filled by X, the resulting structure is full Heusler. However, if tetrahedral voids are occupied equally by X and X′, the structure is known as quaternary Heusler because of four different constituent elements. A very common viewpoint of the hH crystal structure may also be treated as the stuffed combination of rock salt type and zinc sulfide type sublattice, where YZ form the rock salt structure and covalent zinc sulfide type framework is made by XZ, as depicted in Fig. 1.5 [18].

Interestingly, in some works, the cubic hH alloys were reported to exist in $P6_3/mmc$ ZrBeSi type structure under certain conditions. Noda et al. found a cubic to hexagonal phase transition in CoVSb and FeVSb on the application of high temperature-pressure conditions [106]. In another work, Jodin et al. reported a cubic to hexagonal phase transition in FeVSb near 700 ^{0}C [79]. Some Li-based Nowotny-Juza phases, a special derivative of hH alloys, are known to exist in cubic $F\bar{4}3m$ and hexagonal $P6_3mc$ symmetry. For instance, LiZnN [94], LiZnP [91], and LiZnAs [93] are cubic structures whereas LiZnSb [135] and LiZnBi [134] exist in hexagonal polar $P6_3mc$ LiGaGe type structure. Recently, LiZnSb which exists in hexagonal phase was also synthesized in cubic symmetry [141]. Such ex-

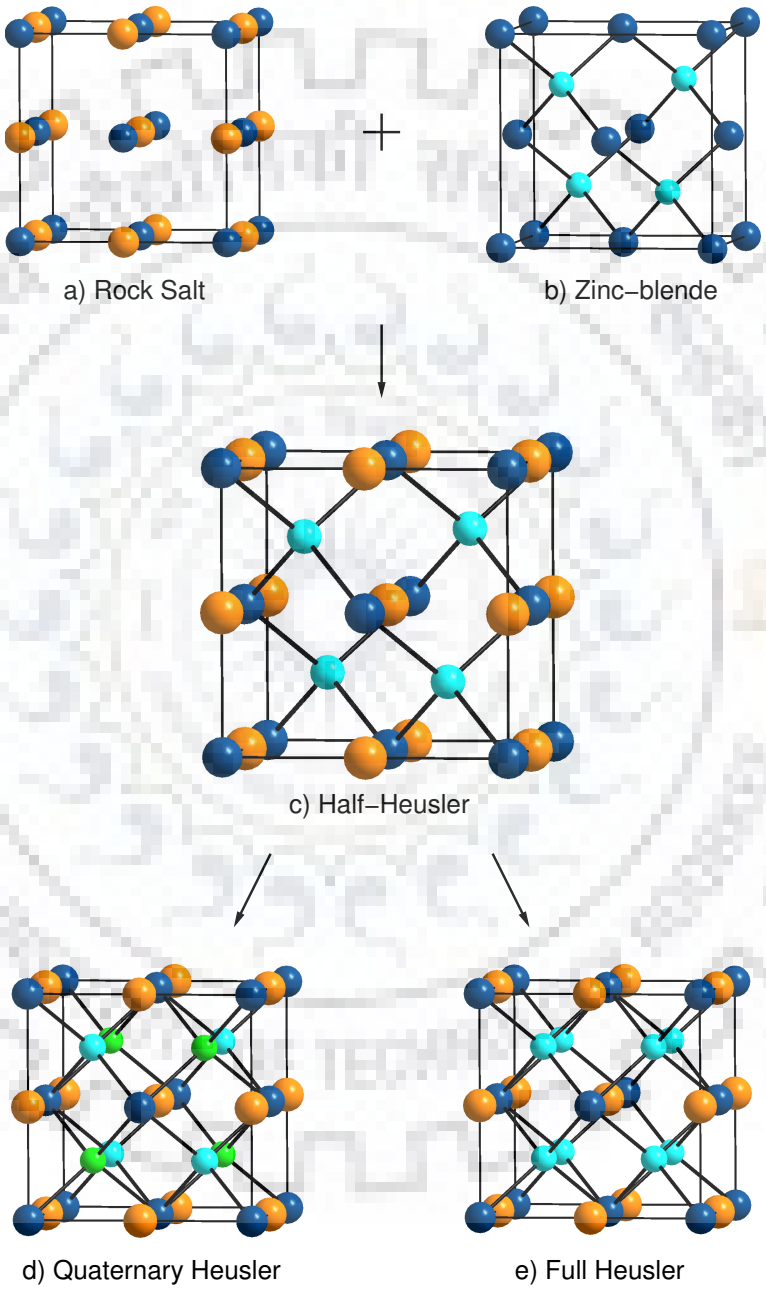

Figure 1.5: The crystal structure of a) Rock salt, NaCl, b) Zinc-blende, ZnS, c) Half-Heusler, d) Quaternary Heusler, and e) Full Heusler alloy.

perimental investigations suggest that cubic and hexagonal variants of hH alloys may be interconvertible provided certain conditions of temperature and pressure. What may be the pertinent condition for these phase transitions? The extended crystal structure of cubic and hexagonal hH alloys, illustrated in Fig. 1.6, reveals that a hexagonal framework is common in all three symmetries. Whereas the hexagonal framework in polar $P6_3mc$ structure is buckled, the hexagonal framework in $P6_3/mmc$ structure is planar. If somehow by applying a certain degree of pressure, the buckling in $P6_3mc$ structure is removed, the resulting structure will be $P6_3/mmc$ and vice versa. However, it may require a great deal of pressure to interconvert the three structures. Further, the positions of X, Y, and Z are (1/3, 2/3, 3/4), (0, 0, 0), and (1/3, 2/3, 1/4), respectively, in $P6_3/mmc$ symmetry whereas the position along z-axis in $P6_3mc$ symmetry is free.

The chemical bonding picture in hH alloys is relatively easier to understand from the molecular orbital perspective. The XYZ can be treated as two separate entities, i.e., $[XZ]^{-}Y^{+}$ where XZ forms the covalent tetrahedral framework stabilized by electrons provided by Y. A schematic illustration of the same, taking CoTiSb as an example, is shown in Fig. 1.7. The Co and Sb form a covalent framework $[CoSb]^{-4}$ where Ti provides four of its electrons to the CoSb bonding. The resulting band gap this way can thus be tuned by varying the composition as desired. A more detailed description of crystal structure and bonding in hH alloys can be found in the review by Graf et al [59].

1.5.2 Interesting Features

Some interesting features of hH alloys which bring them at par with other TE materials are listed below:

- Tunable band gap semiconductors: The most intriguing feature of hH alloys is that their properties in most cases can be determined by merely counting the number of valence electrons in accordance with the Slater-Pauling rule [59]. According to Slater-Pauling rule, in general, the 18 valence electron count (VEC) hH alloys are semiconducting in nature [52], which is one of the prerequisites of good TE properties, as discussed in the beginning. The bonding picture, as stated above, can be seen as XZ forming the covalent tetrahedral framework stabilized by electrons provided by Y. Since the covalent bonding is considered to be the prima facie for band gap in hH alloys [17], the band gap can readily be tuned by varying the Pauling's electronegativity difference between X and Z or by varying the electropositive character of Y [59]. Thus, the band gap of hH alloys can be tuned to meet high ZT values.

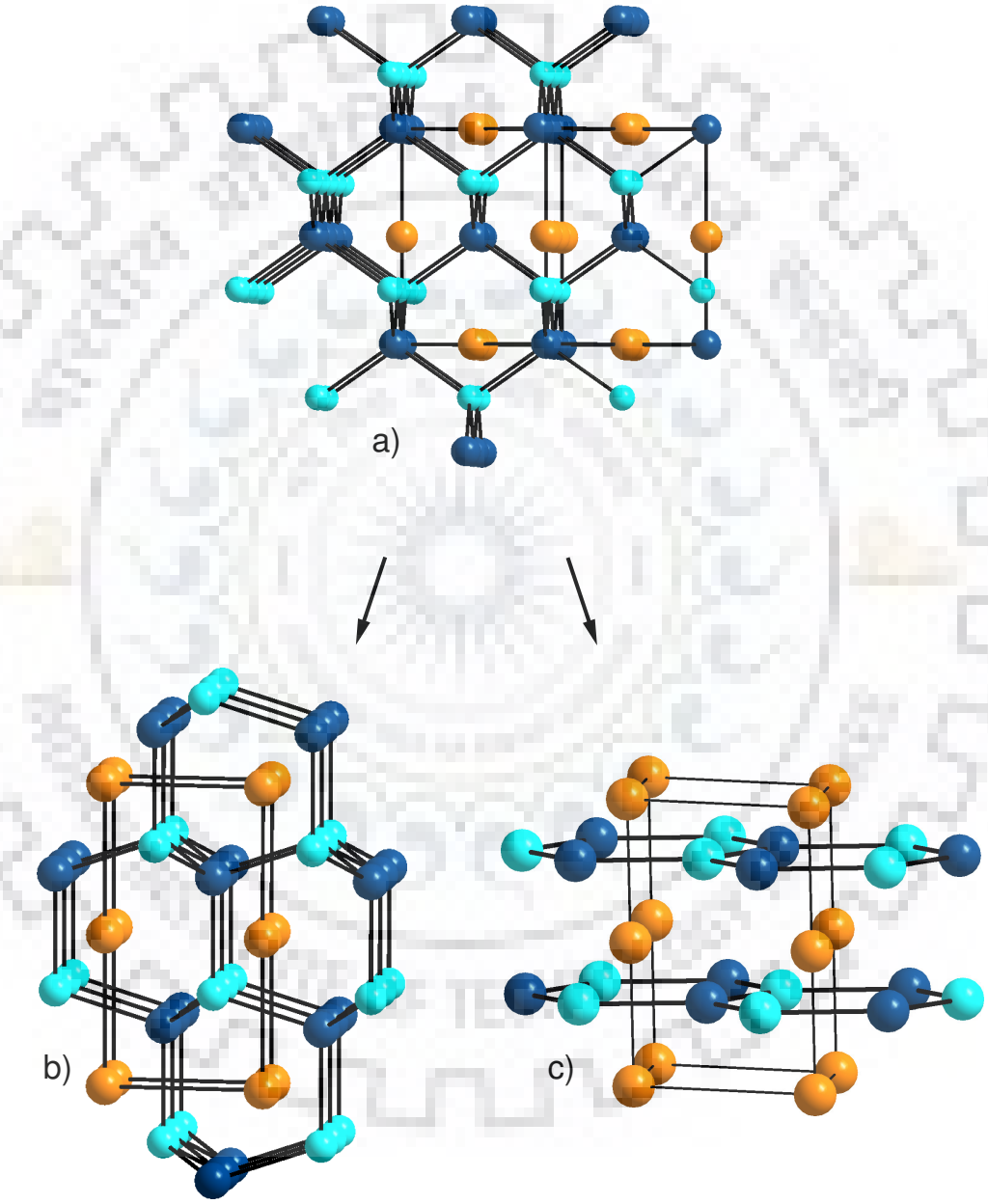

Figure 1.6: The possible crystal structures of half-Heusler alloys in a) $F\bar{4}3m$, b) $P6_3mc$, and c) $P6_3/mmc$ symmetry.

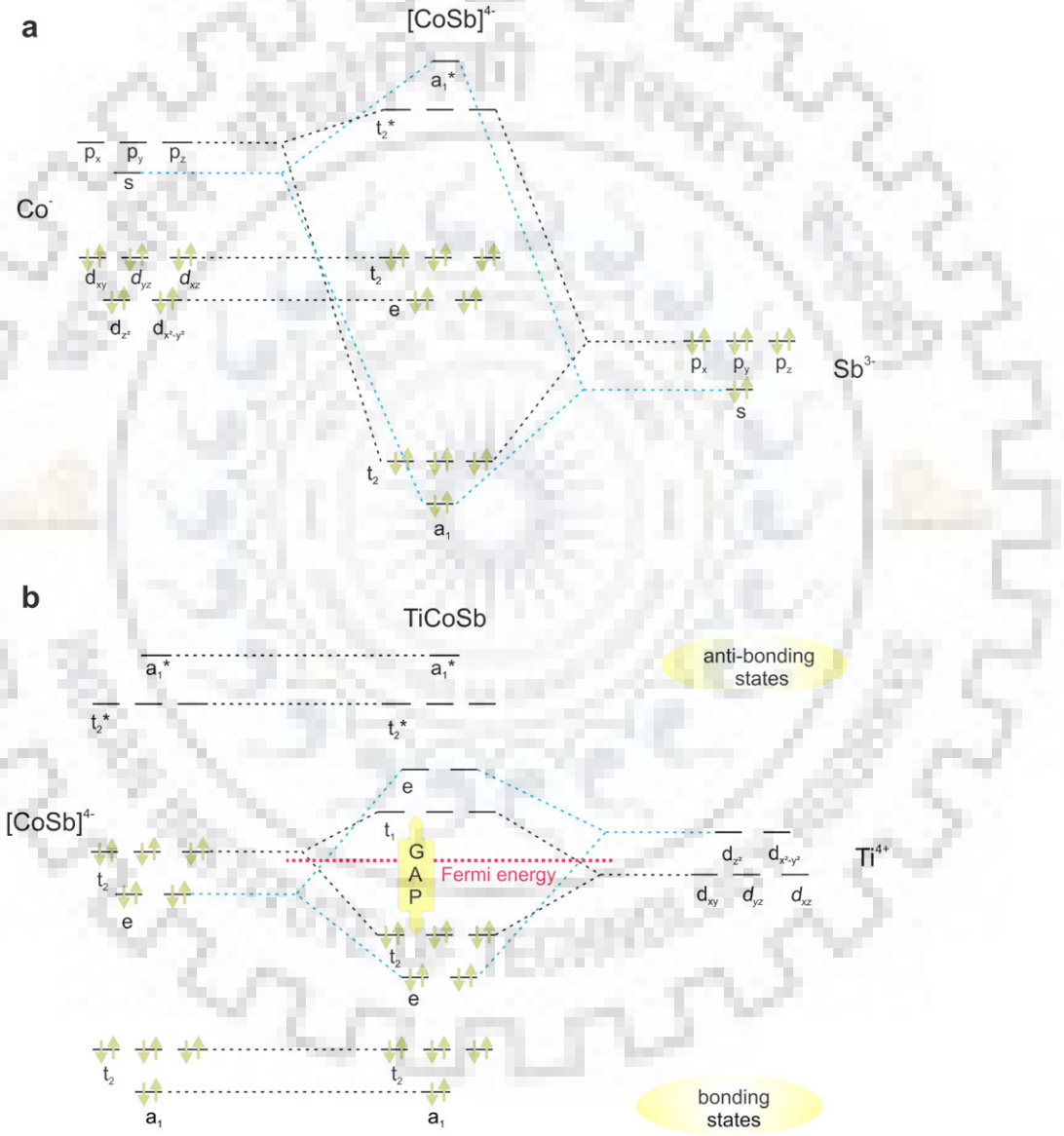

Figure 1.7: The molecular orbital picture of half-Heusler alloys, illustrated by CoTiSb [59].

- Meet Slack's predictions: Further, as per Slack's predictions, hH alloys have three elements where two form the covalent framework necessary for high mobility of the charge carriers and the third may be effective in scattering the phonons. Additionally, the unoccupied tetrahedral voids offer the advantage of doping the atoms into parent hH structures. Not only at vacant site, further, doping at three occupied sites can also be achieved to tune the TE properties. The doping improves the carrier concentration and also introduce point defects, mass fluctuation scattering or strain field scattering which are helpful in scattering the phonons at different wavelengths, thereby minimizing the thermal conductivity [148].

- Robust properties: The interest in hH alloys is also driven by their robust features such as low cost, non-toxic elements, thermal stability, and mechanical strength. These alloys can sustain high-temperature because of their high melting points. Whereas most TE materials may decompose around 600 ^{0}C, hH alloys can sustain around 1000 ^{0}C [148, 24, 75].

Despite these advantages, the hH alloys suffer a major drawback of high thermal conductivity which restricts their ZT values [148, 24, 75]. Nevertheless, as stated above, hH alloys have the privilege of vacant sites which can be exploited to reduce the thermal conductivity.

1.5.3 Progress

Many hH alloys are known to exhibit substantial TE properties competitive with conventional Bi_2Te_3 and PbTe based materials [119, 155, 81, 150]. The two most antecedent and widely investigated classes of hH alloys are MCoSb and MNiSn, where M = Ti, Zr, or Hf [24, 6]. The straightforward easy looking compositions are doped to make the structures more complicated and, accordingly, the higher ZT values are reported, e.g., $Ti_{0.5}Zr_{0.25}Hf_{0.25}Co_{0.95}Ni_{0.05}Sb$ [30]. The ZT values of doped MNiSn and MCoSb are much higher than their parent compositions. The $ZT \sim 1$ at 1000 K [155] and 0.7 at 900 K [116] have been reported for n-doped TiNisn and TiCoSb, respectively, whereas p-doped compositions have also yielded appreciable figures [31]. In addition to the conventional style of doping, nanostructuring route has been an effective strategy recently in the desire of high ZT values [147, 81]. The nanostructuring approach provides more scattering sites of varying size which can effectively scatter a wide range of phonon wavelengths without comprising on power factor [25, 11]. The nanocomposites of doped MNiSn and MCoSb have improved ZT values due to the reduction in thermal conductivity, as depicted in Fig. 1.8 [24]. The

n-type $Hf_{0.6}Zr_{0.4}NiSn_{0.995}Sb_{0.005}$ and *p*-type $Hf_{0.3}Zr_{0.7}CoSn_{0.3}Sb_{0.7}$/nano-$ZrO_2$ composites were reported to have high $ZT \sim 1.05$ and 0.8 in the temperature range 900-1000 K [115]. As mentioned in the section, each strategy has its own merits and demerits, the issue of thermal stability of nanostructures limits their high-temperature applications. With promising results and wide scope of MNiSn and MCoSb, the only drawback is the expensive Hf as the major constituent in most of the high performing hH alloys. The high prices of Hf make it difficult for large-scale application of this class [80]. Hf free compositions of MNiSn and MCoSb, however, does not yield significant ZT values. While many endeavors are being carried out to improve the ZT values by new innovative techniques, meanwhile, the surge of low cost highly efficient TE materials shifted the attention of researchers toward a new emerging class FeMSb (M = V, Nb or Ta). The constituents such as Fe, V, Nb, and Sb are earth-abundant and inexpensive, though, Ta is expensive but can be used for minimal doping the FeVSb and FeNbSb systems. The best performing hH alloys of MNiSn and MCoSb family were mainly *n*-type whereas the *p* -type hH analogues remained a challenge. This was overcome by FeMSb family as most of its compositions exhibit high ZT values on *p*-type doping. The initial investigations in this family were centered on FeVSb. The high reported PF in parent FeVSb is 48 μW cm^{-1} K^{-2}, however, the $ZT \sim 0.25$ at 550 K was achieved because of high thermal conductivity [47]. The solid solution of (V, Nb)FeSb doped with Ti recorded a peak $ZT \sim 0.8$ at 900 K [50]. Despite the various attempts, the ZT value of FeVSb has not reached the unity. Remarkably, FeNbSb based hH alloys have exhibited better TE properties and reported to exhibit $ZT > 1$ [45, 46]. The *p*-doped FeNbSb composition, i.e., $Nb_{0.6}Ta_{0.4}Ti_{0.2}FeSb$ was reported to have a high $ZT \sim 1.6$ at 1200 K [156], which is best reported till date in hH alloys. A more detailed description of the various strategies and progress over the years in hH alloys can be seen in Ref. [148], [24], and [75]. Despite the significant advances in hH alloys, still there exists a wide scope of developing new strategies and screening the unexplored plausible hH systems.

Certainly, the experimental investigations in hH alloys have led a new path, however, the role of theoretical investigations have also proven to be beneficial. Two most significant computational works in TE materials were performed in 1993 by Hicks and Dresselhaus. When historical material Bi_2Te_3 was considered to be potentially incompetent owing to a marginal increase in ZT values over the two decades, the Hicks's work showed that quantum confinement of Bi_2Te_3 may improve their ZT by a factor of 13 in comparison to bulk Bi_2Te_3 [67]. Later, Hicks showed that ZT of one-dimensional conductor strongly depends on the width of the wire. He predicted that a ZT up to 14 can be achieved if Bi_2Te_3 is made of one-dimensional wire [68]. These works largely inspired the

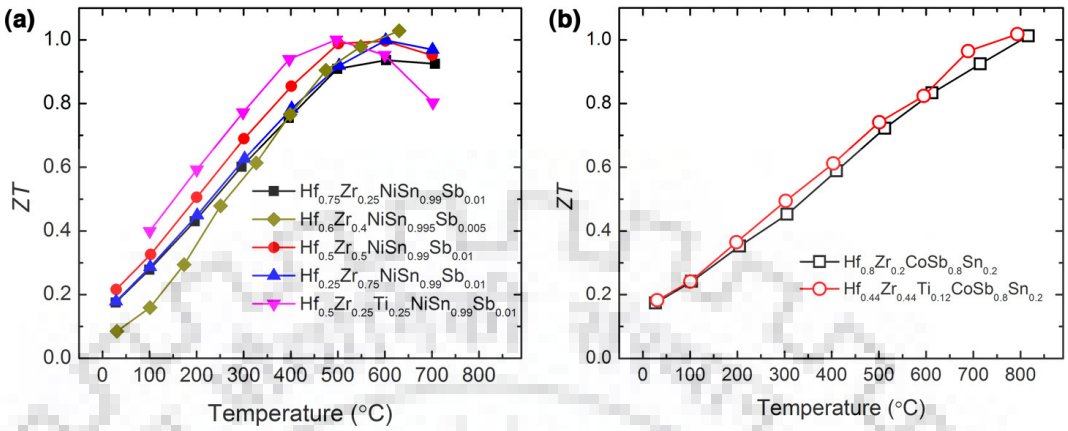

Figure 1.8: The figure of merit as a function of temperature in nanocomposites of a) *n*-type and b) *p*-type MNiSn and MCoSb, respectively [24].

role of quantum confinement in TE materials.

In the context of hH alloys, the theoretical investigations have established some important features. The prediction of 18-VEC non-magnetic semiconductors aid experimentalists to target specific materials while exploring new hH alloys. The electronic structures and band gap engineering have been helpful in modifying the Seebeck coefficient, electrical conductivity, and thus PF. Not only theoretical predictions have led to high PF and *ZT* values, indeed, the experimental realizations on theoretical bases have been successful. Also, theoretically predicted doping levels have matched the previous experimental evidence. In many cases, the theory has explained the observed experimental behavior correctly. Yang et al. screened 36 hH alloys computationally and found reasonably good Seebeck coefficient and PF values for a number of systems [152]. Further, his proposed optimal doping levels in some cases were quite good in agreement with previously reported values. Lee et al. showed that replacing Hf by Zr in HfCoSb will not alter the band structure and proposed high values of carrier concentration and PF [95]. Furthermore, out of numerous possible hH alloys, only a few systems have been reported experimentally. Therefore, a new trend has emerged to theoretically investigate the plausible hH alloys, predict their stability whether they could survive or not and then realize them experimentally. Madsen stressed that *ab initio* approach can be used not only for predicting optimal doping levels and corresponding TE coefficients but also for screening potential TE candidates. He searched for a wide number of compounds and proposed LiZnSb as the most promising *n*-type TE material [99]. Some of his assumptions were later found in agreement with experiment by Toberer [135]. Zunger et al. searched for 45 hH alloys and found that only 16 were reported. The group proposed stability of 8 new hH alloys and further synthesized one of them success-

Properties	Tool
a) Ground State Properties such as crystal structure optimization, energy of the system, electronic strcuture (DOS and band structure), and pressure-volume changes	Wien2k
b) Structural dynamical stability and lattice thermal conductivity	Quantum Espresso
c) Transport parameters such as Seebeck coefficient, electrical conductivity, and electonic thermal conductivity at optimal doping levels.	Boltztrap

Table 1.1: Various computational tools utilized for calculating different crystal structure properties.

fully [157]. Most recently, some unreported cobalt-based 18-VEC hH alloys were proposed to have good TE performances at optimal doping levels [158, 159]. All in all, where theory has been commendable in predicting the high Seebeck coefficient and PF values, the screening of new materials has also been very exemplary. The thesis is devoted to such theoretical investigations of new TE materials, therefore, the next section discusses briefly the computational techniques utilized.

1.6 Computational Details

As mentioned before, the motive of the thesis is the theoretical prediction of new potential hH alloys and the study of their electrical and thermal transport properties. The various properties and the computational tools utilized to investigate them are listed in Table 1.1. The computational tools listed in Table 1.1 are density functional theory (DFT) based, therefore, before elucidating them below is a brief description about DFT.

1.6.1 Density Functional Theory

DFT has been an effective tool for calculating the ground state properties of atoms and molecules in various disciplines of science. The heart of DFT lies in the fundamental theorems proposed by Hohenberg and Kohn (HK) in 1964 [70]. HK put forth and proved that ground state electronic energy can be determined more precisely in terms of electron

density, $\rho(\mathbf{r})$. They postulated that in accordance with the variational principle, the ground state energy is a unique functional ($E[\rho(\mathbf{r})]$) of the electron density, given by

$$E[\rho(\mathbf{r})] = \int \upsilon(\mathbf{r})\rho(\mathbf{r})\, d\mathbf{r} + F[\rho(\mathbf{r})] \tag{1.12}$$

where $F[\rho(\mathbf{r})]$ contains the electronic kinetic energy (T) and the electronic Coulomb interaction (V_{ee})

$$F[\rho(\mathbf{r})] = < \phi | T + V_{ee} | \phi > \tag{1.13}$$

and $\upsilon(\mathbf{r})$ represents the Coulomb potential due to the nuclei of the solids.
The significance of the assumption is less severely complexed nature as compared to the wave function approach. A wave function gets more complexed with an increasing number of electrons whereas the variables of electron density are independent of the system size. However, each density yields different ground state energy, unfortunately, the functional connecting them is not known. The early attempts to overcome this were based on non-interacting uniform electron gas, put forward by Thomas Fermi (TF) in 1927 [36]. Disappointingly, the assumption did not go well in many systems and the calculated energies were in error by 15-50%. Further, the TF model failed completely to predict the bondings in molecules. In 1965, in a major step toward the use of DFT methods in computational science, Kohn and Sham (KS) introduced the concept of orbitals [87]. The problem with the TF model was the inaccurately defined kinetic energy. In KS formalism, the kinetic energy functional was divided into two parts: i) one as previous which can be calculated exactly for non-interacting electrons and ii) a correction term which takes into consideration the interaction between electrons with a different potential V_{KS} (*effective Kohn-Sham potential*).

$$F[\rho] = T_s[\rho] + J[\rho] + E_{xc}[\rho] \tag{1.14}$$

where $T_s[\rho]$ is the kinetic energy of a non-interacting electron gas, $J[\rho]$ is the classical Coulomb energy (often referred as Hartree term), and $E_{xc}[\rho]$ is the *exchange-correlation energy.*

$$J[\rho] = \frac{e^2}{2} \int \int \frac{\rho(\mathbf{r})\rho(\mathbf{r}')}{|\mathbf{r} - \mathbf{r}'|}\, d\mathbf{r}\, d\mathbf{r}' \tag{1.15}$$

If equation 1.14 be compared with exact quantum mechanics energy equation, then the $E_{xc}[\rho]$ can be expressed as

$$E_{xc}[\rho] = \{T[\rho] + V_{ee}[\rho]\} - \{T_s[\rho] + J[\rho]\} \tag{1.16}$$

The difference between the exact kinetic energy and the one assuming non-interacting electrons is usually small and $E_{xc}[\rho]$ represents the correction of $J[\rho]$ originating from the electrons interactions. The effective KS-potential, V_{KS}, can be calculated from equation 1.14 by considering that the exact energy functional $E[\rho(\mathbf{r})]$ of the interacting electrons and the energy $E_s[\rho(\mathbf{r})]$ of the non-interacting electrons is minimized by the same electron density $\rho(\mathbf{r})$.

$$\left[-\frac{1}{2}\nabla^2 + V_{KS}\right]\phi_i(\mathbf{r}) = \varepsilon_\mathbf{i}\phi_\mathbf{i}(\mathbf{r}) \tag{1.17}$$

where

$$V_{KS}(\mathbf{r}) = \upsilon(\mathbf{r}) + e^2\int \frac{\rho(\mathbf{r}')}{|\mathbf{r}-\mathbf{r}'|}\,d\mathbf{r}' + \frac{\delta E_{xc}\left[\rho(\mathbf{r})\right]}{\delta\rho(\mathbf{r})} \tag{1.18}$$

The original many electrons problem can now be solved by one electron system and the charge density can be represented as:

$$\rho(\mathbf{r}) = \sum |\phi_\mathbf{i}|^\mathbf{2} \tag{1.19}$$

The DFT based on HK and KS theorems reduced the many electrons problem to one electron problem and quite an exact method since the difference between the exact kinetic energy and the one assuming non-interacting electrons is quite small. However, for more practical applications such as non-homogeneous electron densities, several other approximations were formulated. The two such successful approximations are the local-density approximation (LDA) and generalized-gradient approximation (GGA).

LDA and GGA

The local-density approximation (LDA) assumes that the density at a particular point in space can be considered as a uniform electron gas. The exchange-correlation energy for a uniform electron gas is given as

$$E_{xc}[\rho] = \int \rho(\mathbf{r})\epsilon_{xc}(\rho(\mathbf{r}))\,d\mathbf{r} \tag{1.20}$$

where ϵ_{xc} is the exchange-correlation energy per electron of a uniformly interacting electron gas of the same density, ρ. LDA is a widely used approximation in cases where electron density varies slowly. In the case of molecules, LDA is known to underestimate the exchange

energy part by ∼10% and overestimate the correlation energy. A more corrected approach is the Generalized Gradient Approximation (GGA). In GGA, exchange-correlation energy includes the first derivative of the density as a variable and can be expressed as

$$E_{xc}[\rho] = \int \rho(\mathbf{r})\epsilon_{xc}(\rho(\mathbf{r}))\,\mathbf{dr} + \int \mathbf{F_{xc}}[\rho, |\nabla\rho|]\,\mathbf{dr} \tag{1.21}$$

where F_{xc} is a correction.

A more detailed treatment can be found in Introduction to Computational Chemistry by Frank Jensen [77]. Based on the above principles, the computational tools utilized for investigating the new potential hH alloys are summarized below:

1.6.2 Wien2k

The DFT based package Wien2k is one of the most accurate computational tools for performing the electronic structure calculations. The programme is based on full-potential (linearized) augmented plane-wave (LAPW) + local orbitals (lo) method as explained below.

LAPW Method

The DFT based linearized augmented plane wave method is one of the most accurate tools for computing the electronic properties of crystal structures. The fundamental idea is to solve the KS equations of a crystal system by incorporating a proper basis set which can be obtained by partitioning the unit cell into two parts I) non-overlapping atomic spheres and II) an interstitial domain, as shown in Fig. 1.9. A different basis set is used for non-overlapping atomic spheres and interstitial space, as discussed below:

I) Non-overlapping atomic spheres: Here, a product of a linear combination of radial functions and spherical harmonics is used.

$$\phi_{k_n} = \sum_{lm}[A_{lm,k_n}u_l(r, E_l) + B_{lm,k_n}u_l(r, E_l)]Y_{lm}(r') \tag{1.22}$$

where $u_l(r, E_l)$ is the radial solution for energy E_l and the spherical part of the potential inside the sphere; and $u_l(r, E_l)$ is the energy derivative of energy E_l. The coefficients A_{lm} and B_{lm} are the function of k_n.

II) Interstitial space: For this region, a plane wave expansion is used

$$\phi_{k_n} = \frac{1}{\sqrt{\omega}}e^{ik_n.r} \tag{1.23}$$

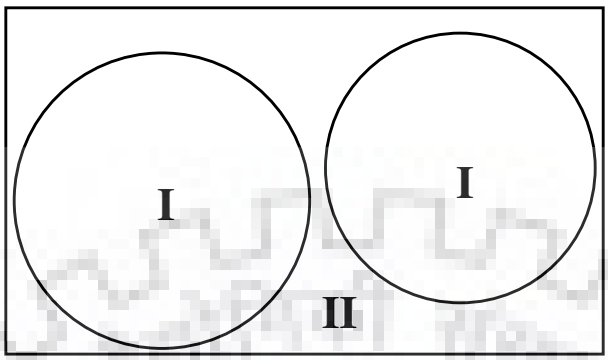

Figure 1.9: Basis set construction used in Wien2k I) Non-overlapping atomic spheres (atomic sites) and II) an interstitial space.

where k_n comprises the reciprocal lattice vector and wave vector in the first Brillouin zone. Using these combined basis sets, the KS equations are solved as per the linear variation principle.

$$\psi_k = \sum_n c_n \phi k_n \tag{1.24}$$

The convergence test of the basis set is governed by a product of the smallest atomic sphere radius, R_{mt} (6-9), and the largest K vector i.e K_{max}, according to the equation 1.24. To ensure a consistent consideration of semi-core and valence states, some local orbitals can be added into the picture. Such local orbitals form a linear combination of two radial functions at two different energies and one energy derivative, according to the equation

$$\phi_{lm}^{LO} = \sum_{lm} [A_{lm,k_n} u_l(r, E_{1,l}) + B_{lm,k_n} u_l(r, E_{1,l}) + C_{lm,k_n} u_l(r, E_{2,l})] Y_{lm}(r') \tag{1.25}$$

The coefficients A_{lm}, B_{lm}, and C_{lm} can be calculated by applying boundary conditions at sphere boundary and normalization of ϕ_{lm}^{LO}. In general, the LAPW method does not use any shape approximations and hence also known as 'full-potential method'[28, 13].

1.6.3 Quantum Espresso

Quantum Espresso (QE), based on DFT, plane waves, and pseudopotentials, is an open-source code for electronic structure calculations and materials modeling. The code takes into consideration the plane wave basis-sets with periodic boundary conditions and pseudopotentials for electronic structure calculations. QE can be used for computing the properties of crystalline and long-range amorphous materials. The otherwise systems can be

solved by the supercell approach using the density-countercharge method. In other words, QE can be used for studying a wide range of metals and insulators. The core structure of atom can be defined by various pseudopotentials such as norm-conserving (NP), ultrasoft (US), and projector-augmented wave sets (PAW). A wide range of exchange-correlation functionals are also implemented within the LDA and GGA approximations, supplemented by some advanced functionals such as Hubbard U corrections, meta-GGA, and hybrid functionals. The programme consists of some core packages such as $Pwscf$, CP, and $PostProc$ whereas the additional packages include $atomic$, $PHononpackage$, NEB, and $D3Q$ to name a few [57, 58, 56]. Within QE, the density functional perturbation theory (DFPT) is implemented to calculate the phonon dispersions, electron-phonon, and phonon-phonon interactions by solving the second and third derivatives of the energy at arbitrary wavelengths.

1.6.4 Boltztrap

Boltztrap is a program for calculating the semi-classic transport coefficients. This program is interfaced with Wien2k but can also be used with other DFT based codes. The code is based on the Fourier expansion of the band energies, meanwhile, retaining the original symmetry of the system by employing star functions. The Fourier expansion makes it relatively an easier procedure to calculate properties relying on band structure and has been successfully tested for superconductors, intermetallics, and thermoelectric materials. The transport properties of materials can be analyzed within the Boltzmann theory. The electric current, j, of a system in the presence of electric field, E_j, magnetic field, B_k, and a thermal gradient, Δ_{ij}, can be expanded as the conductivity tensors

$$j_i = \sigma_{ij}E_j + \sigma_{ij}E_jB_k + v_{ij}\Delta_{ij}T + ... \tag{1.26}$$

In terms of the group velocity, $v_\alpha(i,k)$, the conductivity tensors can be rewritten as

$$\sigma_{\alpha\beta}(i,k) = e^2\tau_{i,k}v_\alpha(i,k)v_\beta(i,k) \tag{1.27}$$

where τ is the relaxation time depending on the band index i and k vector direction, and v is the group velocity.

In terms of the above equation, the density of states energy projected conductivity tensor can be written as

$$\sigma_{\alpha\beta}(\varepsilon) = \frac{1}{N}\sum_{i,k}\sigma_{\alpha\beta}(i,k)\frac{\delta(\varepsilon-\varepsilon_{i,k})}{d\varepsilon} \tag{1.28}$$

where N is the number of k-points sampled.
The transport properties according to the equation 1.26 can be evaluated from the conductivity distributions

$$\sigma_{\alpha\beta}(T;\mu) = \frac{1}{\Omega}\int \sigma_{\alpha\beta}(\varepsilon)\left[-\frac{\partial f_\mu(T;\varepsilon)}{\partial\varepsilon}\right]d\varepsilon, \tag{1.29}$$

$$\upsilon_{\alpha\beta}(T;\mu) = \frac{1}{eT\Omega}\int \sigma_{\alpha\beta}(\varepsilon)(\varepsilon-\mu)\left[-\frac{\partial f_\mu(T;\varepsilon)}{\partial\varepsilon}\right]d\varepsilon, \tag{1.30}$$

$$\kappa^0_{\alpha\beta}(T;\mu) = \frac{1}{e^2T\Omega}\int \sigma_{\alpha\beta}(\varepsilon)(\varepsilon-\mu)^2\left[-\frac{\partial f_\mu(T;\varepsilon)}{\partial\varepsilon}\right]d\varepsilon, \tag{1.31}$$

where κ^0 is the electronic thermal conductivity.
The Seebeck and Hall coefficient can be calculated as

$$S_{ij} = E_i(\Delta_j T)^{-1} = (\sigma^{-1})_{\alpha i}\upsilon_{\alpha j}, \tag{1.32}$$

$$R_{ijk} = \frac{E_j^{ind}}{j_i^{appl}B_k^{appl}} = (\sigma^{-1})_{\alpha j}\sigma_{\alpha\beta k}(\sigma^{-1})_{i\beta}, \tag{1.33}$$

The Seebeck and Hall coefficient are both independent of relaxation time under the assumption that the relaxation time τ is direction independent [100].

1.7 Methodology

As discussed before, in addition to the improvement in existing materials, there is a dire need to search for new TE materials. Therefore, in the quest for new thermoelectric materials, the first step of our working scheme is to identify new plausible potential Heusler alloys. On careful analysis of the periodic table, one can notice that X, Y, and Z, in Heusler alloys mostly originate from the elements highlighted in red, blue, and green, respectively, Fig.1.10. Once the materials of interest are chosen, the next key step is to check their ground properties which are studied by Wien2k. Within the ground state calculations, some basic properties that define a crystal structure are studied. For instance, the symmetry of the chosen system, its atomic positions, volume, lattice parameters, magnetic nature, whether the system is metallic or semiconductor etc., are established. This is performed by minimizing the total energy as a function of volume, fitted with Birch-Murnaghan equation [9].

As stated in previous sections, semiconductors are the best choices for TE materials, so once it is established that the chosen system is semiconducting, the next key step

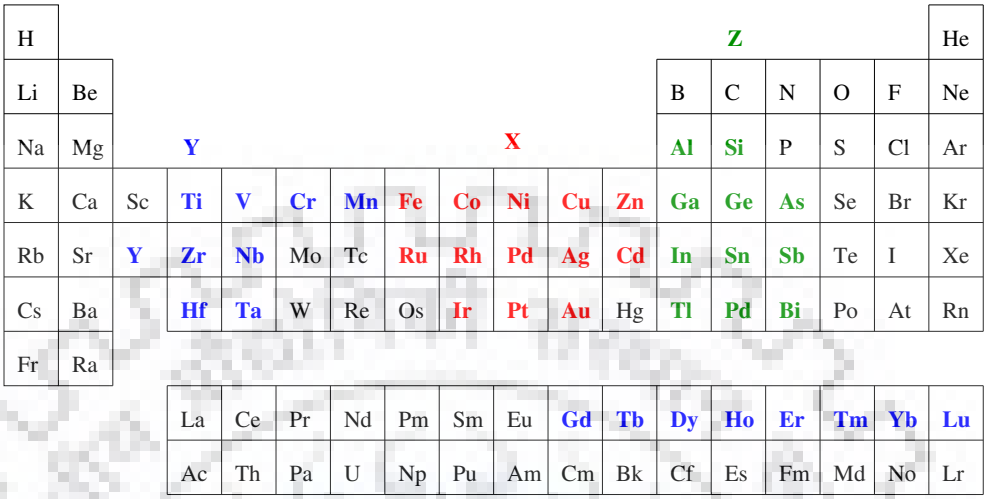

Figure 1.10: Periodic table from the viewpoint of half-Heusler alloys. The elements highlighted in red, blue, and green represent X, Y, and Z, respectively.

is to check its stability. Whether the chosen system is able to survive or not. For this, the dynamic stability of the selected systems is tested by phonon calculations by density functional perturbation theory (DFPT) implemented within the Quantum Espresso. The procedure comprises of two steps, i.e., first, the crystal structure is optimized by QE, followed by calculation of phonon dispersions curves which serves as an indication of stability. The real phonon frequencies are an indication of dynamic stability whereas the presence of imaginary frequencies implies the instability in the system [39, 137]. The systems having imaginary frequencies are discarded and proceed with the dynamically stable ones. Once the dynamic stability of the system under consideration is confirmed, next, the electronic structure is studied with the help of Wien2k.

The electronic band structure and density of states give an insight about the actual transport properties. The electronic features explain which states are responsible at the valence band maximum and conduction band minimum and how the nature of bands will affect the transport properties, discussed in detail in the following chapters. As well, it gives a beforehand intuition about the doping in the system. As an example, XYZ, if the states of X and Y atoms predominantly occupies the VBM and CBM, then it might be possible that any doping of Z by some other element may not affect the parent band structure much. Thus, the electronic transport properties will not be affected whereas the doping may be helpful in reducing the thermal conductivity part. Such theoretical predictions can be helpful in narrowing down the range of dopants. Following the electronic features, the transport properties are evaluated by Boltztrap code which relies on the structural input

from Wien2k.

The transport properties are calculated within the two widely accepted approximations: I) rigid band approximation (RBA) and II) constant relaxation time approximation (CRTA). The two approximations have been successfully utilized by many groups for theoretical prediction of transport properties [99, 21, 95, 79]. The RBA is applicable at low doping levels and considers that on doping a system, the Fermi level shifts up and down without significantly affecting the fundamental band structure. Thus, a single band structure calculation is acceptable for different doping concentrations. As Boltztap code doesn't provide the relaxation time value, the CRTA is helpful in evaluating the parameters which are relaxation time-dependent, e.g., electrical conductivity. Thus, by selecting a constant number for relaxation time, electrical conductivity can be estimated. The constant value of relaxation time can be selected on the basis of previous evidences or by exploiting the experimental electrical conductivity as discussed in chapter-2. The parameters which interest the TE efficiency viz. Seebeck coefficient, electrical conductivity, and electronic thermal conductivity can be obtained as a function of temperature or doping (per unit cell) by the Boltztrap code.

Now, the only part left in the evaluation of ZT is lattice thermal conductivity part, κ_l, which is calculated with the help of D3Q package implemented in Quantum Espresso. In crystals having the band gap, the heat conduction by lattice vibrations is dominant which can be evaluated with the help of harmonic phonon energies and anharmonic phonon-phonon scattering coefficients. The former can be obtained by the second-order derivative of the total energy of the system, with respect to atomic displacements. The second-order derivative of the energy can be obtained by the DFPT which enables to solve the phonon dynamical matrix for an arbitrary q wave vector in the Brillouin zone. The latter part anharmonic scattering coefficients can be obtained by the third-order derivative of the energy of the system with respect to three-phonon perturbations, given by the wave vectors q, $\mathrm{q}^{'}$, and $\mathrm{q}^{''}$. These coefficients can be calculated with the help of "2n + 1" theorem within DFPT. Paulatto et al., based on "2n + 1" theorem, implemented a generic method within the DFPT to compute the three phonons anharmonic coefficients for the arbitrary wave vectors q, $\mathrm{q}^{'}$, and $\mathrm{q}^{''}$. The calculated anharmonic coefficients can serve two purposes. First, the anharmonic broadening of a phonon with an arbitrary wave vector q can be calculated. Also, these coefficients can be used in computing the intrinsic thermal conductivity within the single-mode relaxation time approximation (SMA) [110, 51].

The above discussed brief methodology of the working scheme is illustrated step by step in Fig.1.11. As per the working scheme, the computational parameters used at each

step are summarized next. The FLAPW calculations were performed using the implementation of the generalized gradient approximation (GGA), Perdew-Burke-Ernzerhof (PBE correlation) [112] for Nowotny-Juza phases whereas the modified Perdew-Burke-Ernzerhof (PBEsol correlation) [113] was used for rest all systems. The calculations were performed under the scalar relativistic approximation whereas full relativistic approach was used wherever required, e.g., LiZnbi, CoTaSn, CoMoIn, and CoWIn. However, no significant impact of the spin-orbit coupling was noticed on the band structures. The muffin-tin radii (RMT's) were taken in the range of 2.3-2.6 Bohr radii for hH alloys and 1.77-2.5 Bohr radii for Nowotny-Juza phases. The convergence test R_{mt}xK_{max} was set at 7 as the plane wave cut off. The self-consistent calculations were performed using 125000 k-points throughout the Brillouin zone. The energy and charge convergence criterion used was 10^{-6} Ry and 10^{-5} e, respectively. The electrical transport properties were calculated within the Boltzmann theory [22] and relaxation time approximation as implemented in the Boltztrap code [100]. The electrical conductivity and power factor were calculated with respect to time relaxation, τ; whereas the Seebeck coefficient was taken to be independent of relaxation time, τ.

In the plane-wave pseudopotential approach, scalar-relativistic, norm-conserving pseudopotentials were used for a plane-wave cutoff energy of 100 Ry. The exchange-correlation energy functional was evaluated within the generalized gradient approximation (GGA), using the Perdew-Burke-Ernzerhof parametrization, and the Brillouin zone was sampled with a 20x20x20 mesh of Monkhorst-Pack k-points. The calculations were carried out on a 2x2x2 q-mesh in the phonon Brillouin zone. The lattice thermal conductivity was obtained by solving the linearized Boltzmann transport equation (BTE) within the single-mode relaxation time approximation (SMA) [169] using the D3Q package implemented in the Quantum Espresso. The Troullier-Martins norm-conserving pseudopotentials were used from the Quantum Espresso webpage [56]. The energy cutoff for the plane-wave basis set was set at 100 eV and Brillouin zone integration was performed on a Monkhorst-Pack 20x20x20.

1.8 Structure of Thesis

The thesis is organized into five chapters. The introductory chapter outlines the central challenges the world is currently facing and the plausible solutions. One such solution, as discussed, is the clean alternative source of energy thermoelectricity. Further, the various aspects of thermoelectricity such as thermoelectric efficiency, ways to improve it, materials of interests, are discussed. One promising class of thermoelectric materials, half-

Heusler alloys, is discussed in detail. The crystal structure, interesting features, and the recent progress of these alloys is explored. Along with experimental exploration, the role of computational studies has been emphasized in designing new half-Heusler alloys. Since the thesis is dedicated to exploring computationally the potential half-Heusler alloys, a brief introduction about density functional theory and various computational tools utilized are discussed. Based on such computational techniques, the succeeding chapters (chapters 2-5) are dedicated to the investigation of new plausible Heusler alloys for thermoelectric applications.

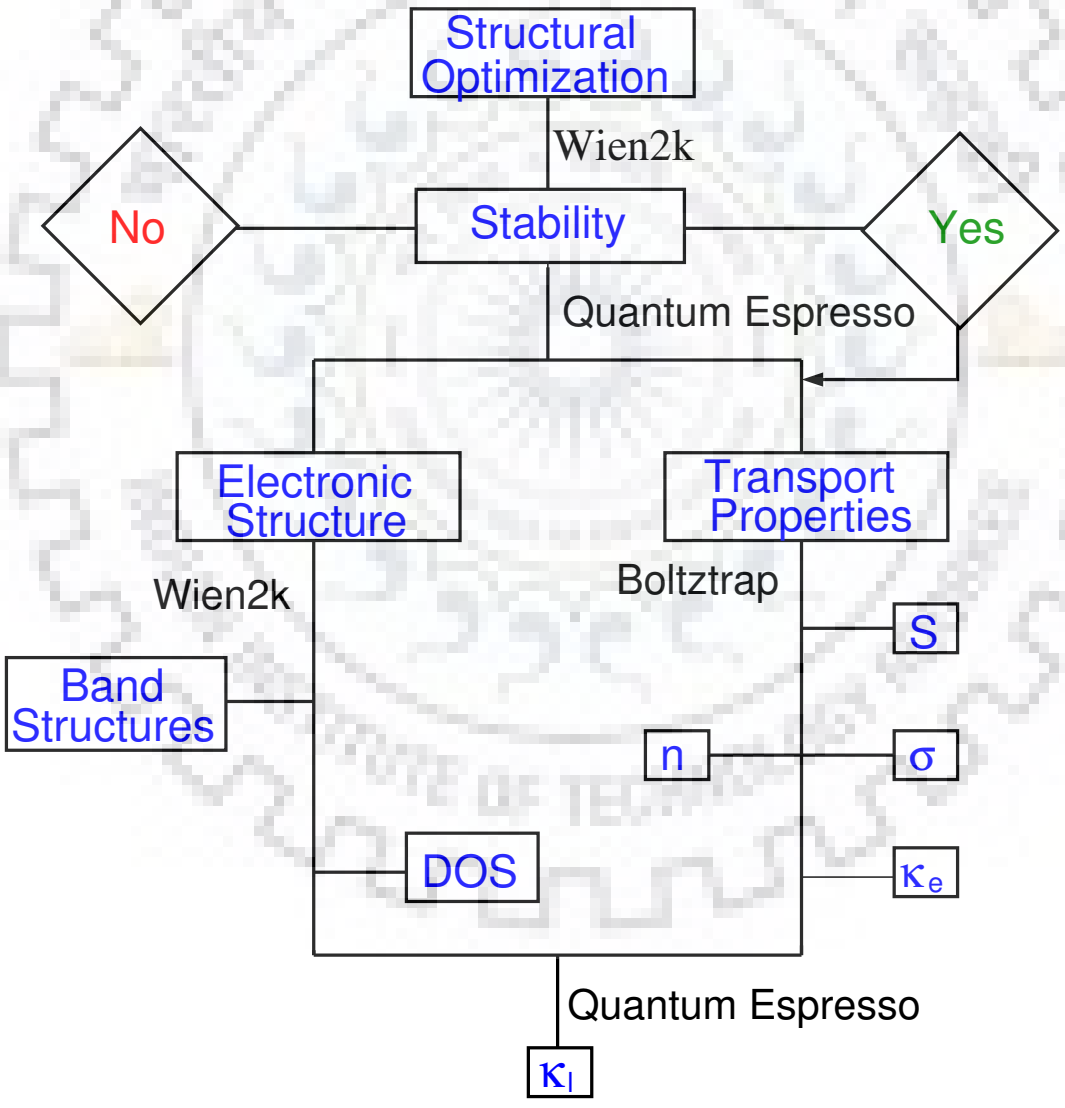

Figure 1.11: A brief methodology of the working scheme.

Chapter-2 discusses the *ab initio* design of new cobalt-based half-Heusler materials for thermoelectric applications. The chapter systematically investigates the ther-

modynamic stability, dynamical stability, and explore the electronic transport properties of new plausible cobalt-based 18 valence electron count half-Heusler alloys in $F\bar{4}3m$ and $P6_3/mmc$ symmetry, with the help of first-principles calculations. Chapter-3 discusses the hole-doped cobalt-based Heusler phases as prospective high-performance high-temperature thermoelectrics. The chapter establishes the thermal conductivity, and thereby ZT, of p-type doped CoVSn, CoNbSn, CoTaSn, CoMoIn, and CoWIn, combining a first-principles approach with semiclassical Boltzmann transport theory. Chapter-4 deals with the *ab initio* electronic structure calculations, semiclassical Boltzmann transport theory, and a rigid band approximation to systematically investigate the thermodynamic stability, dynamical stability, and thermal and electrical transport properties of FeTaSb and FeMnTiSb in cubic $F\bar{4}3m$ symmetry. Finally, the chapter-5 presents the polytypism in LiZnX (X = N, P, As, Sb, and Bi) family, the role of internal and hydrostatic pressure in controlling such behavior, and the effect of polytypism on thermoelectric properties.

Chapter 2

Electrical Transport Properties of Cobalt Based Half-Heusler Alloys

This chapter discusses the new cobalt-based half-Heusler (hH) alloys as potential thermoelectric (TE) prospects and presents results of the *ab initio* study of nine cobalt-based hH alloys. The results include structural optimization of CoYZ systems (Y = Ti, Zr, Hf, V, Nb, Ta, Cr, Mo, W & Z = Sb, Sn, In) in $F\bar{4}3m$ and $P6_3/mmc$ space group, crystal structure stability, (phonon calculations), electronic structure (Band and DOS) calculations, and finally transport properties and their behavior with doping concentration at different temperatures. Further, the importance of doping in hH alloys and emphasis on the interplay of theory and experiment for designing new potential TE materials is summarized at the end.

2.1 Introduction

One remarkable property which makes hH alloys particularly interesting, as mentioned before, is the narrow band gap semiconducting behavior of 18 valence electron count (VEC) ternary hH alloys [154, 31, 19, 18]. Generally, the 18-VEC hH alloys are found to be in agreement with the Slater-Pauling Rule, i.e., $M = N_v - 18$, where N_v = valence electrons and M is the magnetic moment [52]. Most evidently, cobalt-based 18-VEC hH alloys follow the Slater Pauling Rule, i.e., non-magnetic semiconductors [42]. For instance, CoTiSb has $N_v = 18$, $M = 0$, and is a non-magnetic semiconductor [53, 88, 43, 52]. In the past two decades, a large number of hH alloys have been reported to exhibit substantial TE properties comparable to conventional Bi_2Te_3 and PbTe based materials [41, 162, 155, 81, 150, 119, 96, 40]. Poon et al. reported that the n-type

$Hf_{0.6}Zr_{0.4}NiSn_{0.995}Sb_{0.005}$ hH alloy and p-type $Hf_{0.3}Zr_{0.7}CoSn_{0.3}Sb_{0.7}$/nano-$ZrO_2$ composites achieved $ZT = 1.05$ and 0.8 near 900-1000 K, respectively [115]. In another work, Joshi et al. reported a high $ZT \sim 1$ at 700 °C for a nanostructured p-type $Nb_{0.6}Ti_{0.4}FeSb_{0.95}Sn_{0.05}$ composition [80].

More recently, Zunger and coworkers, with the aid of first-principles calculations, systematically investigated the cobalt, rhodium, and iridium-based 18-VEC hH alloys and revealed some new thermodynamically stable systems [157]. In addition, for the first time, they experimentally realized the CoTaSn system. This is the motivation to search for the missing 18-VEC hH alloys. Till now, a large number of hH alloys have been documented in Inorganic Crystal Structure Database (ICSD) and still there exists a wide horizon to search for new potential hH candidates [84]. In the quest for the same, the cobalt-based 18-VEC hH alloys were screened. It surfaced that CoTiSb, CoZrSb, CoHfSb, CoVSn, CoNbSn, and CoTaSn are well explored in theory and experiment. However, the credibility of CoVSn and CoTaSn for a potential TE material is yet to be tested. Further, CoCrIn, CoMoIn, and CoWIn are found to be missing from the timeline of TE materials.

Therefore, a study of thermodynamic stability, dynamical stability, and the electronic transport properties of new plausible cobalt-based hH alloys in both cubic ($F\bar{4}3m$) and hexagonal ($P6_3/mmc$) space groups is demonstrated with the help of first-principles calculations. The idea behind the hexagonal crystal structure stems from the earlier work of Noda and Casper. Casper et al. searched for the hexagonal analogues of half-metallic hH XYZ alloys [17]. In another work, Noda et al. studied a phase transition from cubic-CoVSb to hexagonal-CoVSb on applying a high pressure of 5 GPa [106]. The cubic-hexagonal phase transition is somewhat analogous to a diamond-graphite phase transition. Here, the diamondlike tetrahedral environment of XZ collapses into graphite like honeycomb sublattice. The crystal structure is discussed in detail in Chapter-1. The pressure induced cubic-hexagonal phase transition may have pronounced effect on the nature of chemical bonding, structural, and electronic properties of materials. For instance, on the application of pressure, insulators may become metallic or vice versa [103]. The complete redistribution of structural and electronic properties may be useful for improving the efficiency of existing TE materials.

2.1.1 Structural Optimization

For convenience, CoTiSb, CoZrSb, CoHfSb are addressed as Ti-group; CoVSn, CoNbSn, CoTaSn as V-group; and CoCrIn, CoMoIn, CoWIn as Cr-group. In order to establish the ground state properties, all 9 systems in both cubic and hexagonal framework

	$F\bar{4}3m$			$P6_3/mmc$	
Compound	a (Å)	E_g (eV)	B_0 (GPa)	a (Å)	c (Å)
CoTiSb	5.82 (5.8818)	1.11 (0.19)	156.4	4.344	5.509
CoZrSb	6.03 (6.0676)	1.08 (0.14)	148.6	4.394	6.072
CoHfSb	5.99 (6.0383)	1.14 (0.07)	154.8	4.394	5.958
CoVSn	5.73 (5.9800)	0.66 (0.75)	166.5	4.330	5.205
CoNbSn	5.90 (5.9559)	1.02 (1.00)	170.6	4.427	5.518
CoTaSn	5.89 (5.9400)	1.06 (1.30)	180.4	4.415	5.536
CoCrIn	5.68 (-)	0.00 (-)	161.5	4.339	4.946
CoMoIn	5.80 (-)	0.04 (-)	178.4	4.444	5.150
CoWIn	5.80 (-)	0.51 (-)	193.7	4.429	5.214

Table 2.1: Optimized cell parameters, band gap, and bulk modulus for CoYZ half-Heusler alloys in cubic symmetry and optimized cell parameters for CoYZ half-Heusler alloys in hexagonal symmetry. The corresponding reported values are given in parentheses [124, 98, 14, 157, 66, 62].

were optimized. The total energy is minimized as a function of volume, fitted with Birch-Murnaghan equation [9], for cubic systems in $F\bar{4}3m$ symmetry. And for hexagonal systems, the energy is minimized as a function of volume and c/a parameter in $P6_3/mmc$ symmetry. The calculated lattice parameters for both cubic and hexagonal systems are listed in Table 2.1. The calculated lattice parameters for cubic Ti-group and V-group are in good agreement with experimental values in parentheses. The reliability of the calculations lies in the fact that the discrepancy between calculated and experimental lattice parameters lies in the range of 0.69-1.01%, except for CoVSn system (4.3%). However, the calculated lattice parameter for CoVSn by Hichour et al. [66] and Ameri et al. [2] also showed the same discrepancy. The trend to be followed for Ti-group and V-group, from Table 2.1, is the increase in lattice parameter on going from *3d* to *4d* element (Ti to Zr and V to Nb) and subsequent decrease on going from *4d* to *5d* element (Zr to Hf and Nb to Ta). The corresponding increase in lattice parameter in going from first to the second member of the same family is quite apparent whereas the increase in lattice parameter, in going from CoZrSb to CoHfsb and CoVSn to CoNbSn, can be attributed to lanthanide contraction [73, 29]. However, a regular increase in lattice parameter was observed for the Cr-group.

The calculated band gaps of all cubic systems, except CoCrIn, showed semiconducting behavior and are listed in Table 2.1. The band gap values for cubic systems lies

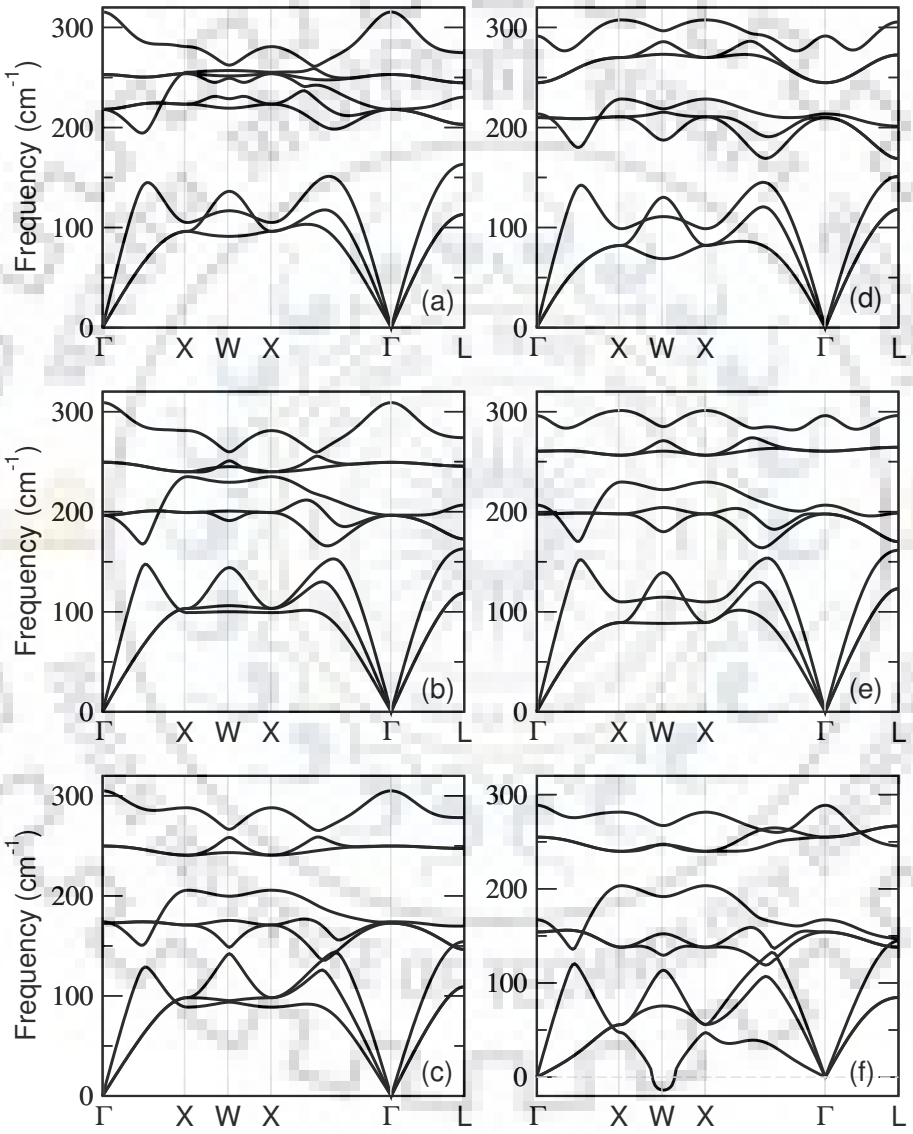

Figure 2.1: (a-f) Phonon dispersion curves for CoVSn, CoNbSn, CoTaSn, CoCrIn, CoMoIn, and CoWIn, respectively, in $F\bar{4}3m$ symmetry.

in the range of 0.03-1.13 eV which is good for TE materials. The calculated band gap values for Ti-group and V-group are in good agreement with previously calculated values. However, the experimental band gap values for CoTiSb (0.19 eV) and CoHfSb (0.14 eV) are very small in comparison to calculated values. The possible explanation, as suggested by Sekimoto et al., could be the deviation from stoichiometric composition and anti-site disordering [124]. There was no previous evidence of calculated band gap for CoZrSb and experimental band gap for V-group. In Cr-group, CoMoIn and CoWIn showed narrow band gap whereas CoCrIn was metallic in nature. All systems in hexagonal symmetry also showed metallic behavior, i.e., insulator to metallic transition on applying hydrostatic pressure to the cubic system. Since the metallic systems are not good choices for TE materials, the cubic-CoCrIn and all hexagonal systems were discarded for further evaluation. For further study, CoVSn, CoNbSn, CoTaSn, CoMoIn, and CoWIn systems were selected.

The bulk modulus, listed in Table 2.1, gives the idea of the stiffness of the material. The calculated bulk modulus of all the systems is comparable to that of steel and is an indication of a strong material. From Table 2.1, it is easy to notice the strength of CoTaSn, CoMoIn, and CoWIn. The stiffness of these systems is a good indication since the hH alloys are desired to work under robust conditions.

2.1.2 Phonon Calculations

Phonons can be considered as normal modes or quantum of vibrations in crystal and serve the purpose of crystal structure stability. Phonon stability lies in the fact that the frequency for each phonon should be a real quantity and not imaginary. As can be seen from Fig. 2.1, there are no imaginary frequencies throughout the Brillouin zone for V-group and Cr-group, except CoWIn, where imaginary frequencies were observed along W-direction. However, the imaginary frequencies up to 10 cm^{-1} are not of much concern and can be removed by employing anharmonic approximations [64]. Thus, the dynamic stability of V-group and Cr-group alloys is ensured.

2.1.3 Electronic Structure

The band structure and DOS of V-group and Cr-group are shown in Fig. 2.2 and Fig. 2.3. Taking transport properties into account, some gross features from band structure and DOS plot are discussed below.

i) The states (not shown for clarity) participating at valence band maximum (VBM) and conduction band minimum (CBM) for all the systems, mostly originated from the *d*-*d* mixing between X and Y atoms, along with some low lying *p*-states of Z atom. The

d-d mixing may vary depending on the combination of X-Y. ii) The interplay of degeneracy and dispersion of bands at VBM plays an important role in transport properties. The VBM of V-group, except for CoNbSn, is located at L point and is twofold degenerate. The VBM of CoNbSn is at L and W points. Here, both L and W points can contribute towards charge carrier transition, thereby enhancing the TE properties. The flat bands in L-Γ region are reflective of *d-d* mixing between X-Y atoms. Twofold degeneracy and flat band correspond to the heavier mass of charge carriers which enhances Seebeck coefficient. However, heavy charge carriers at VBM lead to a reduction in electrical conductivity. The contribution towards electrical conductivity may come from low lying bands below VBM, having low effective mass of charge carriers. The VBM of Cr-group is located at X point and is also twofold degenerate. The flatter bands in this group appeared in X-W region and are less dispersed as compared to V-group, indicative of low thermopower, S [149, 95, 152, 109]. iii) The nature of band gap of V-group is indirect (L-X) whereas that of Cr-group is direct at X point. Overall, the bulk modulus and dynamic thermal stability collectively support the TE potential of CoMoIn and CoWIn. Thus, it would be interesting to see how their transport properties will respond.

2.1.4 Transport Properties

In this section, using rigid band approximation (RBA), semi-classical Boltzmann theory, and constant relaxation time (τ), the calculated transport properties and optimal doping concentrations for attaining maximum power factor (PF) are presented. This would encourage the experimentalists to choose a narrow range for varying doping levels. Figures 2.4 and 2.6 show the calculated transport properties for CoTiSb (in comparison with experiment) and V-group and Cr-group, respectively. Before discussing individual systems, first, the common features of transport properties of CoTiSb, V-group, and Cr-group are discussed. Seebeck coefficient of all the systems was maximum when the Fermi level was close to the middle of the band gap and dropped almost exponentially with doping. However, exactly opposite trend was observed for electrical conductivity. Electrical conductivity was very low when Fermi level was close to the band gap but increased rapidly on doping. When Fermi level shifts towards the VBM or CBM, the density of states increases at the Fermi level, thereby increasing the electrical conductivity and lowering the Seebeck coefficient [95, 152, 109]. As per Mott equation [65, 32], for heavily doped systems, Seebeck coefficient decreases with increasing carrier concentration. Therefore, a TE material should be tuned in such a way that it maintains a high Seebeck coefficient without any significant reduction in electrical conductivity. The combined effect of the dependence of Seebeck co-

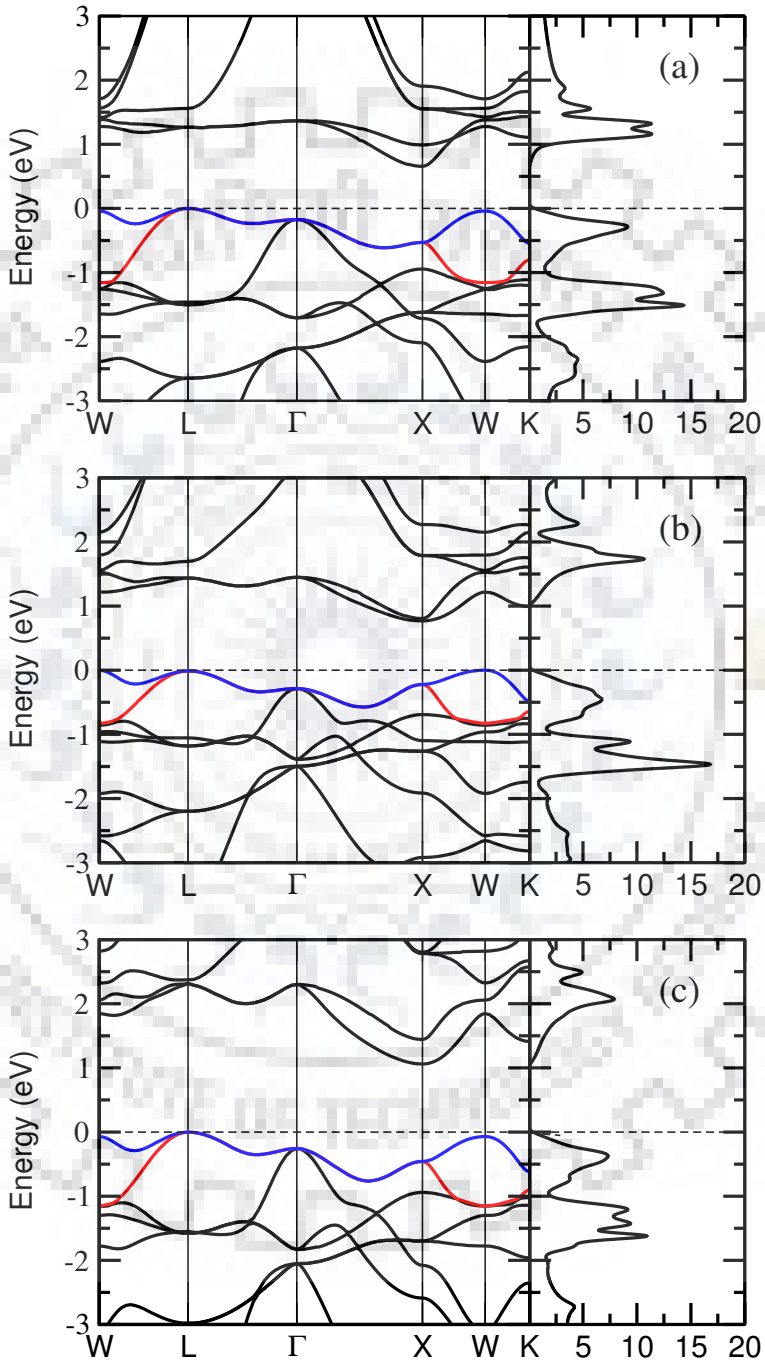

Figure 2.2: (a-c) Calculated electronic structures for CoVSn, CoNbSn, and CoTaSn, respectively, in $F\bar{4}3m$ symmetry. The top of the valence band is taken as zero on the energy axis.

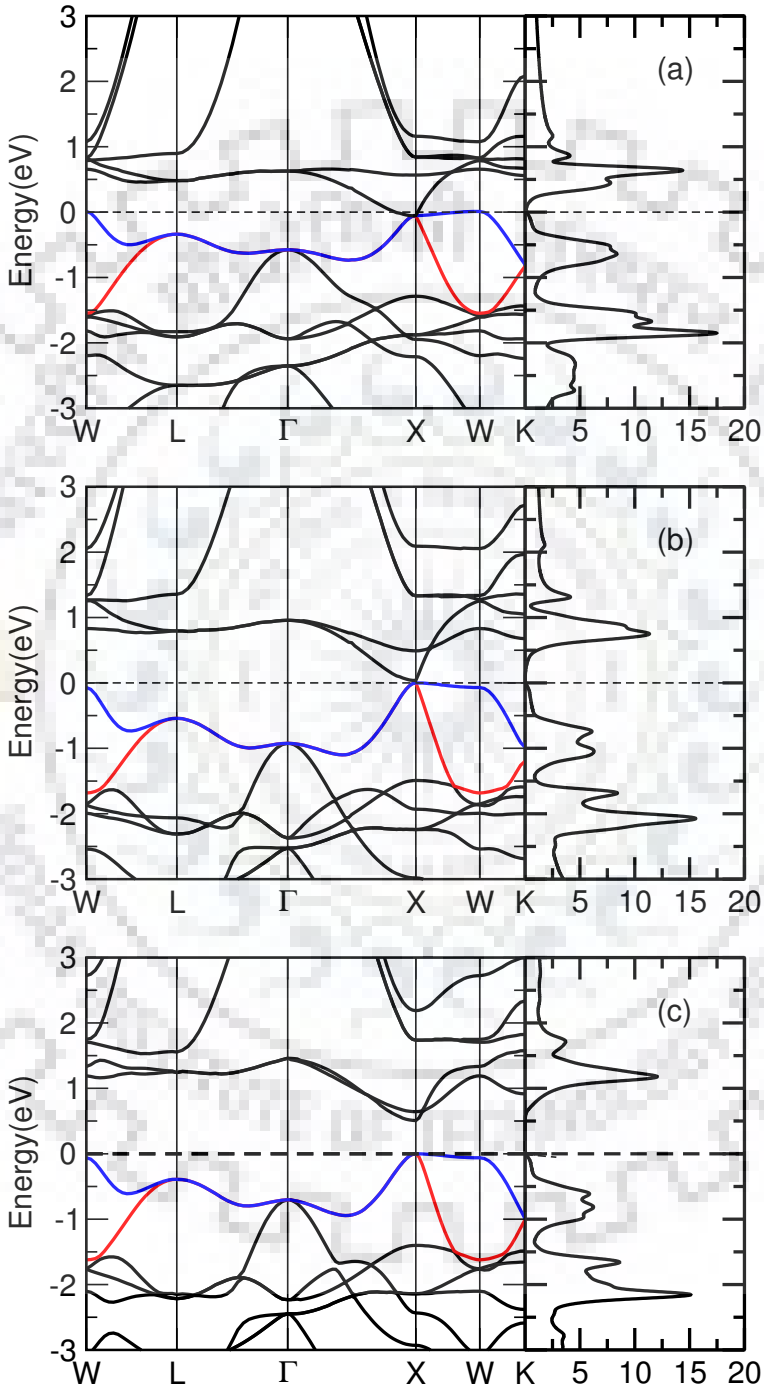

Figure 2.3: (a-c) Calculated electronic structures for CoCrIn, CoMoIn, and CoWIn, respectively, in $F\bar{4}3m$ symmetry. The top of the valence band is taken as zero on the energy axis.

efficient and electrical conductivity on doping reflects that the maximum PF is obtained when the Fermi level is near the band edge. Next, the individual systems are discussed.

First, to check the reliability of the calculations, the results were compared with the well-known CoTiSb system. The CoTiSb was chosen as the reference since the interest is in unreported CoYZ systems. Also, out of 9 CoYZ systems, CoTiSb is most studied in theory and experiment by different groups [52, 124, 165, 10, 107, 145, 166, 125, 144]. The calculated transport properties for CoTiSb are shown in Fig. 2.4(a-d). Figure 2.4(a) shows the behavior of calculated and experimental PF/τ with temperature. In order to compare the theory with experiment, one has to multiply the calculated PF by relaxation time, τ. Here, the reverse approach was employed and the reported PF was divided by τ to obtain the experimental PF/τ. Since there were no prior calculated τ values for CoTiSb, the reported electrical conductivity values were utilized to obtain the τ. In a crude approximation, the τ was approximated by using $\tau = \sigma_{exp}/\sigma_{cal}$. This way the τ was found to be of the order of 10^{-16} s. Incorporating an average value of $\tau = 2$ x 10^{-16} into PF, reported by Sekimoto et al. [124] and Birkel et al. [10], a nice agreement was obtained between calculated and reported PF/τ (Fig. 2.4(a)). This encouraged to study the CoTiSb with different doping concentrations, and compare with previously calculated and experimental values.

Figure 2.4(b) shows PF/τ for different doping concentrations at 300 K, 700 K, and 900 K. The high temperatures were chosen for study because the practical applicability of hH alloys requires high-temperature sustainability. For all temperatures, PF increased substantially on both electron and hole doping and then dropped at higher doping levels. However, hole doping dominated for all temperatures. The improvement in PF for both n-type and p-type doping in CoTiSb has already been reported by many groups [165, 107, 145, 166, 125, 144]. The peak value of calculated PF/τ at 300 K was obtained for 0.12 hole doping, at 700 K for 0.20 hole doping, and at 900 K for 0.22 hole doping per unit cell. These doping concentrations are quite pragmatic and could be realized experimentally. For instance, the 0.12 hole doping for 300 K could be realized by substituting 12% Sb by Sn or 12% Co by Fe. This is in stark agreement with previously calculated and reported values. Yang et al. calculated that 15% hole doping could lead to maximum PF at 300 K [152]. Wu et al. reported a maximum PF of 23 μW cm^{-1} K^{-2} at 850 K for $Co_{0.85}Fe_{0.15}TiSb$ [145]. In calculations of this chapter, the maximum calculated PF/τ was 2×10^{16} μW cm^{-1} K^{-2} s^{-1} at 900 K for 0.22 hole doping per unit cell. The corresponding Seebeck coefficient, S, and electrical conductivity with respect to relaxation time, σ/τ, were 173 μV K^{-1} and 0.63 $\times 10^{18}$ S cm^{-1} s^{-1}, respectively. The value of Seebeck coefficients lies well in the range of reported Seebeck coefficient for hole doped CoTiSb [145, 125, 144].

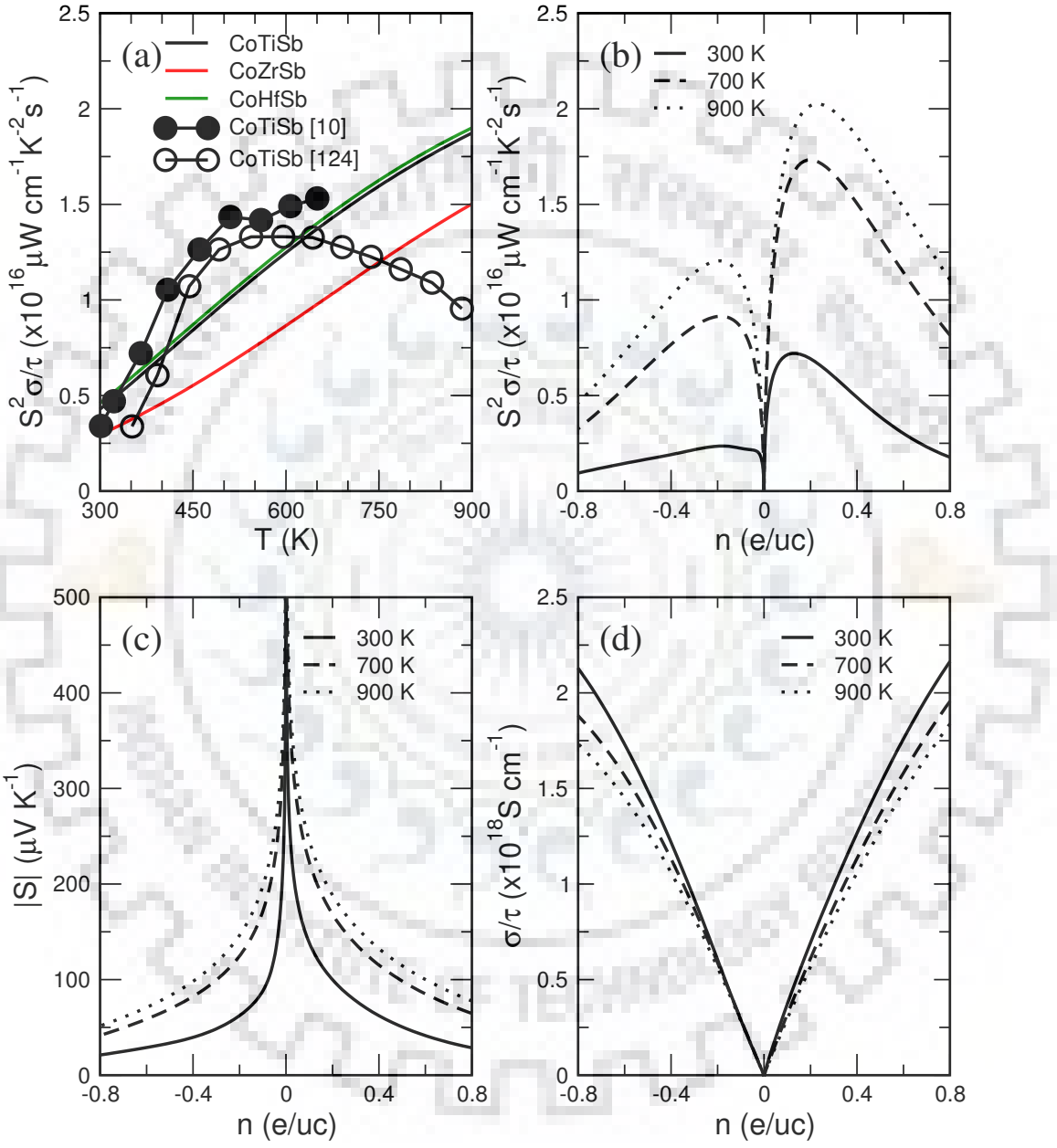

Figure 2.4: (a) Calculated and experimental power factor as a function of temperature for CoTiSb, along with calculated power factor for CoZrSb and CoHfSb. (b-d) Power factor, Seebeck coefficient, and electrical conductivity on doping CoTiSb at 300 K, 700 K, and 900 K. Power factor and electrical conductivity are plotted with respect to relaxation time.

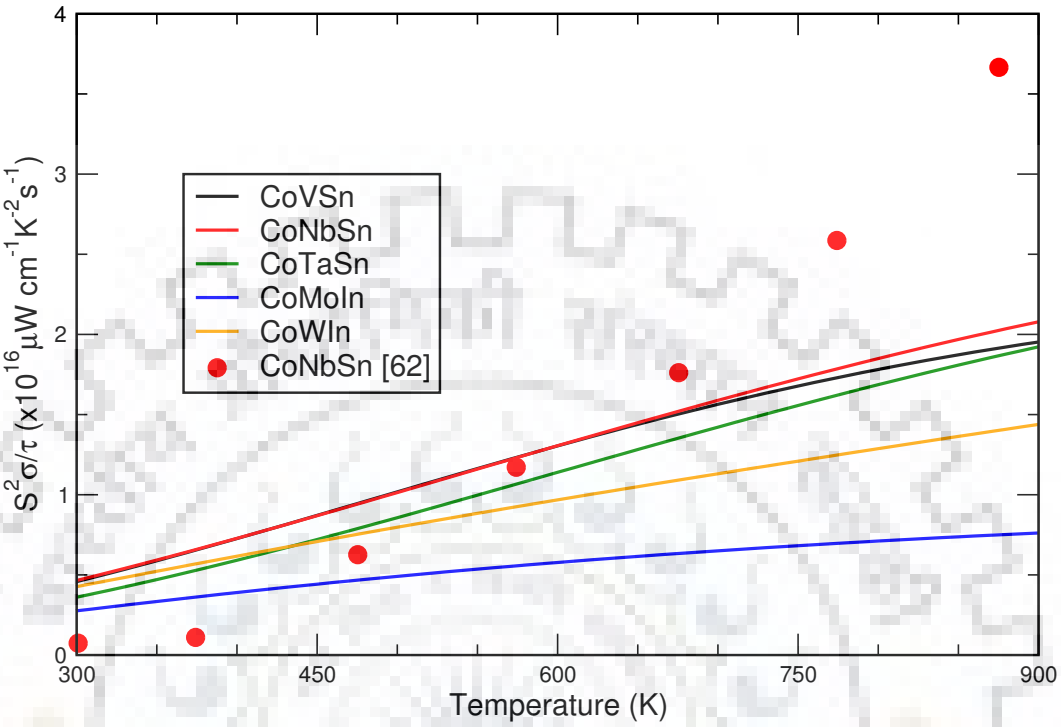

Figure 2.5: Calculated power factor, with respect to relaxation time, as a function of temperature for V-group and Cr-group, along with experimental power factor for CoNbSn.

Once it was established that the calculated transport properties for CoTiSb were in accordance with reported work, the next systems, i.e., V-group and Cr-group were studied. According to the literature, CoVSn, CoNbSn, and CoTaSn are reported in theory and experiment. However, the transport properties of CoVSn and CoTaSn are yet to be studied in detail. Before exploring the transport properties of CoVSn, CoTaSn, and Cr-group, the analysis of calculated transported properties of CoNbSn with reported values is demonstrated.

Figure 2.5 shows the PF/τ as a function of temperature for V-group, Cr-group, and reported CoNbSn. Once again, to correlate the calculated and reported values, the same strategy was employed, i.e., $\tau = \sigma_{exp}/\sigma_{cal}$. The approximation provided the relaxation time of the order of 10^{-16} s. Incorporating the calculated τ values at different temperatures into PF reported by He et al. [62], a close agreement in the range of 300-700 K was observed between calculated and reported PF/τ (Fig. 2.5). However, at higher temperatures, the reported PF/τ deviates from the calculated values. But this is not a matter of concern since the trend of PF/τ is more important. Unfortunately, the PF/τ for Cr-group was almost half of the order of V-group. Nevertheless, a nice agreement was found between the calculated and reported values for CoTiSb and CoNbSn system and an appreciable

enhancement in TE properties was observed on doping. This motivated to consider the importance of doping for V-group and Cr-group also. Thus, the systems of interest and their transport properties as a function of doping are discussed below.

2.1.5 Effects of doping and temperature on transport properties

Figure 2.6 shows the transport properties of V-group and Cr-group at 700 K and 900 K. The trend of Seebeck coefficient and electrical conductivity is explained before. For all the systems at 700 K and 900 K, Seebeck coefficient tends to fall whereas electrical conductivity tends to improve at higher doping levels. The behavior of Seebeck coefficient is in quite good agreement with Mott equation and improving the carrier concentration will definitely enhance the electrical conductivity. Figure 2.6(c) and 2.6(f) show the PF/τ as a function of doping at 700 K and 900 K, respectively. Again, the trend of PF/τ was same for all the systems. For all the temperatures, PF/τ increased substantially on both electron and hole doping and then dropped at higher doping levels. However, hole doping dominated for all the systems. The maximum PF/τ was obtained near the band edge in all cases, owing to high Seebeck coefficient when the Fermi level was near the band edge. Table 2.2 lists the doping concentration (at which maximum PF/τ was obtained), maximum PF/τ, and corresponding Seebeck coefficient and electrical conductivity at 900 K. It is easy to see that the PF/τ for V-group is of the order of CoTiSb whereas the PF/τ of Cr-group is almost half as that of the CoTiSb. In fact, the calculations suggest that at varying doping levels, the PF/τ of V-group surpasses the PF/τ of CoTiSb. The maximum PF/τ was obtained for CoNbSn, closely followed by CoTaSn, and then CoVSn. Till now, experimentalists have focused on n-type doping in CoNbSn and there was no available experimental evidence for p-type doping. Recently in 2016, He et al., while exploring the TE properties for n-type CoNbSn, broadly hinted that higher TE properties could be expected for p-type doping [62]. Here, it was found that CoNbSn could be a potential TE material on p-type doping and is in agreement with previous theoretical prediction [152]. The recently discovered member of the hH family, CoTaSn, could also be a promising p-type TE material. In a recent work, Bhattacharya et al. also predicted the TE potential of CoTaSn on p-type doping [7]. The experimental realization of CoTaSn [157] and the theoretical predictions in this chapter provide an interesting platform for experimentalists. CoVSn also showed promising TE properties on p-type doping. Recently, David J. Singh and group also predicted the high TE performance of the p-type doped CoVSn [127]. Lue et al. synthesized CoVSn with partial atomic disordering and suggested that CoVSn could be stable and can be produced at least with partial disordering [98]. But unfortunately, there has been no study on CoVSn

Compound	Doping (e/uc)	$S^2\sigma/\tau$ ($\times 10^{16}$- μW cm^{-1} K^{-2})	S (μV K^{-1})	σ/τ ($\times 10^{18}$- S cm^{-1} s^{-1})
CoTiSb	0.22	2.02	179	0.63
CoVSn	0.26	2.10	175	0.69
CoNbSn	0.21	2.33	170	0.81
CoTaSn	0.23	2.24	169	0.80
CoMoIn	0.03	1.16	136	0.61
CoWIn	0.03	1.52	170	0.54

Table 2.2: Optimum *p*-type doping concentration at 900 K for CoTiSb, V-group, and Cr-group at which maximum power factor is obtained. Also at optimum doping concentration, power factor, Seebeck coefficient, and electrical conductivity are shown. Power factor and electrical conductivity are shown with respect to relaxation time.

since then.

The Cr-group exhibited minimum PF/τ and this can be attributed to their band structure. The VBM of Cr-group was somewhat non-dispersed as compared to dispersed bands in VBM of V-group. Flat bands are an indication of weak interactions between atoms. The charge carriers in flat band region are acted upon by two or more atoms, thereby reducing their mobility. This leads to the heavier effective mass of charge carriers and high Seebeck coefficient.

Note that the calculated PF values for different doping concentrations depend highly on relaxation time. The approximate value of relaxation time for CoTiSb, $\tau = 2 \times 10^{-16}$ s, which was used to compare the calculated PF/τ with reported PF/τ, cannot be utilized for doped CoTiSb. This is because the relaxation time may vary on doping the system. To validate the point, a comparison between the calculated PF at 900 K for CoTiSb at 0.22 hole doping with T. Wu's work [145] is analyzed. In T. Wu's work, a maximum PF of 23 μW cm^{-1} K^{-2} at 850 K for CoTiSb at 0.15 hole doping was reported. Once again, employing the same strategy as before, the relaxation time was approximated for doped CoTiSb of the order of 10^{-15} s. Using this relaxation time, the PF = 20.2 μW cm^{-1} K^{-2} at 900 K for 0.22 hole doping was obtained. This is close to the maximum PF ever achieved for doped CoTiSb system. It is expected that the actual relaxation time for the V-group and Cr-group on hole doping would be of the same order, i.e., 10^{-15} s. Assuming $\tau = 10^{-15}$ s for doped V-group and Cr-group, the proposed values of PF are 21, 23, 22, 11, and 15 μW cm^{-1} K^{-2} for CoVSn (at 0.26 *p*-type doping), CoNbSn (at 0.21 *p*-type doping), CoTaSn (at

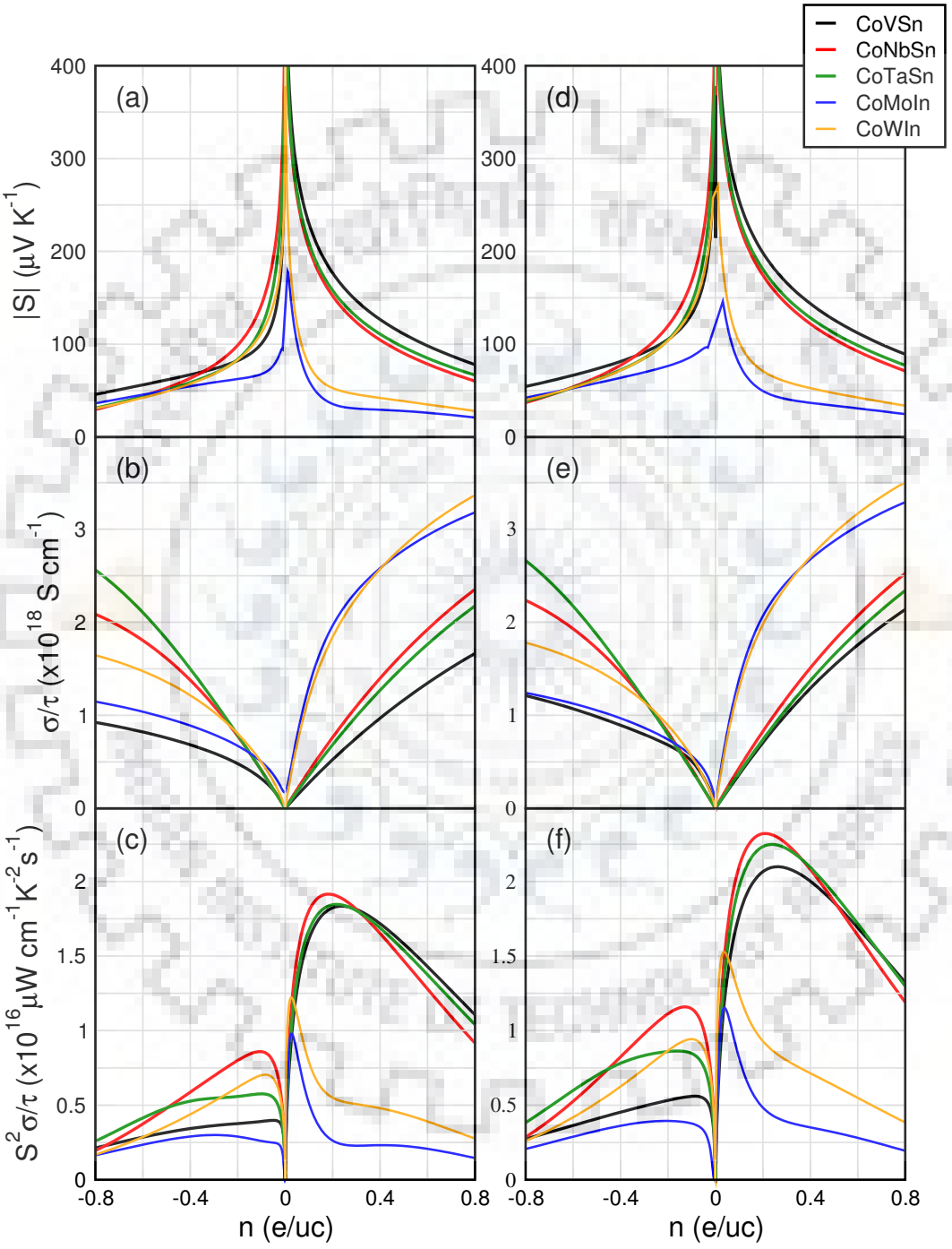

Figure 2.6: Seebeck coefficient, electrical conductivity, and power factor as a function of doping at (a-c) 700 K and (d-f) 900 K. Power factor and electrical conductivity are plotted with respect to relaxation time.

0.23 *p*-type doping), CoMoIn (at 0.03 *p*-type doping), and CoWIn (at 0.03 *p*-type doping), respectively.

2.2 Discussion and Conclusions

Till now, the main focus in 18-VEC half-Heusler alloys is centered on MNiSn and MCoSb, where M = Ti, Zr, Hf. The emphasis is on tailoring the properties of existing materials. However, the ZT value is yet to see the progressive increment. This motivates finding new plausible 18-VEC half-Heusler alloys along with improving the thermoelectric properties of existing materials. The interplay between theory and experiment had been fruitful in designing new materials. In this chapter, a similar theoretical approach was utilized for predicting new Co-based half-Heusler alloys and exploring the thermoelectric properties of existing ones. However, the theoretical prediction of new materials is relatively easier as compared to experimental realization. The manifesting challenges for experimentalists are to synthesize the ordered compositions and the vulnerability of half-Heusler alloys for anti-site disorder. The partial disordering and anti-site disorder may affect the properties significantly.

Here, the systematic investigation of nine 18-VEC CoYZ systems in $F\bar{4}3m$ and $P6_3/mmc$ symmetry was performed. All nine systems were found to be metallic in $P6_3/mmc$ symmetry and semiconductors, except CoCrIn, in $F\bar{4}3m$ symmetry. The V-group was found to have indirect band gap whereas Cr-group possesses direct band gap. The stability of V-group and Cr-group was confirmed by phonon calculations. The transport properties of V-group and Cr-group were found to be more promising on hole doping. The hole doped CoNbSn system is proposed to be a more promising thermoelectric material than the existing electron doped CoNbSn systems. Also, CoVSn, CoNbSn, and CoTaSn, at 900 K, showed higher power factor than the well-known CoTiSb on 0.26, 0.21, and 0.23 hole doping per unit cell, respectively. The values of thermopower for hole doped V-group and Cr-group ranges from 136 to 175 μV K^{-1} at 900 K. This work could be a motivation to experimentalists to synthesize CoVSn, CoMoIn, CoWIn, and improve the thermoelectric properties of existing CoNbSn and CoTaSn by doping.

Chapter 3

Thermal Transport Properties of Cobalt Based Half-Heusler Alloys

This chapter is categorized into three sections: I) Introduction II) Electrical and thermal transport properties and III) Discussion and Conclusions. The introduction section emphasizes on the interplay of theory and experiment in designing new materials. The electrical and thermal transport properties of p-type doped CoVSn, CoNbSn, CoTaSn, CoMoIn, and CoWIn combining a first-principles approach with semi-classical Boltzmann transport theory are discussed in the second section. Finally, the relevance and importance of time relaxation in designing thermoelectric materials and summary of results are discussed in the last section.

3.1 Introduction

In recent years, different approaches have been adopted to enhance the efficiency of half-Heusler (hH) alloys [24]. Along with improving the thermoelectric (TE) properties of existing materials, the search for new potential hH alloys is being carried out extensively [97]. The interplay of theory and experiment for designing new materials had been fruitful in the past [153]. The theoretical prediction of stable systems allows the experimentalists to narrow down the window for targeting new materials. Recently, along with experimental realization, quite a large class of hH alloys have been predicted to be theoretically stable [54, 157]. This was the motivation to investigate specifically 18 valence electron count (VEC) hH alloys, which were not studied in depth so-far.

In the previous chapter, the cobalt-based 18-VEC hH systems CoVSn, CoNbSn, CoTaSn, CoCrIn, CoMoIn, and CoWIn, using the first-principles approach were screened.

The static and dynamic stability, electronic structure, and electrical transport properties of these systems were systematically investigated. The calculations suggested that all these systems, except for CoCrIn, could be potential TE materials on p-type doping. Assuming relaxation time, $\tau = 10^{-15}$ s, a maximum power factor (PF) was calculated of 21, 23, 22, 11, and 15 μW cm^{-1} K^{-2} at 900 K for CoVSn (at 0.26 p-type doping), CoNbSn (at 0.21 p-type doping), CoTaSn (at 0.23 p-type doping), CoMoIn (at 0.03 p-type doping), and CoWIn (at 0.03 p-type doping), respectively [158]. To establish the thermoelectric potential of any material, it is of key importance to evaluate the efficiency of a TE material given by the dimensionless figure of merit $ZT = S^2\sigma T/\kappa$ ($\kappa = \kappa_e + \kappa_l$), where S is Seebeck coefficient, σ is electrical conductivity, and κ is thermal conductivity comprising of electronic and lattice contributions [41, 162, 71, 46].

In this chapter, the thermal conductivity and thereby ZT, of p-type doped CoVSn, CoNbSn, CoTaSn, CoMoIn, and CoWIn are determined combining a first-principles approach with semi-classical Boltzmann transport theory.

3.2 Electrical and Thermal Transport Properties

The rigid band approximation (RBA), semi-classical Boltzmann theory, and constant relaxation time approach were employed to calculate the electrical transport properties. It was established previously that the maximum PF for CoTiSb was obtained on p-type doping. The calculations of the PF/τ as a function of p-type doping for this system at 300, 700, and 900 K are shown in Fig. 3.1(a). The effect of doping on Seebeck coefficient and electrical conductivity reflects that the maximum PF is obtained when the Fermi level is near the band edge, which is indeed the case. The peak value of calculated PF/τ, at 300 K was obtained for 0.12 p-type doping, at 700 K for 0.20 p-type doping, and at 900 K for 0.22 p-type doping per unit cell. This is in good agreement with previously calculated and reported values [152, 145]. As the predicted doping levels are in agreement with previously reported values and the optimal doping levels should be quite achievable experimentally, the PF, thermal conductivity, and ZT as a function of temperature are determined next. Since, in the last chapter, the maximum PF was obtained at 900 K for 0.22 p-type doping, the following is focussed on 0.22 p-type doped CoTiSb.

Figure 3.1(b) shows the PF as a function of temperature for calculated 0.22 p-type doped CoTiSb and reported 0.15 Fe-doped CoTiSb, i.e., $Co_{0.85}Fe_{0.15}TiSb$ [145]. To compare the theory with experiment, an approximate value of relaxation time, $\tau = 10^{-15}$ s was used. This value was arrived at by comparing the calculated and reported electrical

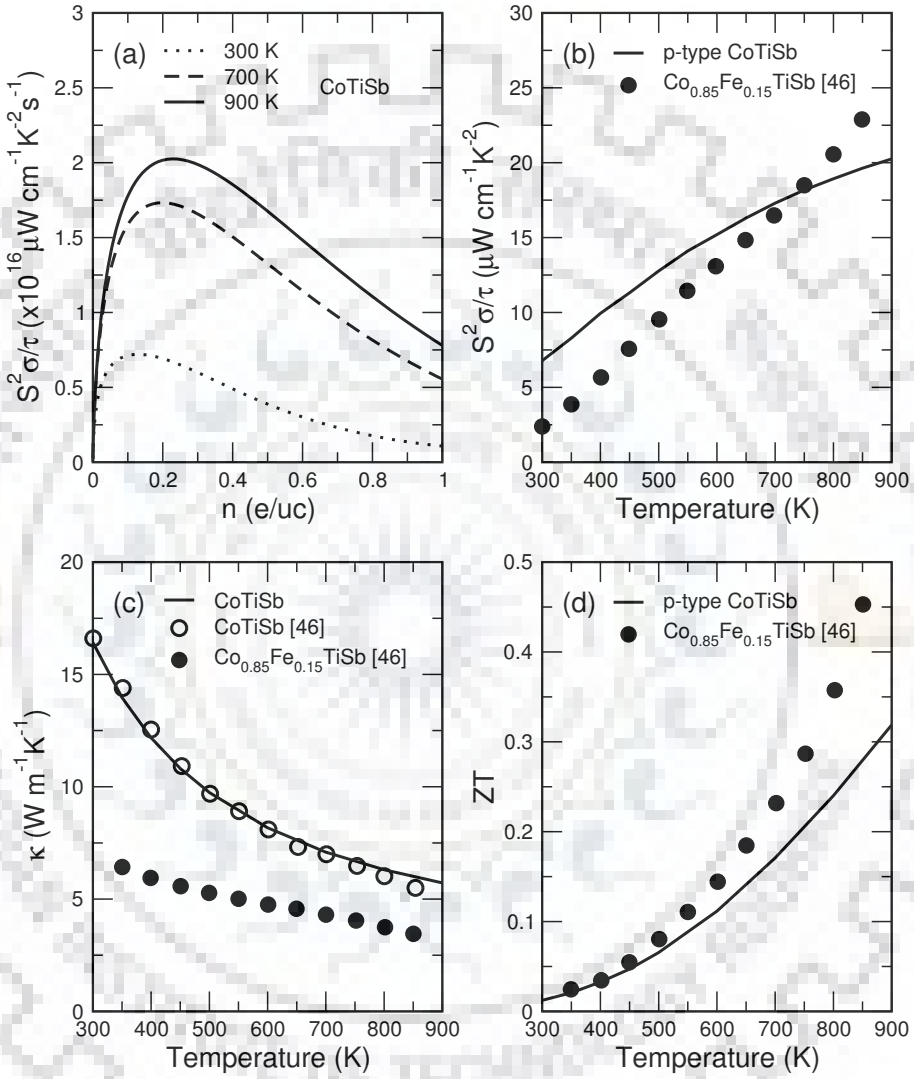

Figure 3.1: (a) Calculated power factor, with respect to relaxation time, on p-type doping CoTiSb at 300, 700, and 900 K. (b) Power factor as a function of temperature for calculated 0.22 p-type doped CoTiSb and reported 0.15 Fe-doped CoTiSb. (c) Thermal conductivity as a function of temperature for calculated CoTiSb, reported CoTiSb, and reported 0.15 Fe-doped CoTiSb. (d) ZT as a function of temperature for calculated 0.22 p-type doped CoTiSb and reported 0.15 Fe-doped CoTiSb. Reported parent CoTiSb and 0.15 Fe-doped CoTiSb are represented by open and filled circles, respectively.

conductivity of 0.22 p-type doped CoTiSb. This strategy had been helpful in the previous chapter and a considerable agreement for cobalt-based 18-VEC systems was obtained [158]. Assuming $\tau = 10^{-15}$ s, the trend of calculated PF for 0.22 p-type doped CoTiSb and reported PF for 0.15 Fe-doped CoTiSb was quite similar. Both calculated and reported PF values were continuously increasing with temperature. The slight deviation in magnitude of PF was because the calculated values were for the pristine system. After obtaining a similar trend for the calculated and reported PF for the p-type doped system, next, the thermal conductivity for CoTiSb was calculated.

The trend of κ as a function of temperature for calculated CoTiSb, reported CoTiSb, and reported 0.15 Fe-doped CoTiSb is shown in Fig. 3.1(c). The value of calculated κ was approximated tenfold lower to match the experimental results. Both calculated and reported κ, as expected, were decreasing with temperature. The calculated and reported κ for parent CoTiSb were in good agreement. The κ of reported 0.15 Fe-doped CoTiSb is almost threefold lower than that of parent CoTiSb at 300 K. This shows the importance of doping effect for a TE material. The calculated κ for parent CoNbSn and reported CoNbSn were further compared and a good agreement was found in the range of 600 K to 900 K [62]. However, the difference was smaller at higher temperatures. After estimating the values of PF for 0.22 p-type doped CoTiSb and κ for parent CoTiSb, as a next step, the efficiency, i.e., ZT for the same was calculated.

Figure 3.1(d) shows the ZT as a function of temperature for the calculated 0.22 p-type doped CoTiSb and reported 0.15 Fe-doped CoTiSb. The ZT values were increasing with temperature owing to the reduction in κ at higher temperatures. A nice agreement can be seen in the range of 300 K to 600 K. Beyond that, experimental values dominated the calculated values. This is quite expected since to calculate ZT ($=S^2\sigma T/\kappa$) of p-type doped CoTiSb, the κ values of parent CoTiSb were incorporated. It is known that κ decreases on doping, therefore, the calculated ZT values are expected to lag behind the experimental values. The maximum calculated ZT value for 0.22 p-type doped CoTiSb was 0.31 whereas 0.45 was reported for 0.15 Fe-doped CoTiSb. The calculated ZT for 0.22 p-type doped CoTiSb is slightly underestimated in comparison to reported 0.15 Fe-doped CoTiSb.

The slight deviations in the calculated values for 0.22 p-type doped CoTiSb and reported 0.15 Fe-doped CoTiSb can be further attributed to the fact that the calculated electrical transport properties for p-type doped systems were, in general; rather than considering a particular atom for doping. For instance, one could tune the properties by doping Co by Fe, Ru, Mn or V, or by doping Sb by Sn, Ge, or In, and properties may vary depending on the choice of atoms. This is quite evident from two similar works on p-type

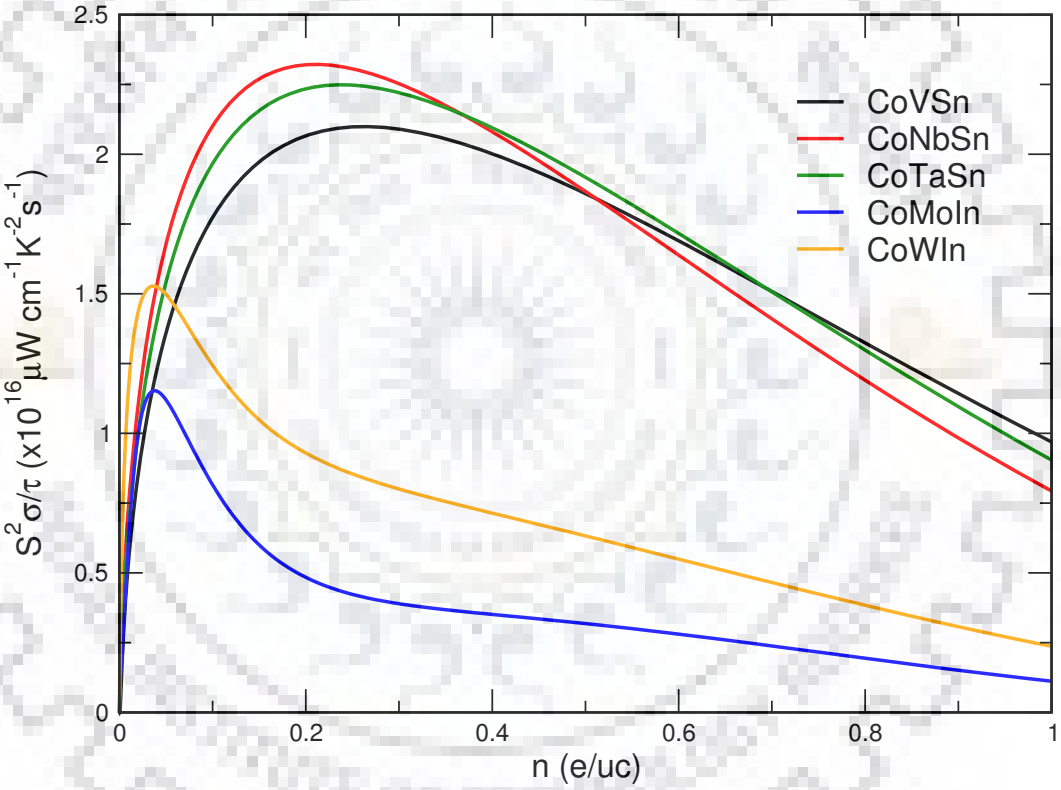

Figure 3.2: The trend of power factor, with respect to relaxation time, on *p*-type doping CoVSn, CoNbSn, CoTaSn, CoMoIn, and CoWIn at 900 K.

doping in CoTiSb. On 15% doping at Sb site by Ge in CoTiSb, Wu et al. reported a PF of 9 μW cm^{-1} K^{-2} at 850 K [144]. However, the same group reported a high PF of 23 μW cm^{-1} K^{-2} at 850 K on 15% doping at Co site by Fe [145]. Hence, it can be concluded that at same doping levels and operating temperature, the value of PF may vary significantly with dopant atom. Overall, a nice agreement was obtained between the calculated TE parameters and reported values for p-type doped CoTiSb. Next, the TE properties of chosen systems are analyzed.

The trend of PF/τ as a function of p-type doping for CoVSn, CoNbSn, CoTaSn, CoMoIn, and CoWIn at 900 K is shown in Fig. 3.2. For all the systems, maximum PF was obtained on p-type doping and all optimal doping levels were small and could be achieved experimentally. Table 3.1 lists the optimal doping levels at which maximum PF was obtained, along with maximum PF and ZT for all the systems at 900 K. As can be seen from Table 3.1, the maximum PF was obtained for CoNbSn, followed by CoTaSn, and then CoVSn. It can be proposed that p-type doped CoVSn, CoNbSn, and CoTaSn have higher PF than the well-known CoTiSb system. Recently, the p-type doped CoVSn is predicted to have high thermoelectric performance [127]. Also, CoNbSn is predicted to have a higher PF on p-type doping [152]. However, the PF for CoMoIn and CoWIn were low as compared to other p-type doped systems. Nevertheless, CoMoIn and CoWIn are expected to have lowest thermal conductivity on account of phonon scattering from heavy atoms of $4d$ and $5d$ transition elements.

The behavior of κ as a function of temperature for all the systems is shown in Fig. 3.3. The inset of Fig. 3.3 indicates the behavior of κ_l with temperature. It is evident that κ_l plays a major part in total thermal conductivity. As discussed earlier, the κ values were approximated tenfold lower for all the systems. The approximation seems valid since the trend for reported and calculated values for CoTiSb are in quite good agreement. The trend of κ was decreasing with temperature for all the systems with maximum κ obtained for CoTiSb whereas minimum κ was obtained for CoMoIn and CoWIn. The lower κ of CoMoIn and CoWIn can be attributed to the scattering of phonons by heavy elements of $4d$ and $5d$ transition metal series. The most important observation, from Fig. 3.3, is that κ for CoMoIn and CoWIn is almost threefold lower than that of CoTiSb at 300 K. This will significantly affect the ZT values for CoMoIn and CoWIn, despite having a low PF as compared to other systems.

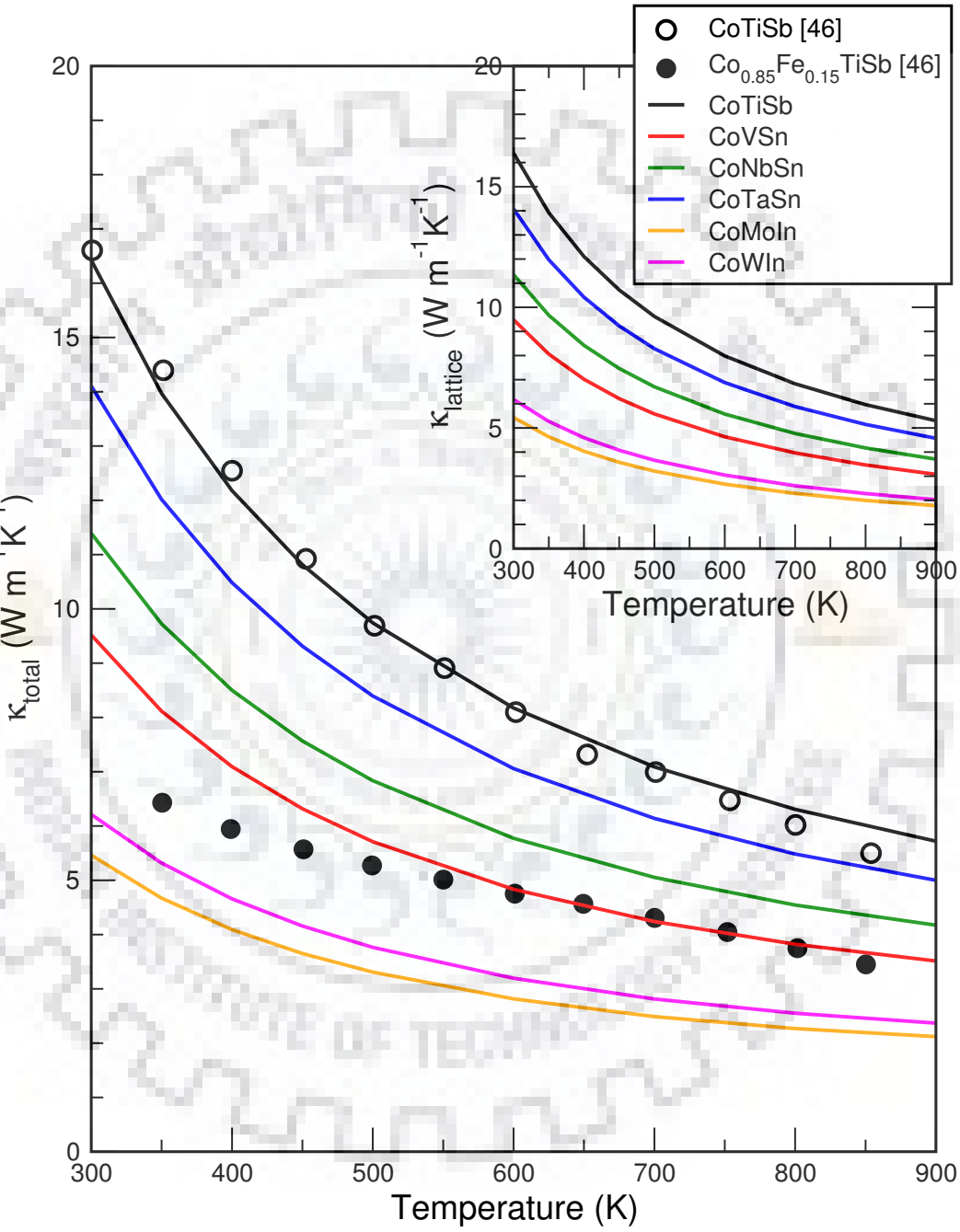

Figure 3.3: The trend of thermal conductivity as a function of temperature. The inset of the figure indicates the behavior of lattice thermal conductivity with temperature. Reported parent CoTiSb and 0.15 Fe-doped CoTiSb are represented by open and filled circles, respectively.

System	Doping (e/uc)	$S^2\sigma$ (μW cm^{-1} K^{-2})	ZT
CoTiSb	0.22	20.2	0.31
CoVSn	0.26	21	0.53
CoNbSn	0.21	23.3	0.5
CoTaSn	0.23	22.4	0.4
CoMoIn	0.03	11.6	0.49
CoWIn	0.03	15.2	0.57

Table 3.1: The maximum power factor ($S^2\sigma$) and figure of merit (ZT) at optimum doping concentrations for p-type doped systems at 900 K, assuming $\tau = 10^{-15}$ s.

3.2.1 Evaluation of Figure of Merit

Next, the ZT ($=S^2\sigma T/\kappa$) values for p-type doped systems were determined by incorporating the calculated κ of parent compounds into the expression for ZT. Since the κ of the parent compound reduces significantly on doping, the calculated ZT values for all the systems are actually *underestimated*. Assuming $\tau = 10^{-15}$ s, the figure of merit ZT for all the systems at optimal p-type doping levels at 900 K is shown in Table 3.1. The ZT values of all the proposed systems were higher than CoTiSb on p-type doping. Despite having low PF, the maximum ZT was obtained for CoWIn on account of lower κ. A high reported ZT value for 0.22 p-type doped CoTiSb was 0.45 at 850 K [145]. This shows that the calculated value of ZT for p-type doped CoTiSb is not far behind than the reported one despite using the κ of undoped CoTiSb. Hence, the ZT values of the proposed p-doped systems may be higher than the proposed values. On a quantitative scale, the reported ZT of considered 0.22 p-type doped CoTiSb was 1.46 times than that of the calculated ZT. Using the same factor for CoWIn, a high ZT of 0.83 was obtained. Since the dopant is not specified, the actual value of the figure of merit may even reach unity, i.e., $ZT \sim 1$ for p-doped CoWIn.

3.3 Discussion and Conclusions

Since the relaxation time depends on temperature and doping levels, the trend of relaxation time with temperature for base composition CoTiSb and p-doped CoTiSb based systems were carefully analyzed. To analyze the trend, the ratio of reported and calculated electrical conductivity was utilized to obtain an approximate value of relaxation time. For base composition CoTiSb, as expected, the relaxation time was decreasing with temperature. The change in relaxation time was found to be considerable at lower temperatures,

however, the change in values was smaller at higher temperatures. Because the results are proposed for high-temperature thermoelectric performance of cobalt-based systems, the small variations in relaxation time at a higher temperature may not affect the predicted results.

Since the predicted optimal doping levels for CoVSn, CoNbSn, and CoTaSn are close to that of reported p-doped CoTiSb, the actual relaxation time will not affect the proposed results much. Moreover, for p-doped CoTiSb, the observed relaxation time over the entire temperature range was of the order, $\tau = C$ x 10^{-15} s, where C is a number which depends on temperature. The value of C was slightly more than 1 in the range of 600-900 K. In this chapter, this number was ignored and only $\tau = 10^{-15}$ s was utilized. Definitely, any value larger than 1 of C will improve the thermoelectric performance. Hence, it can be stated that the proposed values are slightly underestimated in context of relaxation time and likely to improve on employing exact relaxation time. A similar trend of relaxation time was observed for CoNbSn. Therefore, it is expected that for cobalt-based 18-VEC hH alloys, a relaxation time would be of the order of 10^{-15} s. Hence, the calculated values for CoMoIn and CoWIn are also acceptable.

To summarize, all the systems showed a higher power factor than well-known CoTiSb on p-type doping. The κ for undoped CoMoIn and CoWIn was almost threefold lower than that of CoTiSb at 300 K, indicative of good thermoelectric properties at room temperature. The maximum figure of merit ZT was 0.57 for 0.03 p-typed doped CoWIn at 900 K. The ZT values for all the p-type doped systems were expected to be higher than the proposed values since the κ of undoped systems was employed. These calculations provide a clear indication for the promising thermoelectric properties of p-type doped CoVSn, CoNbSn, CoTaSn, CoMoIn, and CoWIn and will hopefully motivate growing these materials with optimal doping concentrations for higher performance thermoelectric applications.

Chapter 4

FeTaSb and FeMnTiSb As Promising Thermoelectric Alloys.

In this chapter, the role of two Fe-based alloys FeTaSb and FeMnTiSb as potential thermoelectric (TE) materials is discussed with the help of *ab initio* electronic structure calculations, semiclassical Boltzmann transport theory, and rigid band approximation.

4.1 Introduction

*M*NiSn and *M*CoSb (where M = Ti, Zr, Hf) are the two pioneer and most studied half-Heusler (hH) classes [6, 24]. A high ZT of 1.05 and 0.8 near 900-1000 K has been reported for the n-type $Hf_{0.6}Zr_{0.4}NiSn_{0.995}Sb_{0.005}$ hH alloy and p-type $Hf_{0.3}Zr_{0.7}CoSn_{0.3}Sb_{0.7}$/nano-$ZrO_2$ composites, respectively [115]. But the drawback of these materials is the expensive Hf as the major constituent. The quest for higher ZT and low-cost materials shifted the focus towards a new promising hH class *M*FeSb (M = V, Nb, and Ta). The $5d$ element Ta, though expensive, can be used for doping a small amount in FeVSb or FeNbSb to improve the TE properties. Within a short span of time, a lot of work has been reported in this family [40, 27, 167, 168, 170]. A high power factor (PF), $S^2\sigma$, of 48 μW cm^{-1} K^{-2} at 350 K is reported for FeVSb system. Despite a high PF, the maximum reported ZT is 0.25 at 550 K owing to a high thermal conductivity of FeVSb [47]. Doping attempts record the highest ZT of 0.8 at 900 K [50]. More interestingly, FeNbSb based hH alloys have been reported to exhibit $ZT > 1$ [45, 46]. A record peak ZT of 1.6 is achieved for $Nb_{0.6}Ta_{0.4}Ti_{0.2}FeSb$ at 1200 K [156]. The least explored member FeTaSb of the family has a patent filed in 2015 on a theoretical approach [121]. Recently, it has been predicted as a p-type hH candidate [7].

In this chapter, a systematic investigation of the thermodynamic stability, dynamical stability, and thermal and electrical transport properties of FeTaSb and FeMnTiSb in cubic $F\bar{4}3m$ symmetry has been carried out. The custom choice of materials was based on earlier discussion and fulfills the foremost criterion of semiconducting behavior. Also, the FeMnTiSb constitutes low-cost elements. On descending in *M*FeSb family from V to Ta, Ta being heaviest is expected to scatter the phonons effectively on account of mass difference [20]. As FeNbSb is reported to have a high *ZT*, the hopes are high from FeTaSb. This is because of the similar sizes of Nb and Ta that their electrical properties are expected to be unaltered. Further, the doping effect on TE properties of FeTaSb is considered.

Conventionally, doping amounts to replacing a certain amount of an atom by a desirable dopant, e.g., FeVSb to $FeV_{0.6}Nb_{0.4}Sb$ [48] or doping a certain amount in the void spaces. As the hH structure has the advantage of vacant lattice sites, instead of doping a small fixed amount, the introduction of a fourth atom into all available vacant lattice sites was considered. This led to the possibility of making FeTaSb a full-Heusler by doping Fe or Ta, e.g., Fe_2TaSb. However, this compound does not obey the 24-VEC Slater-Pauling criterion of a semiconductor. Introducing a different fourth atom may lead to effective phonon scattering on account of mass fluctuations [48] and as well may satisfy the Slater-Pauling rule. After analyzing different possible combinations in order to obey the Slater-Pauling rule with an introduction of the fourth atom in the crystal structure, FeMnTiSb was found to be the most suitable candidate.

The hypothetical quaternary Heusler alloy FeMnTiSb fulfills the 24-VEC semiconductor criterion, comprises low-cost elements, and is expected to have lower thermal conductivity on account of more scattering points and mass fluctuations. Moreover, the choice of Mn as the fourth atom is also suitable on account of bulk low thermal conductivity. Scanning of the literature reveals no prior experimental evidence of existence or synthesis of either FeTaSb or FeMnTiSb. Also, quaternary Heusler alloys have not been much explored in the context of thermoelectricity.

4.2 Structural Optimization and Stability

In order to determine the ground state properties, the crystal structures of FeNbSb, FeTaSb, and FeMnTiSb were optimized using GGA-PBEsol implemented in Wien2k. The crystal structures can be seen in Chapter-1. The ground state of all the three systems was found to be nonmagnetic. The total energy was minimized as a function of unit cell volume, fitted with Birch-Murnaghan equation [9], in $F\bar{4}3m$ symmetry (Fig. 4.1). There

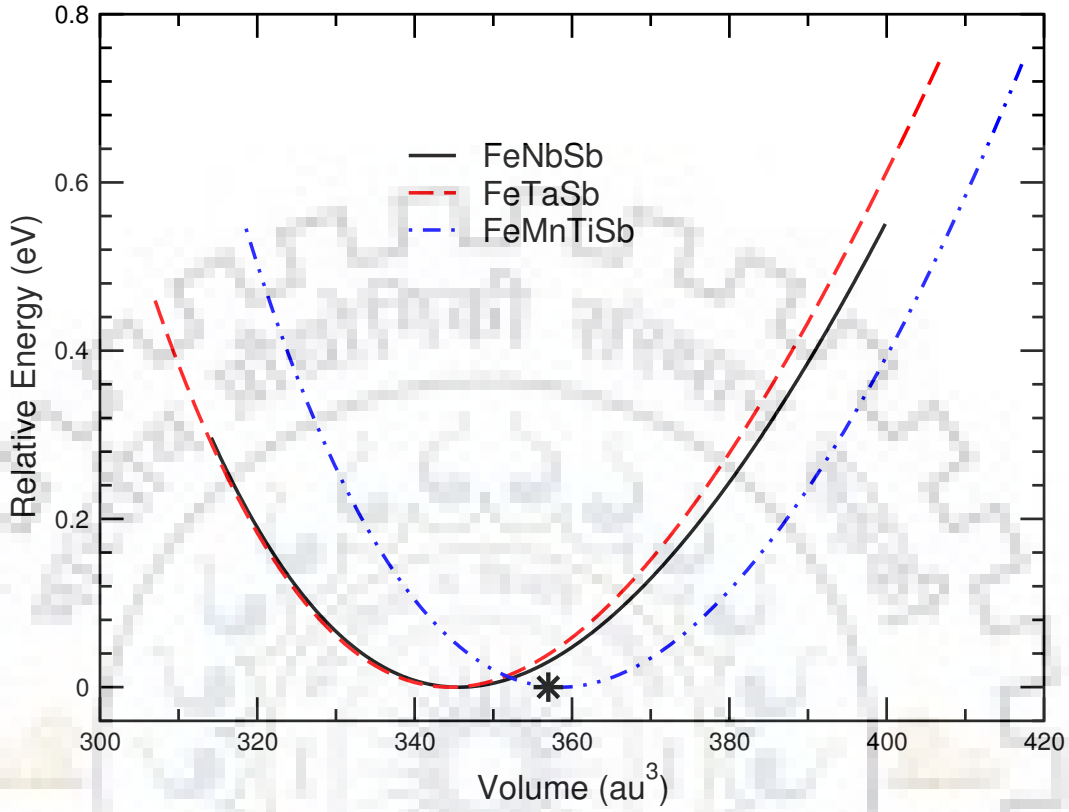

Figure 4.1: Calculated relative total energy as a function of volume for FeNbSb, FeTaSb, and FeMnTiSb in cubic $F\bar{4}3m$ symmetry. The experimentally reported volume of FeNbSb is marked by asterisk [104]. For better illustration, the energy minimum of all plots is taken as zero on energy axis.

is a slight deviation in the calculated and experimental volume of FeNbSb [104]. However, the energy well of FeTaSb is quite similar to that of FeNbSb, indicating the possibility of the existence of FeTaSb too. Furthermore, the energy profile of FeMnTiSb is also similar though somewhat shifted towards the higher volume due to the presence of the fourth atom in the unit cell. The considered systems thus can be synthesized under suitable conditions.

The lattice parameter and the band gap of all the systems are listed in Table 4.1. The calculated and experimental lattice parameters of FeNbSb are in agreement with a discrepancy of only 0.92%. The lattice parameter of FeTaSb is slightly lower than that of FeNbSb [73] which can be attributed to the effect of lanthanide contraction on post lanthanides. Though FeMnTiSb has not been reported yet, FeMnTiAs was studied in a previous *ab initio* electronic structure calculation with lattice parameter as 5.79 Å and its ground state was found to be nonmagnetic [108]. For the purpose of comparison, the calculated lattice parameter of FeMnTiSb is larger than that of FeMnTiAs, as expected,

System	a (Å)	E_g (eV)
FeNbSb	5.8950 (5.95) [104]	0.53 (0.53) [80]
FeTaSb	5.8879	0.86
FeMnTiSb	5.9769	0.31

Table 4.1: The calculated lattice parameter a and band gap E_g values of all the systems in cubic $F\bar{4}3m$ symmetry. The reported values are given in parentheses.

due to the size difference between Sb and As.

As expected, all the systems were nonmagnetic semiconductors in accordance with the Slater-Pauling rule. To the best of the knowledge, there is no experimental report on the band gap of FeNbSb. The calculated band gap of FeNbSb is in good agreement with previously calculated values [71, 40, 80]. Going from FeNbSb to FeTaSb, the increase in band gap can be explained in terms of electronegativity difference of Nb and Ta [59]. The large band gap of FeTaSb, in comparison to FeNbSb, could be helpful in suppressing the onset of bipolar conduction at high-temperature, thereby improving the TE properties at elevated temperatures [156]. FeMnTiSb had the smallest band gap among all the systems since the close proximity of atoms allows the larger overlap and more delocalization of the orbitals [136].

The optimized structures of FeNbSb, FeTaSb, and FeMnTiSb were further studied for dynamic stability with phonon calculations. Phonons are often regarded as normal modes or quantum of vibrations in a crystal. For a system to be dynamically stable, the frequency of each phonon should be real and not imaginary [39, 137]. The calculated results showed no imaginary frequencies for all the systems throughout the Brillouin zone, thus, ensuring the stability of FeNbSb, FeTaSb, and FeMnTiSb. As can be seen from Fig. 4.2, there are three acoustical and six optical branches for FeNbSb and FeTaSb whereas three acoustical and nine optical branches for FeMnTiSb. The major contribution to lattice thermal conductivity comes from the acoustical phonon branches since they have large group velocities [114].

4.2.1 Electronic Structure

The electronic structures of FeNbSb, FeTaSb, and FeMnTiSb were calculated using GGA-PBEsol. The band structure and density of states (DOS) are shown in Fig. 4.3. The electronic features of FeNbSb and FeTaSb are quite similar owing to the similar size and chemical properties of Nb and Ta. This is also reflected in the electrical transport properties

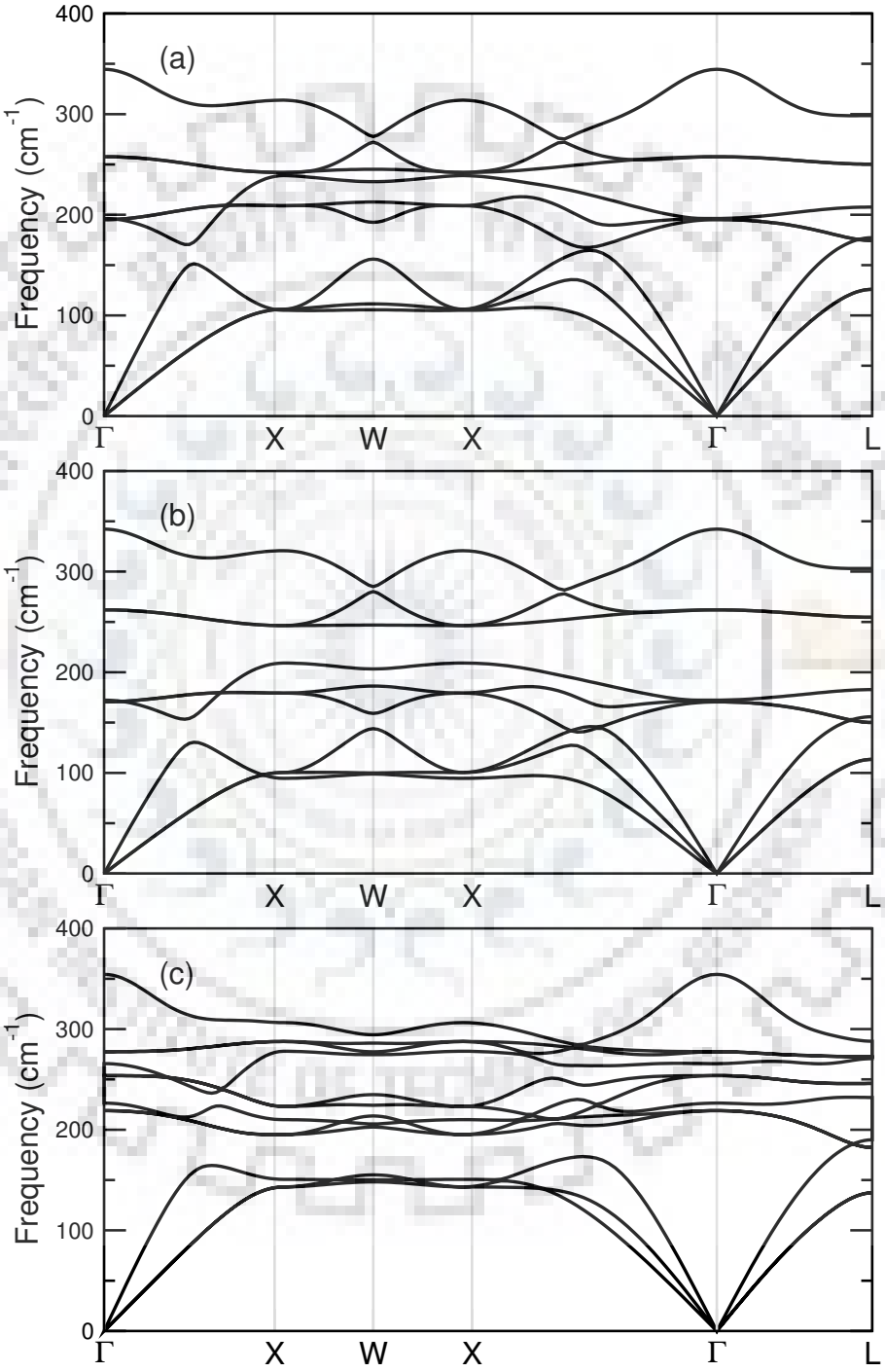

Figure 4.2: The phonon dispersion curves of (a) FeNbSb, (b) FeTaSb, and (c) FeMnTiSb, in cubic $F\bar{4}3m$ symmetry.

discussed later. The valence band maximum (VBM) is at L point whereas the conduction band minimum (CBM) is at X point for both FeNbSb and FeTaSb, i.e., indirect band gap semiconductor.

The VBM of FeNbSb and FeTaSb is twofold degenerate and comprises heavy and light bands. The heavy band enhances Seebeck coefficient whereas the light band facilitates the mobility of charge carriers. Thus, the combination of heavy and light bands is helpful in achieving good TE performance [60, 161, 151]. The DOS features showed that the VBM of FeTaSb mostly comprised d-states of Fe and some d-states of Ta, very similar to FeNbSb [96, 162]. The CBM was dominated by d-states of Fe and Ta. There was no contribution whatsoever from the Sb states. Hence, the doping at Sb site may improve the carrier concentration without affecting the band structure. Any doping at Ta position will be reflected in the CBM without affecting the VBM significantly. However, doping at Fe site will be reflected in both VBM and CBM. These theoretical considerations could be helpful for choosing the experimental doping levels. The energy dispersion of the bands suggested a p-type behavior, which was indeed confirmed by electrical transport properties [162].

In case of FeMnTiSb, the VBM is threefold degenerate whereas the CBM is twofold degenerate. The nature of the band gap is direct and VBM and CBM are located at Γ point. The VBM comprises heavy bands which are relatively flatter in the Γ-X direction than those of FeNbSb and FeTaSb. Flat bands are an indication of large effective mass which augments the Seebeck coefficient. But, a large effective mass reduces the mobility of charge carriers, thereby decreasing the electrical conductivity. These proposed effects have been observed in the electrical transport calculations discussed ahead: the Seebeck coefficient of FeMnTiSb is larger than that of FeTaSb whereas the electrical conductivity of FeMnTiSb is lower than that of FeTaSb, in both n-type and p-type doping.

The CBM of FeMnTiSb is twofold degenerate and comprises flat bands. One of the bands is almost flat in Γ-X, X-W, and W-K directions. These less dispersed bands at CBM of FeMnTiSb suggests improvement in TE performance on n-type doping as is confirmed in the coming section [149]. The DOS features showed that the VBM of FeMnTiSb comprises mostly Mn d-states, with some contribution from the d-states of Fe and Ti. The CBM is dominated by the similar contribution from the d-states of Fe and Mn. Yet again, no significant contribution of Sb states was observed at either VBM or CBM. Therefore, the doping at Sb sites may be helpful in improving the TE properties without altering the band structure. Doping at Mn site will affect considerably both VBM and CBM whereas doping at Fe position will significantly influence only the CBM of FeMnTiSb. Next, the effect of discussed electronic features on electrical transport properties is studied.

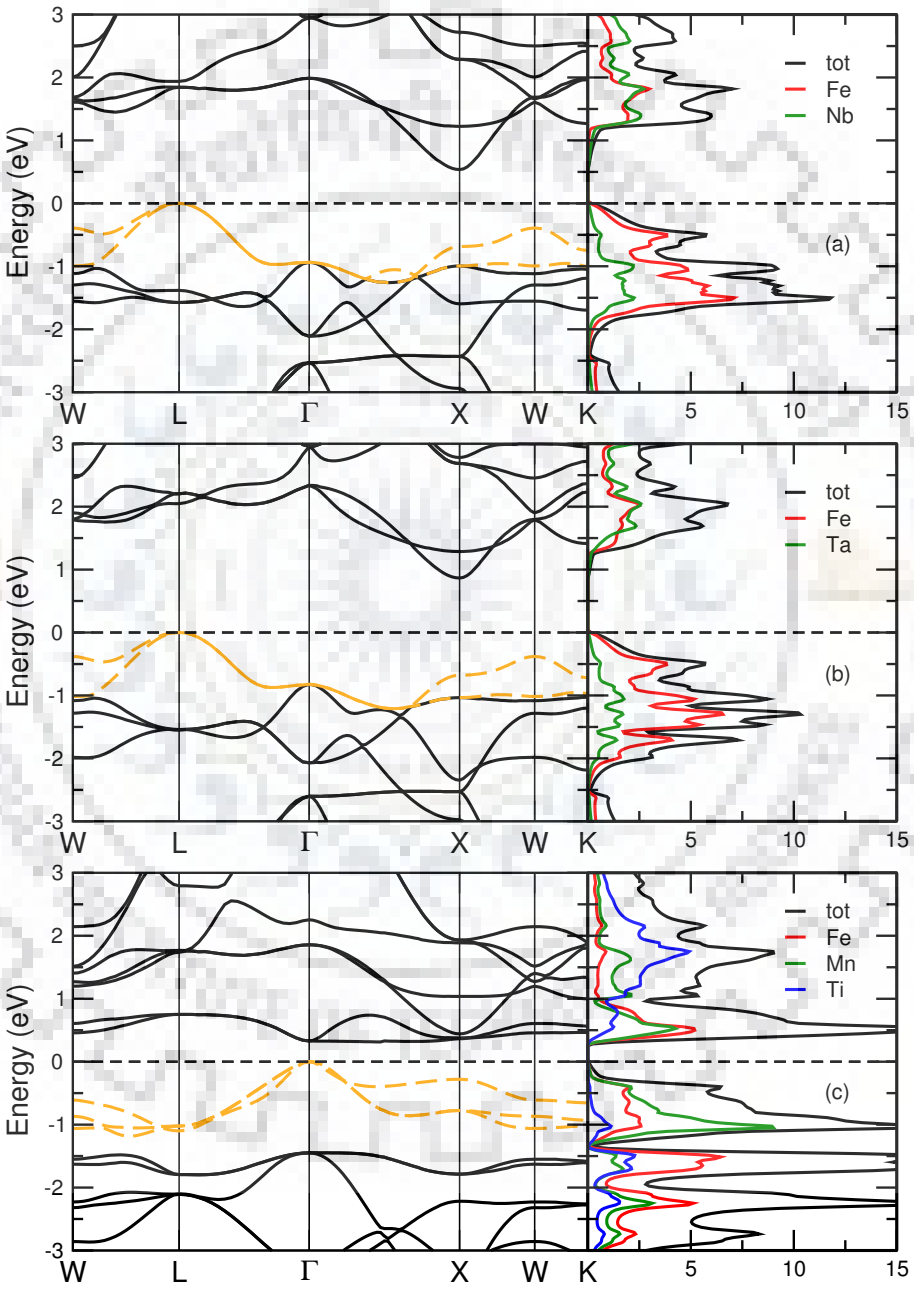

Figure 4.3: Calculated electronic structures of (a) FeNbSb, (b) FeTaSb, and (c) FeMnTiSb, in cubic $F\bar{4}3m$ symmetry. The top of the valence band is taken as zero on the energy axis.

4.2.2 Thermoelectric Parameters

The TE properties of all the systems were calculated using rigid band approximation (RBA), semiclassical Boltzmann theory, and constant relaxation time approach. In this section, the trend of PF with doping for FeNbSb is predicted and further compared with experimentally reported ones. Then, the TE properties of FeTaSb and FeMnTiSb are discussed. The three representative temperatures namely 300 K, 700 K, and 1100 K are chosen for the evaluation of TE properties. The purpose is to see whether the material is compatible with room temperature or conventional high-temperature TE applications or for both. For convenience, throughout this chapter, *p*-FeNbSb, *p*-FeTaSb, *p*-FeMnTiSb for *p*-type doped systems, and *n*-FeMnTiSb for *n*-type doped system are used.

The calculated PF/τ as a function of doping (per unit cell), e/uc, at different temperatures for FeNbSb is shown in Fig. 4.4(a). The trend of PF/τ is increasing for both *n*-type and *p*-type doping and then fall gradually at higher doping levels. The behavior was consistent at all considered temperatures. But the maximum PF/τ was achieved for *p*-type doping at all the temperatures. This is in good agreement with previously calculated and experimental results [45, 46, 156, 96, 162]. The optimal *p*-type doping levels for maximum PF/τ are 0.04, 0.12, and 0.20 e/uc, at 300 K, 700 K, and 1100 K, respectively. Yang *et al.* also proposed 0.04 as the optimal *p*-type doping level for FeNbSb at room temperature [152]. Further, the maximum PF/τ at 1100 K for 0.2 *p*-type doping is in good agreement with experimental results. Fu *et al.* reported a peak ZT of 1.1 at 1100 K for $FeNb_{0.8}Ti_{0.2}Sb$, i.e., 0.2 *p*-type doping [49].

A comparison of calculated and experimental PF of *p*-FeNbSb is shown in Fig. 4.4(b). To compare the theory with experiment, an approximate value of relaxation time was used, i.e., τ = 2 x 10^{-15} s, arrived at by comparing the calculated and experimental electrical conductivity of *p*-FeNbSb. Using $\tau = \sigma_{exp}/\sigma_{cal}$ suggested that τ is of the order of 10^{-15} s. The strategy had been helpful in the previous chapter and a reasonable agreement was obtained for cobalt-based 18-VEC systems [158]. Thus, the adopted value of relaxation time is a realistic representative value. Moreover, the constant relaxation time approach has been successfully used by many groups in predicting the transport properties [99, 96]. The trend of calculated PF is quite similar to that of the experimental PF for *p*-FeNbSb. The difference in magnitude is expected since the calculations were for the pristine system under ideal conditions, very unlikely to be the case for experimental study. The magnitude may vary more or less depending on the system under consideration and techniques employed. However, the trend of the two curves is more important to predict the properties of materials.

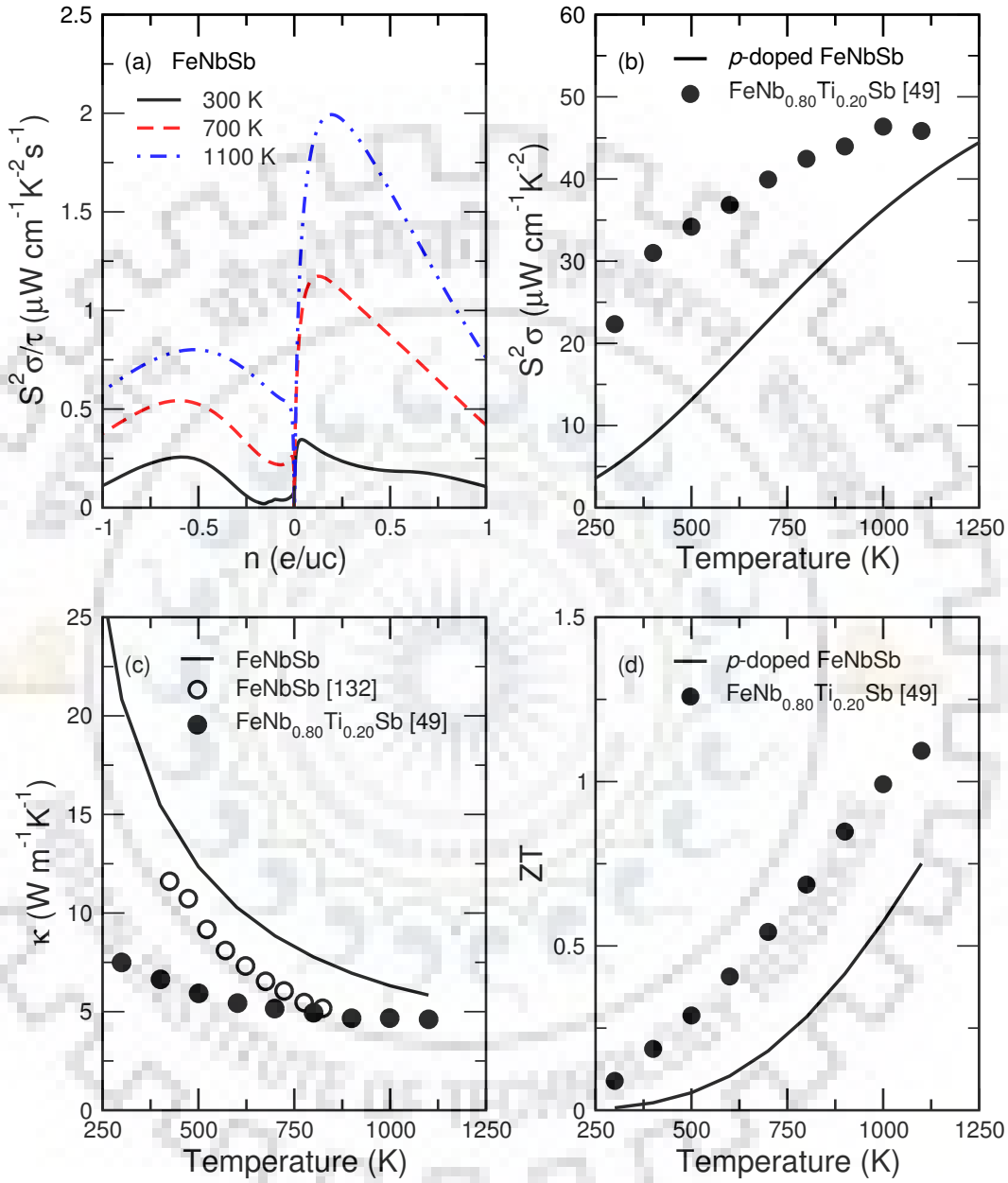

Figure 4.4: (a) Calculated $S^2\sigma/\tau$ as a function of doping (per unit cell) for FeNbSb at 300 K, 700 K, and 1100 K. The negative and positive values on horizontal axis represent electron and hole doping, respectively. (b) Calculated and reported $S^2\sigma$ as a function of temperature for 0.2 *p*-type doped FeNbSb (c) Thermal conductivity versus temperature for calculated FeNbSb, reported FeNbSb (empty circles), and reported 0.2 *p*-type doped FeNbSb (filled circles) (d) The figure of merit as a function of temperature for calculated and reported 0.2 *p*-type doped FeNbSb.

Figure 4.4(c) shows calculated thermal conductivity as a function of temperature for base composition FeNbSb, along with reported data on FeNbSb and p-FeNbSb. The dominance of κ_l in total thermal conductivity is well known for Heusler alloys [63, 144, 85]. The plots for calculated and reported κ are in good agreement for the parent material FeNbSb in the range of 400-825 K [132]. The calculated values slightly overestimated the reported ones. Hence, one needs to keep in mind that the calculations would yield an underestimated value of the figure of merit. The experimental data shows that the κ of reported p-FeNbSb has lower values than that of parent FeNbSb as expected on account of mass fluctuations. Similar to PF, the calculated κ for FeNbSb approaches the κ of reported p-FeNbSb at the higher temperature. Note that the calculated values of κ were lowered by tenfold. This was the observation from the previous chapter that the calculated values of κ_l for ternary hH alloys were tenfold higher [159].

The behavior of figure of merit ZT as a function of temperature for calculated and reported p-FeNbSb, illustrated in Fig. 4.4(d), exhibited similar trend over the entire temperature range [49]. However, the calculated values lagged behind the experimental ones. It is noteworthy here that the difference in the magnitude of the two can be attributed to the fact that the κ of undoped FeNbSb was employed for calculating the ZT of p-FeNbSb. As can be seen from Fig. 4.4(c), (i) the calculations overestimated κ w.r.t. the experiment, (ii) a significant reduction in κ was observed with doping. Consequently, the calculated ZT values are expected to be much lower than the actual ones. The calculations of κ for doped systems are relatively complicated and computationally demanding, therefore, κ of undoped FeNbSb was adopted for the doped material also. Nevertheless, similar trends were obtained for calculated and reported TE properties of p-FeNbSb. As stated earlier, the trend is more important rather than the actual figures. Moreover, the close proximity of the calculated and reported plots for PF and κ at higher temperatures imply that the calculated results are comparable to reported ones in that range. Having judged the results for the reference material FeNbSb, the following are presented the findings on the two proposed TE systems FeTaSb and FeMnTiSb.

The dependence of TE parameters on doping at different temperatures for FeTaSb and FeMnTiSb is illustrated in Fig. 4.5. The Seebeck coefficient, Fig. 4.5(a) and 4.5(d), is maximum, for both the materials, when the Fermi level is near the middle of the band gap and decreased at higher doping levels, showing almost the same trend for all the temperatures under consideration. Exactly an opposite trend was observed for electrical conductivity which increased rapidly with doping, Fig. 4.5 (b) and 4.5(e). As discussed under electronic features, the Seebeck coefficient of FeMnTiSb was higher than that of Fe-

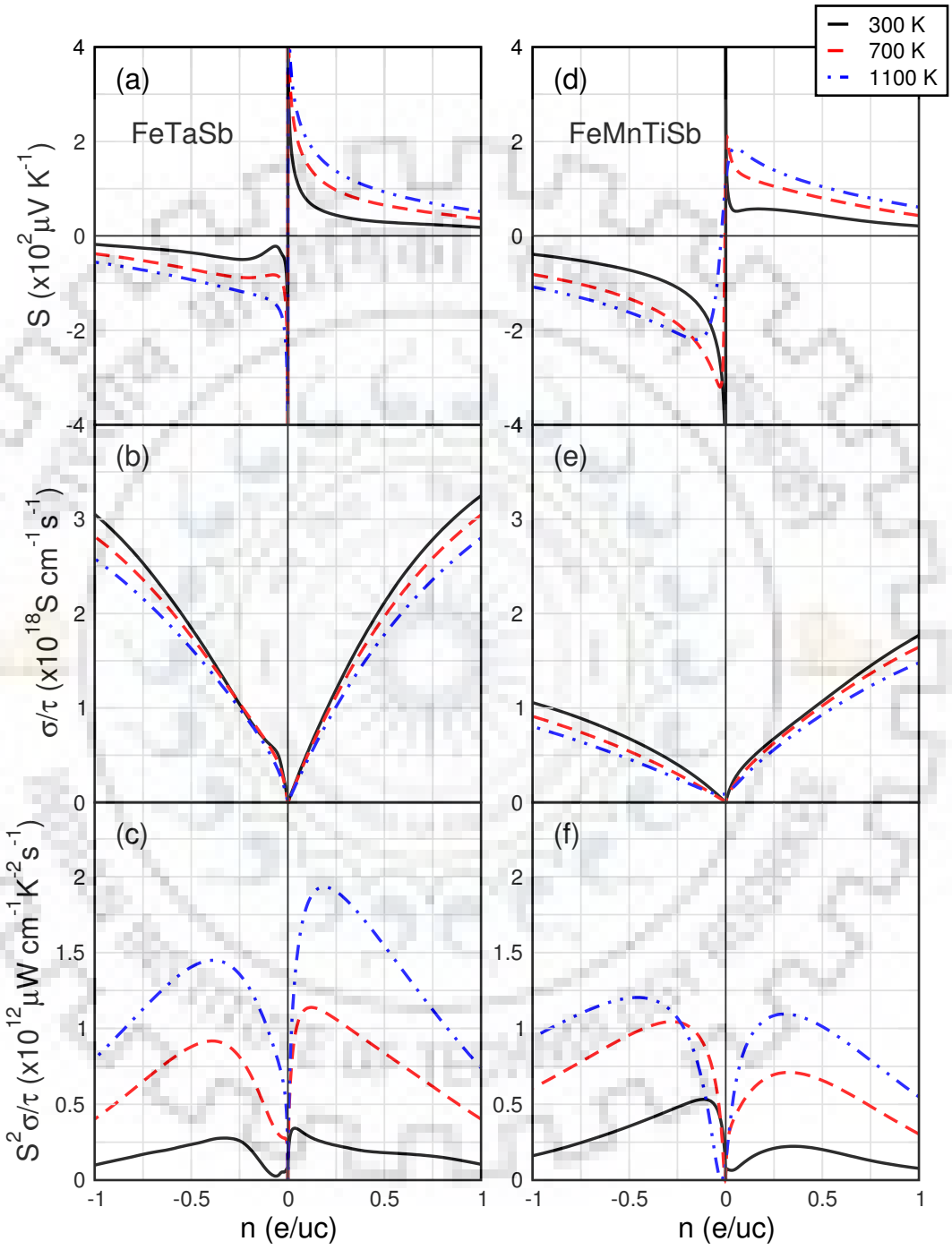

Figure 4.5: The trend of Seebeck coefficient, electrical conductivity, and power factor as a function of doping per unit cell at 300 K, 700 K, and 1100 K, for FeTaSb (a-c) and FeMnTiSb (d-f). The negative and positive values on horizontal axes represent electron and hole doping, respectively. Power factor and electrical conductivity are plotted with respect to relaxation time.

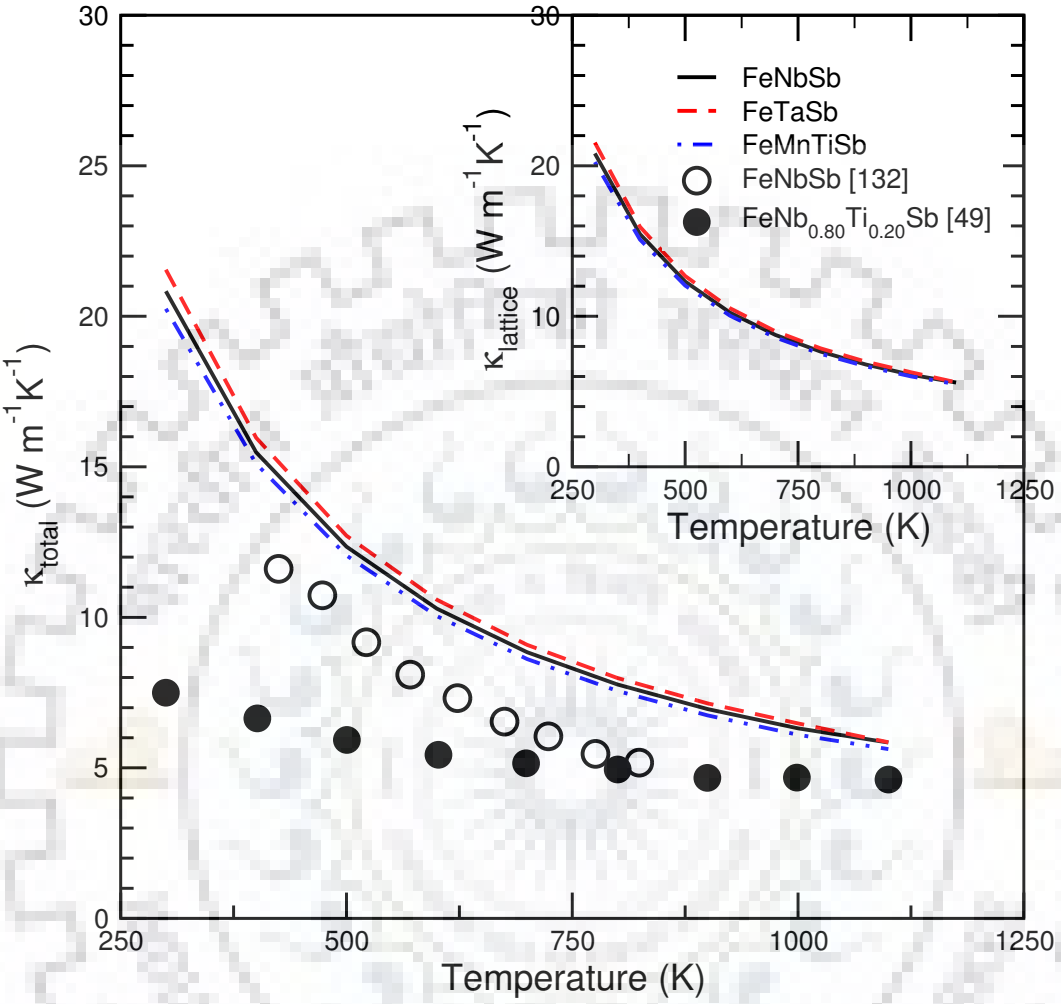

Figure 4.6: The calculated total thermal conductivity of FeNbSb, FeTaSb, FeMnTiSb, and reported total thermal conductivity of FeNbSb and 0.2 p-type doped FeNbSb. The inset shows the lattice thermal conductivity of FeNbSb, FeTaSb, and FeMnTiSb.

TaSb whereas the electrical conductivity of FeMnTiSb was lower than that of FeTaSb owing to heavy flat bands at VBM. As the Fermi level shifts towards the VBM or CBM, the carrier concentration increases, thereby improving the electrical conductivity and reducing the Seebeck coefficient. Therefore, an optimal doping level is desired which maintains a balance between Seebeck coefficient and electrical conductivity to attain a maximum PF. Generally, such a doping level is found when the Fermi level is near the band edge [149, 95, 109, 152].

The calculated PF/τ as a function of doping (per unit cell) at different temperatures for FeTaSb and FeMnTiSb is shown in Fig. 4.5(c) and 4.5(f). The magnitude of PF/τ enhanced with doping, and exhibited quite a similar behavior for both the systems: first increased sharply with doping and then dropped steadily at higher doping levels. The

p-type doping dominated n-type at all the temperatures for FeTaSb. The optimal p-type doping levels for best PF/τ values were 0.03, 0.11, and 0.18 e/uc, at 300 K, 700 K, and 1100 K, respectively. However, the n-type doping prevailed in case of FeMnTiSb at different temperatures. The maximum PF/τ values were obtained at 0.11, 0.27, and 0.47 e/uc n-type doping at 300 K, 700 K, and 1100 K, respectively. The doping levels are quite pragmatic and could be realized experimentally. The hole doped FeNbSb has recently been reported to have the highest ZT among the hH alloys [156]. It was encouraging to note that the PF/τ for the proposed material p-FeTaSb at 1100 K was comparable to that of p-FeNbSb. This shows the potential of FeTaSb as a high-temperature TE material.

Now, the attention is focussed on the quaternary alloy FeMnTiSb being explored for TE properties. It is highly desirable to have both n-type and p-type branches of a TE module to be of similar TE materials or ideally of the same material. Efficient combination of n-type and p-type branches of the same material is rare. In most of the cases, the performance of one type is poor in comparison to the other [37]. Interestingly, at 1100 K, the values of maximum PF/τ for n-type and p-type doped FeMnTiSb are very close; the corresponding optimal doping levels are 0.47 and 0.31 e/uc, respectively. This shows the importance of FeMnTiSb as both n-type and p-type high-temperature TE material.

Another noteworthy observation from Fig. 4.5(f) is that the maximum calculated PF/τ at 300 K of FeMnTiSb is about 1.5 times that of recently much popular or acclaimed FeNbSb. Thus, FeMnTiSb could be a better room temperature TE prospect in comparison to FeNbSb and FeTaSb. High PF/τ values for both n-type and p-type FeTaSb at 1100 K (Fig. 4.5(c)) reveals that FeTaSb may also fall in the category of materials which can be utilized for making both n-type and p-type branches. The discussion so far indicates that the PF of p-FeTaSb is comparable with p-FeNbSb whereas n-FeMnTiSb could be a better room temperature TE prospect. Therefore, it becomes interesting to see the behavior of their thermal conductivity.

Figure 4.6 shows the trend of calculated κ with temperature for FeNbSb, FeTaSb, and FeMnTiSb. For comparison, reported κ of parent FeNbSb and p-FeNbSb are also included. The inset establishes the dominance of κ_l in total κ. As discussed earlier, the trend of calculated and reported κ of parent FeNbSb is quite similar. However, the calculated values slightly overestimate the reported ones. The effect of doping is quite pronounced on the κ of p-FeNbSb. Importantly, the two curves for reported p-doped and calculated undoped FeNbSb approaches each other at the higher temperature. Despite the low projected values, the κ of FeTaSb and FeMnTiSb bears a close resemblance to that of FeNbSb over the entire temperature range. As stated earlier, the κ of quaternary FeMnTiSb was

System	T	n	c	S	PF	ZT
FeNbSb	300	0.04	0.7	127	5.1	0.007
	700	0.12	2.4	139	22.7	0.179
	1100	0.20	3.7	155	39.8	0.749
FeNbSb (exp.) [49]	1100	0.20		203	45.8	1.1
FeTaSb	300	0.03	0.7	131	6.8	0.009
	700	0.11	2.3	140	22.6	0.174
	1100	0.18	3.6	156	38.6	0.725
FeMnTiSb	300	-0.11	2.0	162	10.6	0.030
	700	-0.27	5.0	180	20.4	0.169
	1100	-0.47	8.8	166	24.0	0.469

Table 4.2: The calculated optimal doping levels (n, per unit cell) for p-type FeNbSb, p-type FeTaSb, and n-type FeMnTiSb are shown at different temperatures (T, in K) and the corresponding carrier concentration (c, in 10^{21} cm^{-3}), Seebeck coefficient (S, in μV K^{-1}), power factor (PF, in μW cm^{-1} K^{-2}), and ZT. The reported values of FeNbSb at 1100 K are also listed for comparison.

expected to be lower than that of ternary hH alloys, however, the reduction in κ was not substantial.

For a quantitative analysis, Table 4.2 presents the optimal doping levels and the corresponding Seebeck coefficient, PF, and ZT for FeTaSb and FeMnTiSb, *vis-a-vis* those of the reference material FeNbSb from experiments and the calculations. The values of Seebeck coefficient were in between 127-186 μV K^{-1} and are in line with many high-performance hH alloys. The optimal doping concentrations were of the order of 10^{21} cm^{-3} which are most suitable for obtaining a high TE performance by hH alloy.

As discussed earlier, assuming a relaxation time τ = 2 x 10^{-15} s, approximate values of PF and ZT for FeTaSb and FeMnTiSb at optimal doping concentrations are proposed. The calculated and reported PF for p-FeNbSb [49], at 1100 K, are 39.8 μW cm^{-1} K^{-2} and 45.8 μW cm^{-1} K^{-2}, respectively. Thus, the good agreement between the calculated and experimental values indicates the reliability of the calculations and the suitability of the chosen relaxation time, especially at high-temperatures. At 1100 K, the calculated PF of p-FeTaSb was 38 μW cm^{-1} K^{-2} which is again comparable to calculated and reported PF of p-FeNbSb. Whereas FeTaSb could be as challenging as FeNbSb at high-temperatures, the PF of n-FeMnTiSb at 1100 K is still comparable with conventional TE material CoTiSb,

reported [145, 116] to have the maximum PF of about 23.2 μW cm^{-1} K^{-2}. The most remarkable observation from Table 4.2 is that the n-FeMnTiSb showed a high PF of 10.6 μW cm^{-1} K^{-2} at room temperature which is higher than that of FeNbSb. Despite being a low value, this PF is still competitive enough with that of many CoTiSb based materials [145, 116].

Incorporating κ of parent systems, displayed in Fig. 4.6, in the ZT formula for p-FeNbSb, p-FeTaSb, and n-FeMnTiSb, the obtained underestimated, as discussed earlier, ZT values are listed in Table 4.2. The calculated and reported ZT values at 1100 K for p-FeNbSb are 0.74 and 1.1, respectively. Remarkably, the figure of merit $ZT \sim 0.72$ for p-FeTaSb at 1100 K, is not far behind from that of p-FeNbSb, thus ensuring that p-FeTaSb is as promising as p-doped FeNbSb. It is worth stressing here that, as discussed earlier, the actual values of the figure of merit could be as high as unity for both p-FeNbSb and p-FeTaSb provided κ of doped FeNbSb and FeTaSb is included in the ZT formula.

The calculated ZT of n-FeMnTiSb at room temperature was quite low. The reason is quite obvious. The κ of undoped FeMnTiSb was fairly high at room temperature (Fig. 4.6). Since the κ of FeMnTiSb parallels κ of FeNbSb, it is expected that the doped FeMnTiSb would have about threefold lower κ at room temperature, thereby improving the overall figure of merit. Nevertheless, the calculated ZT values of p-FeMnTiSb and n-FeMnTiSb, at 1100 K, were 0.42 and 0.46 (not shown in Table), respectively. The values were lower than that of FeNbSb but compatible enough with CoTiSb based materials [145, 116]. Similar to FeNbSb and FeTaSb, the actual ZT values of n-FeMnTiSb and p-FeMnTiSb are expected to be higher on the inclusion of κ of doped FeMnTiSb in the figure of merit formula.

4.3 Conclusions

In this chapter, utilizing *ab initio* approach, semiclassical Boltzmann transport theory, and constant relaxation time approach, the ground state properties, structural stability, electronic features (band structure and DOS), and thermal and electrical transport properties of two novel Fe-based Heusler alloys FeTaSb and FeMnTiSb were systematically investigated. Both the systems were nonmagnetic semiconductors in cubic $F\bar{4}3m$ symmetry and their stability was confirmed by phonon calculations. At 1100 K, the power factor of p-doped FeTaSb (38.6 μW cm^{-1} K^{-2}) was comparable to the best performing Heusler alloy FeNbSb whereas the power factor of n-doped FeMnTiSb (24 μW cm^{-1} K^{-2}) was comparable to the conventional TE material CoTiSb. However, the power factor of FeMnTiSb (10.6 μW

cm^{-1} K^{-2}) at room temperature was higher than both FeNbSb and FeTaSb. Interestingly, at high-temperatures, the low-cost FeMnTiSb could be used as both n-type and p-type legs in a TE module. The ZT at 1100 K of p-doped FeTaSb was 0.72 whereas ZT of n-doped and p-doped FeMnTiSb were 0.46 and 0.42, respectively, which, as discussed, are actually underestimated values. The findings are optimistic, suggesting the potential of FeTaSb and FeMnTiSb as promising TE materials, would motivate and prompt the experimentalists to realize these materials and their potential.

Chapter 5

Polytypism and Thermoelectric Properties in Nowotny-Juza Phases

This chapter discusses the polytypism behavior in LiZnX (X = N, P, As, Sb, and Bi) family, the role of chemical and hydrostatic pressure in controlling such behavior, and the effect of polytypism on thermoelectric (TE) properties. Further, the effect of doping is considered in systems to tune the desired TE properties.

5.1 Introduction

Nowotny-Juza phases are a special derivative of half-Heusler (hH) alloys when X belongs to the Group-I, Y to the Group-II, and Z to the pnictogen family [143]. The crystal structure of Nowotny-Juza phases, $A^{I}B^{II}C^{V}$, comprises a hypothetical zinc-blende type lattice of $[BC]^{-}$ interpenetrated by a face-centered lattice of A^{+} [94, 91, 93, 92, 89, 90]. The zinc-blende type covalent framework offers the high mobility of charge carries whereas the filled octahedral sites (A^{+}) provides ionicity to the system, thereby reducing the thermal conductivity. The filled octahedral sites may also be helpful in scattering the phonons by acting as rattlers [86]. This proffers that Nowotny-Juza phases could be promising candidates for TE applications.

Within the Nowotny-Juza phases, the LiZnX (X = N, P, As, Sb, and Bi) family has drawn considerable interest owing to their potential applications in neutron detectors [105], photovoltaic cells [3], and Li-ion batteries [5]. For many years, this class of filled tetrahedral semiconductors was not explored in the context of thermoelectricity. In 2006, with the help of rigid band approach and semiclassic Boltzmann theory, Madsen investigated a large number of compounds and predicted LiZnSb as a new potential TE material, with

an estimated $ZT\sim2$ at 600 K for lightly doped n-type LiZnSb [99].

Since then, the Nowotny-Juza phases have witnessed a surge in the field of thermoelectricity. In response to Madsen's theoretical calculations, Toberer experimentally reported a $ZT < 1$ at 523 K of p-doped LiZnSb [135]. In a recent work, the transport properties of Li-based Nowotny-Juza alloys were studied by a first-principles approach [149]. Most recently, the previously unknown polytypism was reported for the first time in this class. The solution phase method reveals the cubic ($F\bar{4}3m$) analogue of LiZnSb despite the hexagonal ($P6_3mc$) structure reported by traditional solid-state synthesis [141]. However, the solution phase attempt on LiZnP resulted in the cubic structure in accordance with the solid-state techniques [142]. Thus, merely varying the synthesis technique is not solely responsible for the polytypism in Nowotny-Juza phases.

The polytypism behavior is not limited to Nowotny-Juza phases. The first investigations on polytypism were performed on SiC in 1912. Since then, the polytypism has been reported in a large number of systems. The phenomenon is governed by a number of parameters but greatly influenced by temperature and pressure. The cubic sphalerite and hexagonal wurtzite are two well-known examples of polytypism in ZnS. A number of perovskite-related structures are reported to be polytypic under high pressure [138].

With regard to polytypism in Nowotny-Juza phases, few questions need to be addressed. What is the driving force of polytypism in LiZnSb? Is it achievable by varying the synthesis techniques only? Or the transformation is pressure driven? Is it restricted to $F\bar{4}3m$ and $P6_3mc$ or also possible in closely related $P6_3/mmc$ symmetry? Will transport properties be affected by the phase transition? And most importantly, is it limited only to LiZnSb or also possible for other members of LiZnX family? To answer these fundamental questions, the LiZnX systems are revisited in this chapter.

The first three members of LiZnX (X = N, P, As, Sb, and Bi) family crystallize in cubic ($F\bar{4}3m$) [94, 91, 93] whereas the latter two are reported in hexagonal symmetry ($P6_3mc$) [135, 134]. On descending from N to Bi in the family, the symmetry changes from cubic to hexagonal at LiZnSb. The polytypism is also exhibited by LiZnSb. It is quite possible that the onset of polytypism in LiZnX family begins at LiZnSb and likely to prevail in succeeding LiZnBi also. By the same analogy, moving up from Bi to N, the symmetry changes from hexagonal to cubic at LiZnAs. The polytypism may also be exhibited by LiZnAs. Stating that LiZnAs and LiZnBi are very likely to show different phases, the polytypism in other family members cannot be ruled out completely. Now, what could be the driving force for such phase transition?

As one move from N to Bi in LiZnX family, the increase in the size of pnictogen

atoms leads to the expansion of crystal lattice. The relative expansion of the crystal volume corresponds to the negative internal pressure. Since the phase transition appears towards the bottom of the LiZnX series, i.e., LiZnSb, the role of internal pressure in polytypism cannot be overlooked. Thus, along with controlling the synthesis conditions, the internal pressure seems to be a governing factor in the phase transition. A number of studies have noted a profound effect of internal pressure in controlling the phase transitions [76, 72, 44]. As well as, the hydrostatic pressure is well-known to govern the phase transition in a number of compounds [8, 16, 78]. However, there is no previous evidence of hydrostatic pressure driven polytypism in Nowotny-Juza phases. It can be stressed that the hydrostatic pressure may also act as the driving force of polytypism in Nowotony-Juza phases. To further gain an insight into the polytypism, next, the structural optimization of LiZnX systems is discussed in cubic and hexagonal symmetry.

5.2 Structural Optimization

The ground state properties of LiZnX systems were calculated using the GGA implemented in Wien2k. Fitted with Birch-Murnaghan equation [9], the total energy was minimized as a function of volume for $F\bar{4}3m$, as a function of c/a and volume for $P6_3/mmc$, and as a function of c/a, volume, and forces for $P6_3mc$ symmetry. The crystal structure in all three symmetries is discussed in detail and can be seen in Chapter-1. Table 5.1 lists the calculated cell parameters and band gap values of LiZnX systems in different symmetries. The optimized free atomic position along the z-axis, in $P6_3mc$ structure, increased from 0.73 to 0.84 in case of Zn whereas the position of X changed from 0.09 to 0.23 on going from LiZnN to LiZnBi. Overall, the distance between Zn and X remained almost constant.

The calculated cell parameters of LiZnN, LiZnP, LiZnAs in $F\bar{4}3m$ and LiZnSb, LiZnBi in $P6_3mc$ symmetry are in good agreement with reported values. The calculated cell parameters by Wien2k exceeded the solid-state synthesis reported values by 0-0.78%, except for recently reported low-temperature solution phase cubic LiZnSb (2.8%). The unit cell volume, as expected, expanded in all the systems in different symmetries with increasing atomic size of X element. Besides, the calculated c/a ratio of all but LiZnN in $P6_3mc$ symmetry was close to the ideal value of 1.633. However, the c/a ratio ranges from 1.24 to 1.99 in $P6_3/mmc$ structure. As the symmetry changed from planar $P6_3/mmc$ to puckered $P6_3mc$, excluding LiZnBi, the c/a ratio decreased accordingly. Thus, the introduction of buckling in planar honeycomb lattice resulted in lowering the c/a ratio.

	$F\bar{4}3m$			$P6_3/mmc$				$P6_3mc$			
System	a (Å)	E_g (eV)	B (GPa)	a (Å)	c/a	E_g (eV)	B (GPa)	a (Å)	c/a	E_g (eV)	B (GPa)
LiZnN	4.92	0.53	113.79	3.39	1.99	0.40	50.80	3.40	1.75	0.32	106.41
	(4.90[a]	(1.98)[a]	-	-	-	-	-	-	-	-	-
LiZnP	5.76	1.35	64.50	4.01	1.81	1.30	31.42	4.03	1.62	1.19	57.41
	(5.76)[b]	(2.04)[b]	-	-	-	-	-	-	-	-	-
LiZnAs	5.97	0.46	55.87	4.16	1.78	0.57	26.56	4.18	1.62	0.39	55.02
	(5.94)[c]	(1.1)[c]	-	-		-	-	-	-	-	-
LiZnSb	6.41	0.54	42.46	4.47	1.74	0.20	19.99	4.46	1.62	0.37	46.54
	(6.23)[d]	-	-	-	-	-	-	(4.42)[e]	(1.61)	-	-
LiZnBi	6.61	0.00	35.52	4.95	1.24	0.00	41.38	4.60	1.62	-	38.88
	-	-	-	-	-	-	-	(4.57)[f]	(1.61)	-	-

Table 5.1: Wien2k calculated cell parameters a and c, band gap E_g, and bulk modulus B, of LiZnX (X = N, P, As, Sb, and Bi) systems in $F\bar{4}3m$, $P6_3/mmc$, and $P6_3mc$ symmetry. The experimentally reported values are listed in parentheses. [a]Ref. [94], [b]Ref. [91], [c]Ref. [93], [d]Ref. [141], [e]Ref. [135], [f]Ref. [134].

The deviation of c/a ratio from ideal value in $P6_3/mmc$ symmetry invalidates the possibility of the existence of LiZnX family in hexagonal planar structure. Similarly, the existence of LiZnN in polar $P6_3mc$ structure is uncertain. Importantly, the ideal c/a ratio was preserved in LiZnP and LiZnAs in $P6_3mc$ structure, indicating the possible stability of two systems in the hexagonal variant. Thus, LiZnP and LiZnAs may show polytypism among the LiZnX family which is one of the focus of the chapter. Further, to study the effect of polytypism on transport properties, it is important to see how the band gap varies in different symmetries. Let us now look at the second part of Table 5.1, where shown the trend of band gap values in different symmetries.

As GGA is known to underestimate the band gap, the calculated values were lower than the experimental ones. However, the values are consistent with previously calculated values [82]. The band gap ranges 0.20-1.35 eV, tailor-made for TE materials. Notably, among the LiZnX systems, LiZnP possesses the highest band gap in all three symmetries. The band gap in case of cubic LiZnSb was slightly higher than the expectations. Ignoring this, the band gap of LiZnX systems in all three symmetries decreased from LiZnP to LiZnBi with increasing atomic size of X. The smaller band gap of LiZnN in comparison to LiZnP has been assessed in detail by Kalarasse and Bennecer and was attributed to the strong p-d repulsion in LiZnN. The repulsion leads to an upward shift of valence band maximum in energy [83].

Interestingly, except for LiZnBi, the band gap survived on going from cubic to hexagonal or hexagonal to cubic symmetry. Provided semiconductors are the best choices for TE materials, the LiZnX systems in different geometries could be interesting TE prospectives. The predicted stability of LiZnP and LiZnAs in hexagonal structure and the survival of band gap in different symmetries collectively motivated to see whether the polytypism behavior in LiZnX family was possible or not. Hence, it became increasingly important to see the energy profile in order to affirm the so far proffered polytypism in LiZnX family. And most significantly, what could be the realistic volume and pressure requirements for such behavior.

Figure 5.1 details the optimization of LiZnX systems in $F\bar{4}3m$ and $P6_3mc$ symmetry. Initially, the possible existence of LiZnX systems in $F\bar{4}3m$, $P6_3/mmc$, and $P6_3mc$ symmetry was purported. However, as stated before, the deviations in c/a ratio from ideal value in $P6_3/mmc$ symmetry indicated their instability in hexagonal planar structure. Furthermore, the calculations revealed that the energy difference between $P6_3/mmc$ and other symmetries was quite high to achieve under ambient conditions (Table 5.2). Therefore, any possibility of the existence of LiZnX systems in $P6_3/mmc$ symmetry was ruled out and

$F\bar{4}3m$ and $P6_3mc$ structures were considered in the quest of polytypism.

It is interesting to note that all LiZnX systems were found to be stable in the cubic ground state (Fig. 5.1). The calculated low energy cubic phases of LiZnN, LiZnP, and LiZnAs are consistent with reported structures [94, 91, 93]. However, the calculated cubic ground state of LiZnSb and LiZnBi is in contrast to solid-state synthesis reported hexagonal structures ($P6_3mc$) [135, 134]. More recently, LiZnSb was synthesized in cubic phase by low-temperature solution phase method [141]. The same group also showed that the cubic phase is more energetically favorable through first-principles calculations. Here, an important question arises: Why thermodynamically less stable hexagonal LiZnSb phase was reported for so long despite the recently synthesized more stable cubic LiZnSb?

In order to understand this, the energy profile of LiZnX systems in both $F\bar{4}3m$ and $P6_3mc$ symmetries was analyzed. Figure 5.1, barring LiZnAs, contend the decreasing energy gap between the two phases ($F\bar{4}3m$ and $P6_3mc$) on descending from LiZnN to LiZnBi. The exact values are listed in Table 5.2. The LiZnAs system had a somewhat higher energy gap between the two symmetries than the preceding LiZnP. The decreasing energy gap between $F\bar{4}3m$ and $P6_3mc$ symmetry can be attributed to the volume expansion of unit cell on going from LiZnN to LiZnBi. The energy gap between cubic and hexagonal symmetry in LiZnN was 0.48 eV, in LiZnP was 0.30 eV, whereas in case of LiZnAs was 0.77 eV.

However, remarkably, the energy gap between the two symmetries came down to 0.05 eV for LiZnSb and further down to 0.01 eV in case of LiZnBi. Considering the thermal energy at room temperature is 0.025 eV, a small amount of activation energy by temperature or pressure could interchangeably result in either cubic or hexagonal LiZnSb. This could be the plausible rationale for the synthesis of cubic LiZnSb by low-temperature solution phase method and hexagonal variant by the high-temperature solid-state technique. However, as mentioned by White, the thermodynamically less stable hexagonal phase formation by high-temperature solid-state technique is surprising [141].

Nevertheless, in the same line of argument, the even lower energy gap of 0.01 eV between the cubic and hexagonal analogue and the calculated low energy cubic phase of LiZnBi suggests the possible existence of previously known hexagonal LiZnBi in cubic phase. The experimental support of cubic LiZnSb further substantiates the predicted result. Keeping in mind the recent success in cubic LiZnSb, it is strongly believed that the cubic analogue of LiZnBi could be synthesized by the low-temperature solution phase method. Having attributed that LiZnSb and LiZnBi are most likely to exist in cubic phase complementing the previously reported hexagonal phase, the other way round possibility was further investigated, i.e., the existence of previously known cubic phases in the hexagonal

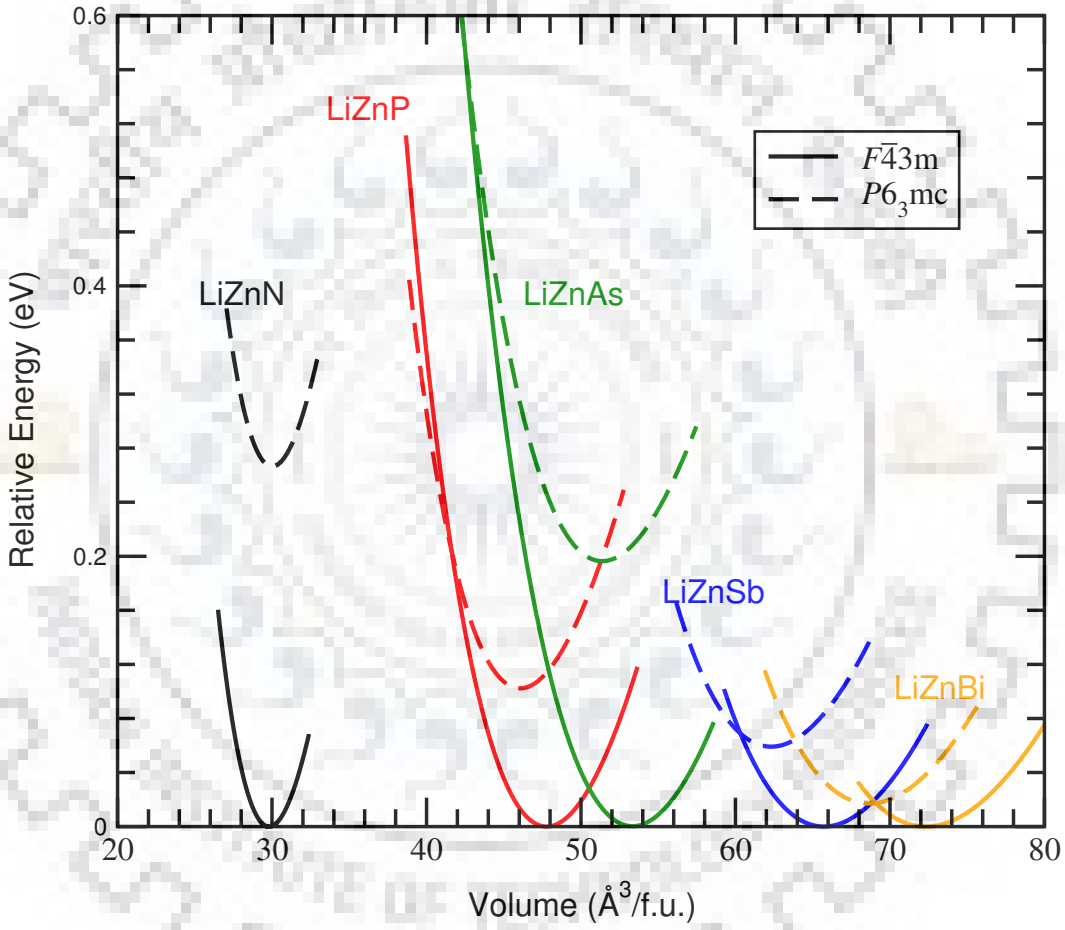

Figure 5.1: Calculated relative energy of LiZnX (X = N, P, As, Sb, and Bi) systems as a function of volume per formula unit in cubic $F\bar{4}3m$ and hexagonal $P6_3mc$ symmetry. The solid and dashed lines represent cubic and hexagonal symmetry, respectively.

System	$E_{F\bar{4}3m}$	$E_{P6_3/mmc}$	E_{P6_3mc}	ΔE	P
LiZnN	0	0.48	0.26	-	-
LiZnP	0	0.30	0.10	0.20	12.3
LiZnAs	0	0.77	0.19	0.56	20.3
LiZnSb	0	1.10	0.05	0.06	4.3
LiZnBi	0	0.68	0.01	0.01	1.7

Table 5.2: Calculated relative energy, E (in eV) of LiZnX systems in $F\bar{4}3m$, $P6_3/mmc$, and $P6_3mc$ symmetry. The cubic ground state minimum is set at 0. ΔE (in eV) and P (in GPa) represents the energy and pressure required for the phase transition from cubic to hexagonal symmetry.

phases.

Can hexagonal analogues of previously reported cubic LiZnN, LiZnP, and LiZnAs be synthesized by low-temperature solution phase method? Contrary to the expectations, the solution phase synthesis of LiZnP by White et al. also resulted in the cubic structure [142]. Therefore, merely varying the synthesis technique may not result into polytypism. Once again, the plausible reasoning stems from the energy profile of LiZnP. The energy gap of 0.10 eV between the cubic and hexagonal phase might be responsible for the non-existence of LiZnP in hexagonal symmetry. The energy barrier was even higher for LiZnN (0.26 eV) and LiZnAs (0.19 eV). Thus, further experimental investigations are needed in order to overcome the energy barrier between the cubic and hexagonal symmetry.

Few potential approaches utilized over the years involves the application of high-temperature, high pressure or combination of both to achieve the transition between different symmetries. In this endeavor, the possibility of transition between the well established cubic and proposed hexagonal phase of LiZnN, LiZnP, and LiZnAs is explored. Further, the cubic to hexagonal transition in LiZnSb and LiZnBi is also investigated. With no possible transition in LiZnN, the LiZnP was marked by a cubic to hexagonal transition at 0.20 eV whereas the required energy for the transition in LiZnAs was 0.56 eV (Fig. 5.1). Obviously, this may not be achieved under ambient conditions but could be driven by high-temperature or high pressure. Since the calculations were performed at 0 K, the required pressure for cubic to hexagonal transition in LiZnP and LiZnAs was calculated to be 12.3 and 20.3 GPa, respectively. In case of LiZnSb and LiZnBi, the required pressure was 4.3 and 1.7 GPa, respectively, corresponding to the 0.06 and 0.01 eV energy requirement. On the application of the required amount of pressure, one could achieve the hexagonal analogues of these

systems. However, due care must be exercised while performing pressure experiments since the bulk modulus indicates the highly compressible nature of LiZnX systems (Table 5.1).

As an insight to experimental realization, further, the variation of cell parameter, c/a ratio, and unit cell volume on pressure application was analyzed. The variation of lattice parameter and c/a as a function of pressure is illustrated in Fig. 5.2. The lattice parameter a of all the systems decreased steadily in both cubic and hexagonal structures. The decrement of lattice parameter in cubic phase was about 0.02 Å/GPa in LiZnP and LiZnAs, which grown to 0.04 Å/GPa in LiZnSb, and steepest in case of LiZnBi, 0.05 Å/GPa. The decrease in lattice parameter in hexagonal analogues was smaller than their cubic counterpart. The c/a ratio under pressure, except for LiZnN, lied in between 1.62 and 1.58 in the range of 0 to 21 GPa.

Figure 5.3 shows the change in volume under application of pressure. The decrease in volume in cubic LiZnP and LiZnAs was around 0.52 Å^3/GPa, whereas in case of LiZnSb and LiZnBi the decrease in volume was a bit steeper, i.e., 1.46 and 1.88 Å/GPa, respectively. The decrease in volume of hexagonal analogues followed a similar trend, i.e., 0.54 Å^3/GPa in LiZnP, 0.51 Å^3/GPa in LiZnAs, 1.44 Å^3/GPa in LiZnSb, and 2.38 Å^3/GPa in case of LiZnBi. The pressure-volume changes suggest that the LiZnX systems are compressible under application of pressure.

Highlighted in Fig. 5.3, the cubic phase stability of LiZnP up to 12.3 GPa, LiZnAs up to 20.9 GPa whereas the LiZnSb and LiZnBi were stable in cubic phase up to 4.3 GPa and 1.7 GPa, respectively. Beyond the specified range of pressure in respective systems, the hexagonal phase is expected to prevail. The corresponding volumes at which cubic to hexagonal phase transition is expected were about 41, 42, 60, and 69 Å^3/f.u. for LiZnP, LiZnAs, LiZnSb, and LiZnBi, respectively. Likewise, the change in volume on cubic to hexagonal phase transition was 1.2, 1.3, 2.5, and 3.5 Å^3/f.u. for LiZnP, LiZnAs, LiZnSb, and LiZnBi, respectively. The discontinuous change in volume in cubic to hexagonal phase transition indicates the transition is of the first order. Notice that the interest is in studying the transport properties of hexagonal variants of cubic ones, therefore, the extreme pressure range at which hexagonal phases may deform is not demonstrated. The idea is to somehow stabilize the cubic systems in hexagonal ones and explore their transport properties. Above all, it seems pertinent to achieve the hexagonal variants of cubic LiZnX systems by application of the certain degree of pressure.

As outlined in the introduction, the feasibility of polytypism in LiZnX family increases as one moves from LiZnN to LiZnBi, i.e., with the relative expansion of the unit cell. The LiZnSb has already been reported as an instance of polytypism whereas the

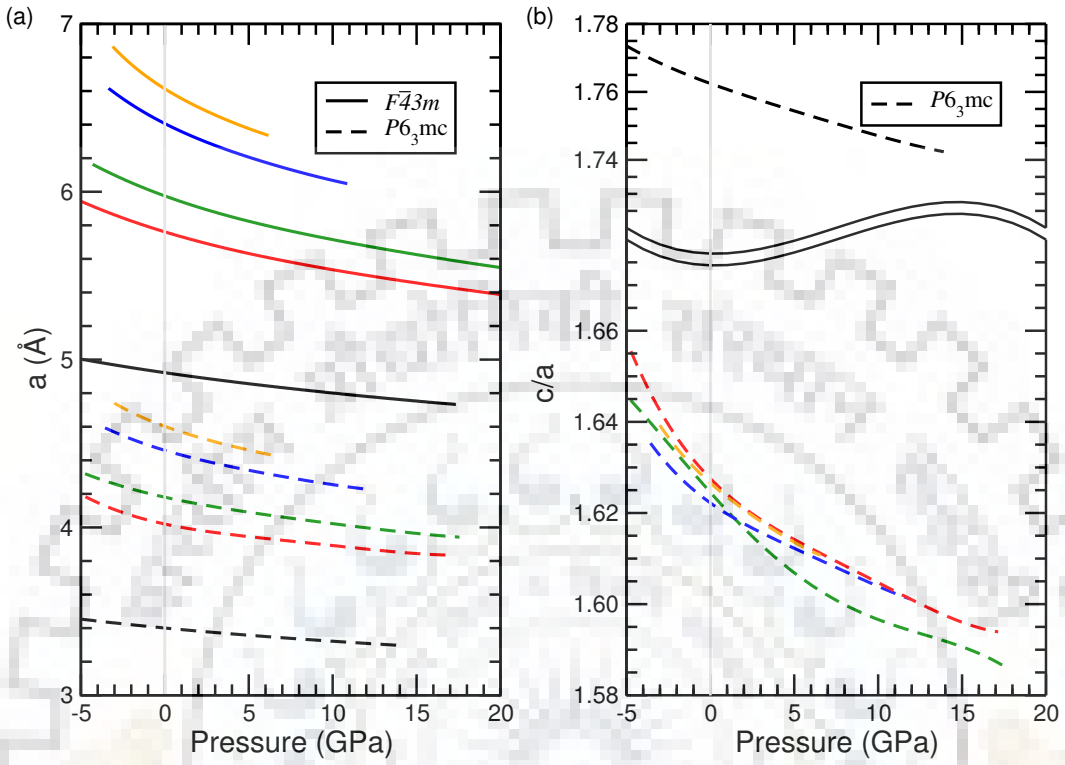

Figure 5.2: (a) Calculated lattice parameter as a function of pressure in cubic $F\bar{4}3m$ and hexagonal $P6_3mc$ symmetry and (b) calculated c/a ratio as a function of pressure in hexagonal $P6_3mc$ symmetry. The solid and dashed lines represent cubic and hexagonal symmetry, respectively. The black, red, blue, green, and orange lines represent LiZnN, LiZnP, LiZnAs, LiZnSb, and LiZnBi, respectively.

calculated results indicate a strong possibility of polytypic behavior in LiZnBi. It is believed that the relative expansion of the unit cell volume will facilitate the polytypism in early members of LiZnX family, i.e., LiZnP and LiZnAs whereas it may induce polytypism in LiZnN. By increasing the unit cell volume, one can tone down the conditions required to carry out the phase transition. Therefore, another perspective to manifest the polytypism in LiZnX systems is introduced: the role of internal pressure. The effect of internal pressure is well-known in inducing phase transition and controlling electronic and magnetic properties in a number of systems. Some of the works on internal pressure can be found in the literature [76, 72, 44, 35].

The internal pressure in a crystal lattice can be achieved either by doping with suitable dopants or introducing the nonreactive entities such as hydrogen or helium in the vacant sites. The doping may result in either positive or negative internal pressure depending upon the choice of dopant whereas the insertion of chemical entities results in

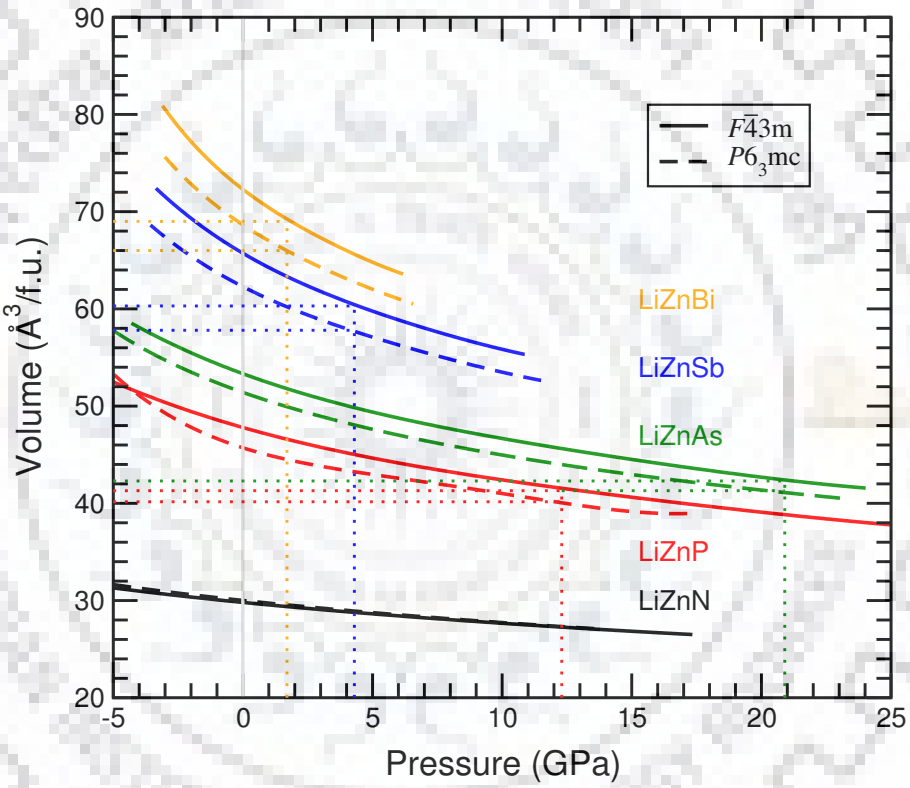

Figure 5.3: Calculated volume per formula unit as a function of pressure in cubic $F\bar{4}3m$ and hexagonal $P6_3mc$ symmetry. The solid and dashed lines represent cubic and hexagonal symmetry, respectively. The dotted lines indicate the volume and pressure at cubic to hexagonal phase transition.

expansion of unit cell, i.e., negative internal pressure. Since the interest lies in the expansion of unit cell volume, the doping of heavier pnictogen atoms in LiZnN, LiZnP or LiZnAs will subsequently expand the crystal lattice and may facilitate the process of polytypism. The choice of pnictogen atoms as dopants also ensures the intact electronic structure.

The introduction of nonreactive elements such as hydrogen and helium in the vacant sites builds the negative internal pressure within the system and eventually expands the crystal lattice. However, it may be challenging to introduce the hydrogen and helium at the vacant sites. The solution phase chemical route could be a favorable approach to achieve the hydrogen insertion. Overall, either doping or hydrogen insertion should be tuned in a way that does not distort the original crystal lattice. The discussion on pressure application suggests that internal pressure can complement the hydrostatic pressure in realizing the polytypism in LiZnX systems.

Thus far, in response to the recently discovered polytypism in LiZnSb, it can be proposed that LiZnBi could be the most promising candidate for polytypism in LiZnX (X = N, P, As, Sb, and Bi) family. In addition, provided certain conditions such as pressure application may also induce the polytypism in LiZnP and LiZnAs. The two symmetries explored in the context of polytypism are $F\bar{4}3m$ and $P6_3mc$. To validate the findings, it is crucial to demonstrate the stability of hypothesized structures i.e stability of LiZnN, LiZnP, and LiZnAs in $P6_3mc$ whereas the stability of LiZnSb and LiZnBi in $F\bar{4}3m$ symmetry. Thuswise, in the next section, the dynamic stability of LiZnX systems in cubic and hexagonal structures is tested.

5.3 Phonon Stability

Phonons are the normal modes or quantum of vibrations in a crystal and are an indicative of the stability of a system. In order to be dynamically stable, the phonon frequencies of a system should be real and not imaginary [39, 137]. Table 5.3 summarizes the results of phonon calculations. The '+' sign indicates the positive frequencies throughout the Brillouin zone whereas the '–' sign shows the existence of negative frequencies within the system. Thus, the '+' and '–' sign implies the stability and instability, respectively, in the system.

Remarkably, all LiZnX systems in $F\bar{4}3m$ and $P6_3mc$ symmetry had positive phonon frequencies and were stable in nature. However, with LiZnBi as an exception, all the systems in $P6_3/mmc$ symmetry were predicted to be unstable. As investigated earlier, the relative energy of LiZnX systems in $P6_3/mmc$ symmetry was quite high, phonon

System	$F\bar{4}3m$	$P6_3/mmc$	$P6_3mc$
LiZnN	+	–	+
LiZnP	+	–	+
LiZnAs	+	–	+
LiZnSb	+	–	+
LiZnBi	+	+	+

Table 5.3: The phonon frequencies of LiZnX family in $F\bar{4}3m$, $P6_3/mmc$, and $P6_3mc$ symmetry. '+' and '–' indicates the positive and negative phonon frequencies, respectively.

calculations further confirm the non-existence of LiZnX systems in $P6_3/mmc$ symmetry. Therefore, any possibility of polytypism in LiZnX family in $P6_3/mmc$ symmetry is ruled out. Given that one of the objectives is to study the polytypism in all LiZnX systems, the stability of LiZnX in both $F\bar{4}3m$ and $P6_3mc$ symmetry lends enough support to the purpose. The energy profile and dynamic stability collectively suggest that not only LiZnSb but other members of LiZnX family are also probable of polytypism in $F\bar{4}3m$ and $P6_3mc$ symmetry.

Before proceeding ahead, the questions posed in this chapter regarding the polytypism in LiZnX (X = N, P, As, Sb, and Bi) systems are addressed. *What is the driving force for polytypism in LiZnSb?* The calculations suggest that the competitive energies of cubic and hexagonal phases could be the possible reason behind polytypism in LiZnSb, in addition to underlying mechanisms. *Is it achievable by varying the synthesis techniques only or the transformation is pressure driven? Is it limited only to LiZnSb or also possible for other members of LiZnX family?*

White et al. revealed the first instance of cubic LiZnSb by solution phase method despite the previously known hexagonal phase by solid-state technique. However, the same group achieved the cubic phase of LiZnP by solution phase method in accordance with the solid-state synthesis of cubic LiZnP. Thus, merely varying the synthesis technique may not lead to different phases. Through first-principles calculations, it has been demonstrated that by application of the certain degree of pressure, the previously known cubic LiZnP and LiZnAs could be realized in hexagonal symmetry. Likewise, the cubic LiZnSb and LiZnBi could be transformed into hexagonal analogues by application of pressure. Note that the cubic LiZnSb and LiZnBi are reported to be stable in this study despite the previously known hexagonal phases.

Is it restricted to $F\bar{4}3m$ and $P6_3mc$ or also possible in closely related $P6_3/mmc$

symmetry? The relative energy of LiZnX systems in $P6_3/mmc$ symmetry was quite high in comparison to $F\bar{4}3m$ and $P6_3mc$ symmetry. Further, phonon calculations confirmed the dynamic instability of LiZnX systems in $P6_3/mmc$ symmetry. *Will transport properties be affected by the phase transition?* To investigate the effect of polytypism on TE properties which is the focus of the chapter, the electrical and thermal transport properties of LiZnX systems in cubic $F\bar{4}3m$ and hexagonal $P6_3mc$ symmetries are surveyed next.

5.4 Transport Properties

In this section, first, the optimal doping levels at which the maximum power factor (PF) in cubic and hexagonal LiZnX systems can be obtained at different temperatures, are highlighted. The prediction of optimal doping enables the experimentalists to aim at specific doping levels while seeking the best TE composition. Then, the plausible explanation of the behavior of PF, Seebeck coefficient, and electrical conductivity in terms of electronic features are discussed. For convenience, hereafter, the terms c-LiZnX for cubic, h-LiZnX for hexagonal, p-LiZnX for hole-doped, and n-LiZnX for electron-doped LiZnX systems are used.

The rigid band approximation (RBA) was employed to calculate the electrical transport properties of LiZnX (X = N, P, As, and Sb) systems. The constant relaxation time approach was also used which considers the Seebeck coefficient to be independent of relaxation time τ, whereas the electrical conductivity and PF are presented using $\tau = 10^{-14}$ s. The constant relaxation time approach has been a useful paradigm for predicting the TE properties through *ab initio* approach. Madsen, in his work, utilized τ = 2 x 10^{-14} s while exploring the TE potential of LiZnSb [99] which was later found in agreement by Toberer and group [135]. Toberer et al., with the help of Drude model of conductivity and experimentally determined values for the mobility and effective mass, used an average value, $\tau = 10^{-14}$ s, for ZT estimates of p-LiZnSb. In a theoretical investigation on c-LiZnX systems, a relaxation time of $\tau = 10^{-14}$ s was used for predicting PF values [149]. Recently, White et al. used κ_l/τ = 1 x 10^{14} for calculating the figure of merit of c-LiZnSb [141]. Overall, in LiZnX systems, the relaxation time value of $\tau = 10^{-14}$ has been quite an appropriate figure to predict the transport properties. Therefore, the select of τ is quite a rationale which is based on previous theoretical and experimental works.

Generally, the Seebeck coefficient is maximum when the Fermi level is near the middle of the band gap and decreases as the Fermi level deviates either into valence band or conduction band with doping. Unlikely, the electrical conductivity increases with increasing

density of states on either electron or hole doping. The combined effect results in a maximum PF somewhere near the band edge. This is what has been observed for LiZnX systems in both cubic and hexagonal symmetries. As illustrated in Figs. 5 and 6, the maximum PF on either hole or electron doping is observed near the band edge in LiZnX systems in cubic and hexagonal symmetry, respectively. At higher doping levels, the PF falls gradually as the Seebeck coefficient gets significantly reduced. The data on PF and doping levels are presented in light of experimental evidence on few LiZnX systems. Recently, polycrystalline samples of $LiZn_{1-x}As$ were successfully synthesized with less than 15% doping by solid-state reaction [23]. The DTA measurements have shown that the melting temperature of LiZnP [92] and LiZnAs [89] are 850 and 950 ^{0}C, respectively.

Optimistic of the findings, the PF values at room temperature 300 K, 500 K, and as high as 700K are presented while the doping levels are considered up to 0.2 charge carriers per unit cell (e/uc), i.e., 20%. However, for better illustration, the doping levels are shown up to 0.4 e/uc. Before analyzing case by case at different temperatures in different symmetries, some trends in PF and doping values of LiZnX which are common to both cubic and hexagonal symmetry are discussed. The PF increased on going from 300 K to 700 K at all doping levels, depicting the increasing trend of PF with temperature. In all the cases, the maximum PF was obtained at 700 K. Interestingly, within a particular type of doping i.e n-type doping, the hexagonal analogues of LiZnX had higher PF than their cubic counterpart whereas in p-doped LiZnX systems the PF was higher in cubic symmetry. Overall, at all considered temperatures, LiZnN was found to have maximum PF on hole doping whilst rest members of LiZnX family had better PF on electron doping in either symmetry.

The optimal doping levels at which maximum PF was obtained shifted toward higher values with increasing temperature i.e one has to introduce more number of charge carriers to achieve maximum PF at a higher temperature. The optimal doping levels for p-type doping ranges in between 0.004-0.115 e/uc which seems quite reasonable for experimental realization. For n-type doping, the optimal doping values were comparatively higher and ranges from 0.066 to as high as 0.347 e/uc. The relevance and acceptability of some higher doping levels are questioned ahead. Briefing the general features of PF of LiZnX systems in cubic and hexagonal symmetry, next, the focus is on the PF and doping of LiZnX systems at different temperatures in different symmetries. Figure 5.4 shows the PF as a function of doping of LiZnX systems at 300, 500, and 700 K in cubic $F\bar{4}3m$ symmetry. The optimal doping levels for p-LiZnN were 0.01, 0.021, and 0.035 e/uc at 300, 500 and 700 K, respectively. The corresponding values of PF were 19.65, 40.41, and 65.17 μW cm^{-1}

K^{-2}. The values of PF on electron doping were not convincing even at high electron doping levels, as explained in next section. Thus, only hole doping is worth considering in *c*-LiZnN. Unlike LiZnN, the electron doping was more favorable in LiZnP. The optimal doping levels on electron doping were 0.189, 0.201, and 0.215 e/uc at 300, 500, and 700 K, respectively, the accompanying PF values were 21.11, 49.64, and 83.80 μW cm^{-1} K^{-2}.

It was mentioned before that in light of experimental doping levels, the results were proposed up to 0.20 e/uc. However, only a couple of doping levels exceeded the defined limit. Since the doping level 0.215 e/uc was not far away from 0.20 e/uc, the PF bore close resemblance at the two doping levels, i.e., 83.80 μW cm^{-1} K^{-2} at 0.215 e/uc and 83.65 μW cm^{-1} K^{-2} at 0.20 e/uc. Therefore, the actual figures are included in order to provide an exact framework to experimentalists. Moreover, in Fig. 5.4(b), a careful observation of *n*-type doping branch of LiZnP revealed a smaller peak of PF on minimal doping complementing the higher PF peak. The inset of Fig. 5.4(b) shows the enlarged view of the same. At the smaller peak, the PF values were 8.64, 18.90, and 31.48 μW cm^{-1} K^{-2} at 0.003, 0.007, and 0.011 e/uc optimal doping levels, respectively, corresponding to 300, 500 and 700 K. The values are not worthy of attention in comparison to the larger peak, however, the PF at 700 K, i.e., 31.48 μW cm^{-1} K^{-2}, is still an appreciable number. Acknowledging the experimental challenges, the proposed high optimal doping levels of LiZnP are not of much concern since the minimal doping level may also provide a reasonable PF, if not great.

Moving on to the next systems LiZnAs and LiZnSb, Fig. 5.4(c) and (d), the better PF values were obtained on electron doping. The PF values of *n*-LiZnAs were 23.26, 52.98, and 86.86 μW cm^{-1} K^{-2} at 0.068, 0.072, and 0.077 e/uc doping levels, respectively, corresponding to 300, 500, and 700 K. The recently found polytypic LiZnSb has some interesting features to look upon. The optimal doping levels for *n*-LiZnSb were 0.140, 0.149, and 0.161 e/uc at 300, 500, and 700 K, respectively. The corresponding values of PF were 29.82, 72, and 123.92 μW cm^{-1} K^{-2}. The PF values of LiZnSb are quite impressive and best among the LiZnX systems in cubic symmetry. The recent solution phase synthesis of *c*-LiZnSb and impressive values of PF further strengthens the motive of polytypism induced TE properties in LiZnX systems. An important observation, similar to LiZnP, was the appearance of a small peak at minimal doping at 300 K. However, unlike LiZnP, the peak disappeared at higher temperatures. The inset of Fig. 5.4(b) highlights the obscured smaller peak at 300 K on *n*-type doping. The PF at this second peak was 14.83 μW cm^{-1} K^{-2} at a minimal doping of 0.008 electrons per unit cell. Let us now look at the other part of Fig. 5.4(d), the hole doping side. At 300 K, corresponding to optimal doping level 0.004 e/uc, the value of PF was 14.54 μW cm^{-1} K^{-2}. The similar values of PF on

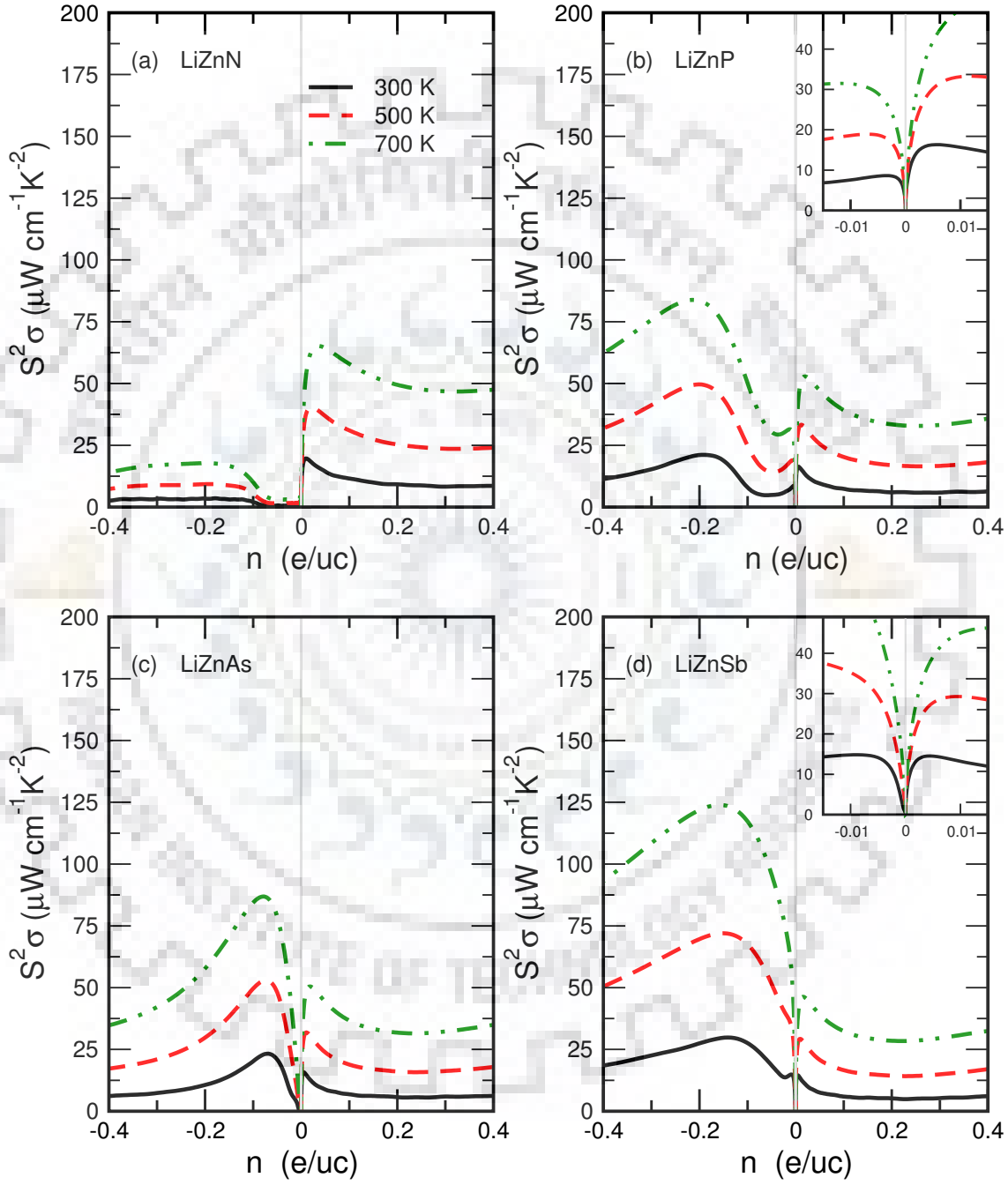

Figure 5.4: Calculated power factor as a function of doping per unit cell in LiZnX (X = N, P, As, Sb) systems at 300, 500, and 700 K, in $F\bar{4}3m$ symmetry, assuming $\tau = 10^{-14}$ s. The '+' and '–' sign on horizontal axes respresents hole and electron doping, respectively.

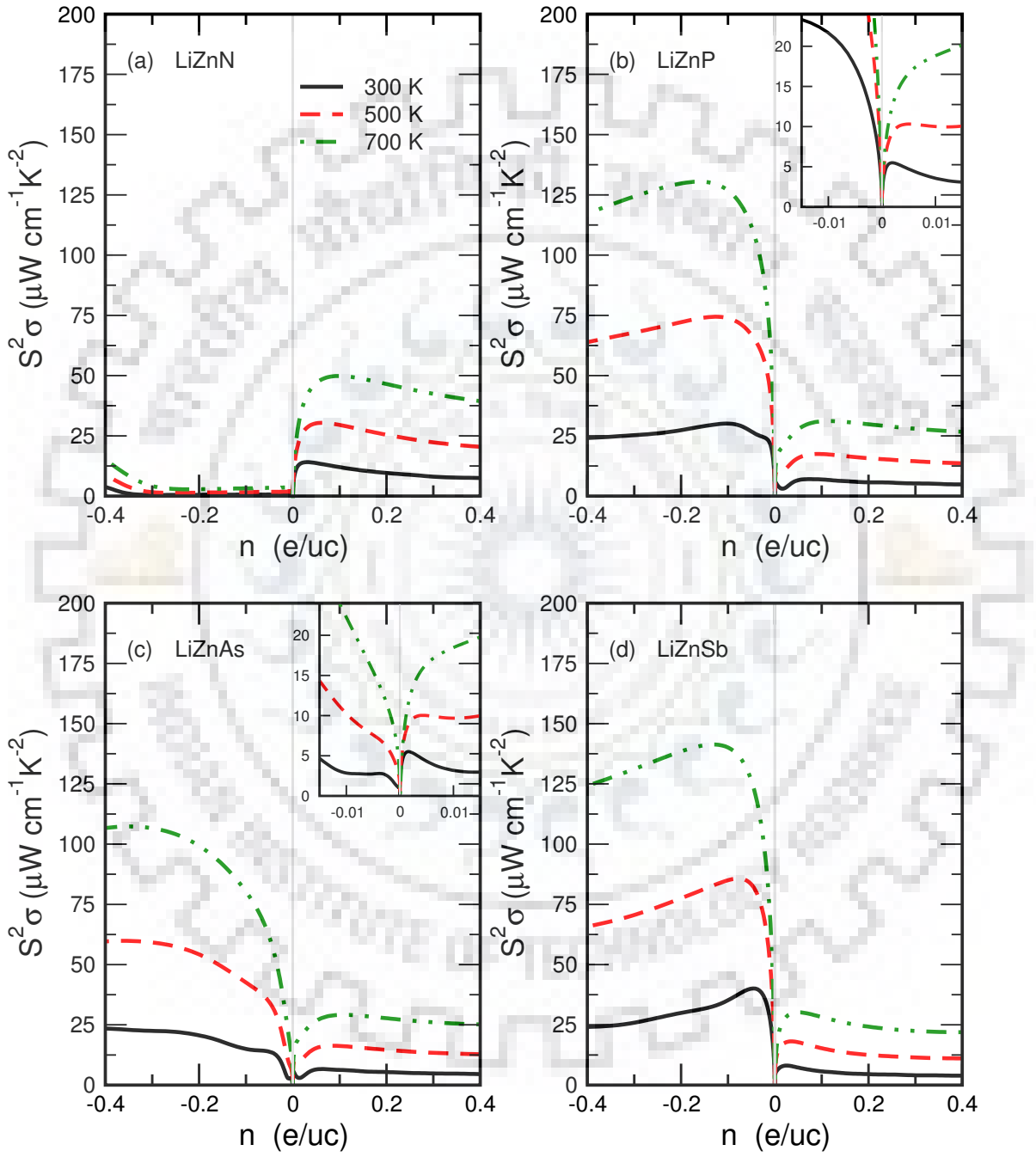

Figure 5.5: Calculated power factor as a function of doping per unit cell in LiZnX (X = N, P, As, Sb) systems at 300, 500, and 700 K, in $P6_3mc$ symmetry, assuming $\tau = 10^{-14}$ s. The '+' and '–' sign on horizontal axes respresents hole and electron doping, respectively.

p-type and *n*-type doping is the most intriguing correlation.

For device fabrication, it is highly desirable to have *n*-type and *p*-type branches of similar TE material or ideally of the same material, which is rare. Usually, the performance of one type is inferior to the other [37]. Thus, *c*-LiZnSb could be used for making both *n*-type and *p*-type legs of a TE module. Unfortunately, the PF at 300 K for the two legs were not substantial. However, considering the benefits of different legs of the same material, *c*-LiZnSb could be used in room temperature TE applications requiring less efficiency. Turning now to the hexagonal symmetry, the PF as a function of doping for LiZnX systems is shown in Fig. 5.5. Alike cubic analogue, the *h*-LiZnN also had higher values of PF on hole doping. Yet again, there was no significant PF whatsoever on electron doping even at higher doping levels at all temperatures. The optimal doping levels at which maximum PF was obtained for *p*-LiZnN were 0.030, 0.062, and 0.096 e/uc at 300, 500, and 700 K, respectively. The values of PF at optimal doping levels were 14.08, 30.40, and 49.84 μW cm^{-1} K^{-2}.

In case of *h*-LiZnP, the electron doping dominated at all temperatures. The optimal doping levels for maximum PF in *n*-LiZnP were 0.102, 0.126, and 0.164 e/uc at 300, 500, and 700 K, respectively. The maximum value of PF at 300 K was 30.07 which drastically increased to 74.42 and 130.49 μW cm^{-1} K^{-2} at 500 and 700 K, respectively. Similar to *c*-LiZnP, a small peak of PF appeared at minimal doping. However, here it appeared on *p*-type doping side contrary to *n*-type in *c*-LiZnP. The inset of Fig. 5.5(b) highlights that the small peak at minimal doping which emerged on hole doping side persists till 500 K and disappears thereafter. Since the best values of PF were achievable at *n*-type doping, the low PF value at smaller peak was not worth considering. A similar trend was observed for *h*-LiZnAs. In addition to the dominant peak, a small peak was observed at minimal hole doping at 300 K which survived till 500 K. Unfortunately, yet again, the smaller peak corresponded to the less favorable PF and could not assist the high optimal doping levels of LiZnAs. The optimal doping levels of *n*-LiZnAs at three defined temperatures were beyond 0.30 e/uc. Restricting to the described limit of 0.20 e/uc, the PF values were not far behind than the peak values. This was because of the steady increase in PF with doping, unlike other cases where the PF peak was relatively steeper. The values of PF were 20.79, 54.80, and 100 μW cm^{-1} K^{-2} at 300, 500, and 700 K, respectively, at 0.20 e/uc.

Now, the most promising candidate thus far, *h*-LiZnSb is discussed. What makes LiZnSb particularly interesting is the excellent values of PF in cubic phase and the recent experimental realization in cubic symmetry. Further, Madsen's prediction of *h*-LiZnSb as a potential TE material drives the interest in its properties. The optimal doping levels for *n*-LiZnSb were 0.046, 0.076, and 0.134 e/uc at 300, 500, and 700 K, respectively. The

System	T (K)	n (e/uc)	$S^2\sigma$ (μW cm^{-1} K^{-2})	ZT
LiZnN	300	+0.010 (+0.030)	19.65 (14.08)	0.14 (0.10)
	500	+0.021 (+0.062)	40.41 (30.40)	0.36 (0.29)
	700	+0.035 (+0.096)	65.17 (49.84)	0.55 (0.90)
LiZnP	300	-0.189 (-0.102)	21.11 (30.07)	0.15 (0.24)
	500	-0.201 (-0.126)	49.64 (74.42)	0.47 (0.92)
	700	-0.215 (-0.164)	83.80 (130.49)	0.78 (1.96)
LiZnAs	300	-0.068 (-0.20)	23.26 (20.79)	0.17 (0.16)
	500	-0.072 (-0.20)	52.98 (54.80)	0.50 (0.67)
	700	-0.077 (-0.20)	86.86 (100.00)	0.82 (1.49)
LiZnSb	300	-0.140 (-0.046)	29.82 (40.10)	0.22 (0.32)
	500	-0.149 (-0.076)	72.00 (85.73)	0.98 (1.04)
	700	-0.161 (-0.134)	123.92 (141.32)	1.27 (1.95)

Table 5.4: Calculated optimal doping levels n, power factor $S^2\sigma$, and ZT of LiZnX (X = N, P, As, Sb) systems at 300, 500, and 700 K in cubic $F\bar{4}3m$ symmetry. The values in hexagonal $P6_3mc$ symmetry are enclosed in parentheses. '+' and '–' sign represents p-type and n-type doping, respectively. The relaxation time is taken to be $\tau = 10^{-14}$ s.

optimal doping levels at 300 and 500 K were quite acceptable in comparison to other n-type hexagonal systems whereas the value at 700 K was within the described limit of doping. The PF values at optimal doping levels were 40.10, 85.73, and 141.32 μW cm^{-1} K^{-2}. As expected, the PF values were tremendous and turn out to be the best in the detailed survey of transport properties of LiZnX systems in cubic and hexagonal symmetry. As put forward by Madsen [99] for h-LiZnSb and later by White [141] et al. for c-LiZnSb, the calculated results also indicate the TE potential of cubic and hexagonal LiZnSb.

In addition to PF, the carrier concentration and Seebeck coefficient at optimal doping levels ranges 10^{20}-10^{21} cm^{-3} and 20-138 μV K^{-1}, respectively, in either symmetry. Having discussed in detail the trend and values of PF as a function of doping in LiZnX systems at different temperatures, some salient features of PF values and the significance of actual numbers are discussed next. It was found that h-LiZnX systems had higher PF values than the cubic ones at optimal doping levels. Returning to the question posed in the beginning, it can be stated that the hexagonal polytypes of prevailing cubic LiZnN, LiZnP, and LiZnAs will have improved values on n-type doping, provided pressure driven cubic to hexagonal phase transition. Nonetheless, the cubic and hexagonal variants of LiZnSb have

equally competitive figures.

As far as actual numbers are concerned, the PF values at 300 K ranges in between 19-29 μW cm^{-1} K^{-2} for cubic symmetry whereas for hexagonal systems the values lie in between 14-40 μW cm^{-1} K^{-2}. At 500 K, the PF values were much improved and lies in the range of 40-72 and 30-85 μW cm^{-1} K^{-2} for cubic and hexagonal systems, respectively. However, the PF values at 700 K were highly impressive for both cubic and hexagonal symmetry and lies in an overwhelming range of 65-123 and 49-141 μW cm^{-1} K^{-2}, respectively. Further, excluding LiZnN, despite the higher PF values obtained at n-type doping, the values of p-doped cubic LiZnX systems at 700 K are not completely inconsiderable. The PF values of cubic LiZnP, LiZnAs, and LiZnSb corresponding to optimal doping levels 0.115, 0.108, and 0.049 e/uc were 31.14, 29.15, and 30.20 μW cm^{-1} K^{-2} at 700 K, respectively. The optimal doping levels, as can be seen in Fig. 5.4, were even lower at 300 K and ranges in between 0.004-0.005 e/uc. To give a complete picture to experimentalists, the varying doping levels at varying temperatures and at either hole or electron doping are also featured. In case one wish to substitute smaller values of dopants keeping an eye on experimental conditions, he may go for p-type doping in c-LiZnX systems rather than aiming high PF values in n-type doping.

As mentioned in the beginning that Nowotny-Juza phases are a special derivative of hH alloys, thus, a requisite comparison between the two would be worthwhile. Despite the lowest values of PF in LiZnX systems at 300 K, the values are competitive enough with conventional CoTiSb based materials [145, 116]. Remarkably, the PF values of LiZnX systems at 500 K outclass even the best performing hH alloy, FeNbSb [156]. Further, the numbers of PF at 700 K in LiZnX systems are too overwhelming to commensurate with parent hH alloys. Altogether, thus far, the evaluation of transport properties implicate that LiZnX systems could be a new potential class of TE materials.

The only predicament could be high thermal conductivity which may restrict the ZT values. Specifically, the c-LiZnX systems may have high values of κ on account of diamondlike network between Zn and X. Madsen used an estimated value of lattice thermal conductivity, $\kappa_l = 2$ W m^{-1} K^{-1}, up to 600 K to calculate ZT of h-LiZnSb [99]. Toberer, at a particular carrier concentration, experimentally found that the κ of h-LiZnSb varies approximately from 6 to 5 W m^{-1} K^{-1} whereas the κ_l is of the order of 4-3 W m^{-1} K^{-1} at 300-525 K [135]. In another work, κ_l of h-LiZnSb was measured to be 4.5 W m^{-1} K^{-1} at 300 K [86]. Nevertheless, over the years, the κ has seen a progressive decrement in a number of systems by isoelectronic alloying, doping or nanostructuring [131, 24, 65].

Furthermore, Cahill proposed the theoretical lower limit to the thermal conductiv-

ity κ_{min} of disordered crystals wherein he established that the κ_{min} of Si and Ge are 0.6 and 0.9 W m^{-1} K^{-1} at 300 K [15]. Keeping in mind the similarity of dominant Zn-X framework in LiZnX systems with diamondlike Si and Ge structure and little exploration of transport properties of LiZnX systems, the analogy is extended to correlate their κ values. Hence, it is believed that κ of LiZnX systems can be reduced significantly to meet the defined κ_{min}. The assumption is optimistic but the idea is to provide an intuitive estimate of κ_{min} values of LiZnX systems. Even κ of 1 W m^{-1} K^{-1} would yield excellent figure of merit.

Despite some failures, the theoretical κ_l values of cubic and hexagonal LiZnX systems are currently being investigated. For this study, κ_e of the parent LiZnX systems was calculated by Boltztrap code and an estimated value of lattice thermal conductivity, κ_l = 3.5 W m^{-1} K^{-1}, is used. Rather than selecting a random constant number of κ_l, the experimentally reported κ_l values of h-LiZnSb are exploited. Toberer [135] reported κ_l $\sim$ 4-3 W m^{-1} K^{-1} in the temperature range 300-525 K whereas Kishimoto [86] reported κ_l $\sim$ 4.5 at 300 K. An average value of κ_l = 3.5 W m^{-1} K^{-1} is chosen in this chapter for estimating the ZT values. This value is not overly optimistic because κ_l is known to decrease with temperature. Given that the PF values of the interest are observed at 700 K, the value of κ_l is indeed on a higher side.

Incorporating the κ values as per the discussion, some encouraging values of ZT were obtained for experimentalists, listed in Table 5.4. The ZT values of LiZnX systems ranges in between 0.10-0.32 at 300 K in cubic and hexagonal symmetry. At 500 K, the ZT values were in the range of 0.36-0.98 and 0.29-1.04 for cubic and hexagonal symmetry, respectively. The best ZT values, as expected, were obtained at 700 K and ranges 0.55-1.27 in case of cubic symmetry whereas 0.90-1.95 for hexagonal symmetry. The most striking values to emerge out from the Table 5.4 were of cubic and hexagonal LiZnSb. The ZT values of cubic and hexagonal LiZnSb at 700 K were 1.27 and 1.95, respectively, which were complemented by h-LiZnP and h-LiZnAs. The ZT values of h-LiZnP and h-LiZnAs at 700 K were 1.96 and 1.49, respectively.

Taken together, the findings suggest a promising scope of LiZnX systems in TE applications. The investigations in this direction are in progress and are likely to explore more corroboration in favor of polytypism and transport properties. As of now, due to lack of experimental investigations of LiZnX systems from the TE perspective, the findings of this chapter are compared with previously calculated values. The prediction of hexagonal n-LiZnSb as a potential TE material is in line with Madsen's prediction. Madsen [99] proposed ZT $\sim$ 2 at 600 K for h-LiZnSb whereas the calculated value of ZT is 1.95 at 700 K. The carrier concentration values of p-LiZnSb are fairly consistent with Toberer's

reported values [135].

In case of *c*-LiZnX systems, except *n*-LiZnAs and *n*-LiZnSb, the predicted optimal doping levels and PF values at 300 K in cubic symmetry are consistent with a previous theoretical work within low doping levels [149]. Furthermore, the calculated ZT value of cubic *n*-LiZnSb is 1.27 at 700 K in comparison to 1.64 at 600 K proposed by White et al [141]. The slightly lower projected value can be attributed to the choice of different κ_l values. While White et al. assumed $\kappa_l/\tau = 1 \text{ x } 10^{14}$ W m^{-1} K^{-1} s^{-1}, taking experimental values of κ_l into consideration, $\kappa_l = 3.5$ W m^{-1} K^{-1} is utilized in this chapter.

In spite of this, a much lower value of ZT in case of cubic *p*-LiZnSb was obtained. Whereas White reported $ZT \sim 1.43$ at 600 K, the calculated value was only 0.47 at 700 K. Nevertheless, with little experimental investigations, the results are mostly in agreement with previously calculated values. In the next section, the electronic structure of cubic and *h*-LiZnX systems are studied to delve deeper into the trend and figures of PF and doping type.

5.5 Electronic Structure

The calculated electronic band structures of LiZnX (X = N, P, As, and Sb) systems in $F\bar{4}3m$ and $P6_3mc$ symmetry are illustrated in Figs. 7 and 8, respectively. It can be seen, except *c*-LiZnP, the valence band maximum (VBM) and conduction band minimum (CBM) of all the systems were located at Γ point in both cubic and hexagonal symmetry, resulting in the direct band gap. In case of *c*-LiZnP, the VBM and CBM were located at different wave vectors Γ and X, respectively, making it indirect band gap semiconductor. The optical measurements demonstrated direct band gap of *c*-LiZnN [90] whereas *c*-LiZnP [92] was found to be an indirect band gap semiconductor. However, previous calculations have also reported indirect band gap in case of *c*-LiZnP [82].

The VBM and CBM edges were dominated by *p*-states of pnictogen atoms and Zn *d*-states (not shown for clarity). The states near VBM had a major contribution from pnictogen atoms whereas states close to CBM were dictated by Zn. There was hardly any contribution from Li in cubic structures, however, Li contributed in states close to CBM in hexagonal symmetry. Such information can be helpful in deciding the dopants in synthesis. For instance, any doping at Li site may not affect VBM in either symmetry whereas doping at Zn and pnictogen site may alter the electronic features. Thus, one can choose the dopants to manipulate the properties as desired. Further, the choice of dopant should be cost-effective and more suitably of similar size to the atom to be replaced. The

most suitable dopants for n-type doping in LiZnX systems could be Ga/In/Ge for Zn and Se/Te for Sb. The favorable dopants for p-type doping are Co/Fe in place of Zn and Sn/Ge for Sb.

Returning to the band structure, the shift of Fermi level corresponding to optimal doping levels at which maximum PF was obtained at 700 K is highlighted in Figs. 7 and 8. The red dashed line corresponds to p-type whereas blue line to the n-type doping. The cubic symmetry is focussed first. A common observation among the cubic systems was the threefold degeneracy of VBM. Two bands were degenerate in L-Γ and Γ-X direction, the third band was degenerate at Γ point, Fig. 5.4. The degenerate bands comprised two relatively heavy and other lighter band which plays an important role in transport properties. The flat and heavy band signifies heavy effective mass of charge carriers which improves Seebeck coefficient whereas the lighter one facilitates the mobility of charge carriers, thereby improving the PF. The bands close to VBM were almost identical in all the systems and it was the CBM which is governing the type of doping.

Fig. 5.6, the presence of single parabolic and dispersed band at CBM is an indicative of poor PF on hole doping whereas the CBM of other systems was relatively flat and degenerate at some point with higher bands. This explains the poor PF values on n-type doping in c-LiZnN as compared to other systems. The combination of heavy and light bands at VBM, as described above, makes p-type doping more favorable in c-LiZnN. In other systems, the more favored n-type doping can be attributed to the dominating features of CBM but the advantages of degenerate heavy and light bands at VBM cannot be completely ignored.

The mild optimal p-type doping levels in c-LiZnX systems are attractive from the experimental viewpoint, as noted in transport properties section. Further, the degenerate bands at VBM assure appreciable figures of PF if not significant compared to n-type doping. Regarding other systems, the CBM was flat and nondispersive in L-Γ direction followed by a more dispersed nature in Γ-X direction. Here, the single band promotes both Seebeck coefficient and electrical conductivity. The flat band was further assisted by a more dispersed band degenerate somewhere in between X-W direction, depending on the system. Note that this band was degenerate with other higher light bands which influence higher electrical conductivity. Collectively, the PF was improved on n-type doping in other c-LiZnX systems.

The lookalike features of CBM of c-LiZnP and c-LiZnAs were responsible for their similar PF values, 83 and 86 μW cm^{-1} K^{-2}, respectively. The higher PF of n-LiZnSb (123 μW cm^{-1} K^{-2}) was because of two factors. First, the CBM of LiZnSb was flatter in L-Γ and Γ-X direction. The contribution of heavy electrons from L and X pocket and lighter

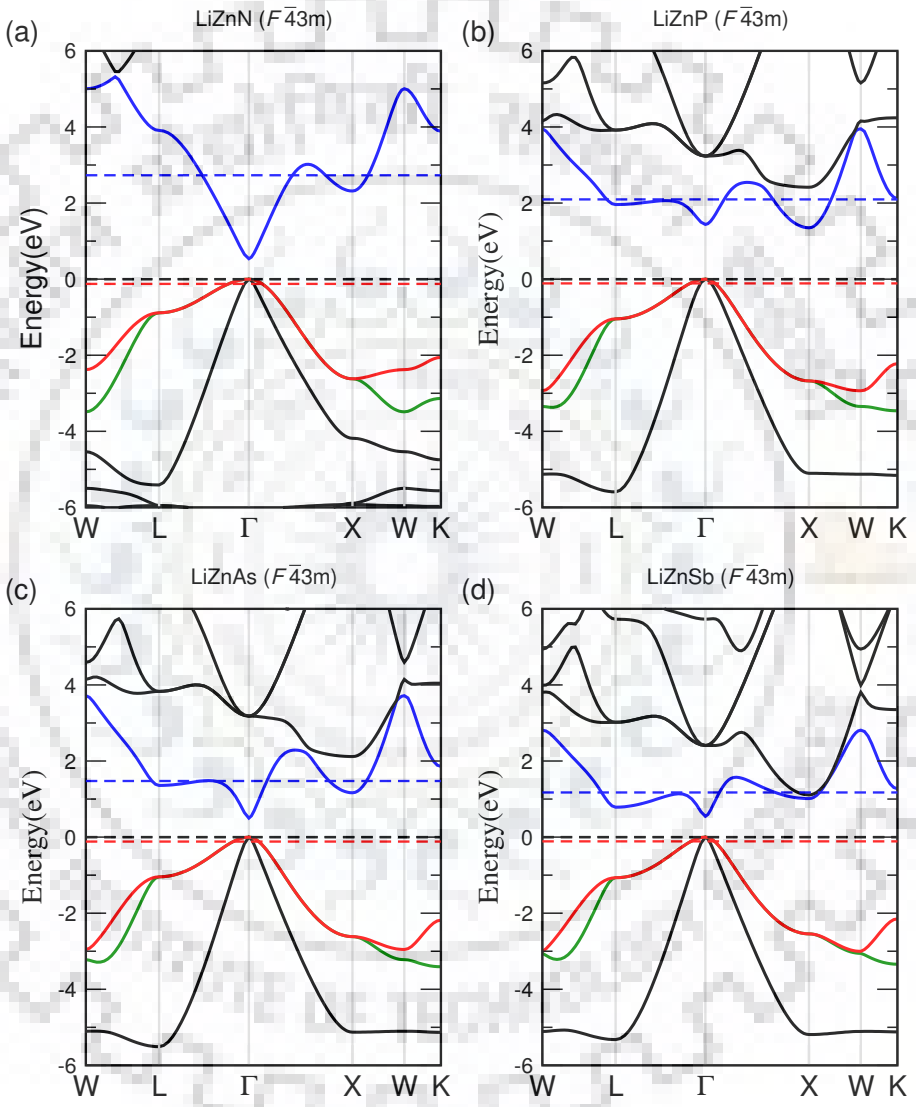

Figure 5.6: Calculated electronic band structures of LiZnX (X = N, P, As, Sb) systems in $F\bar{4}3m$ symmetry. The valence band edge is set at zero on the energy axis and represented by a black dashed line. The shift of Fermi level at optimal hole and electron doping at 700 K is highlighted by red and blue dashed line, respectively.

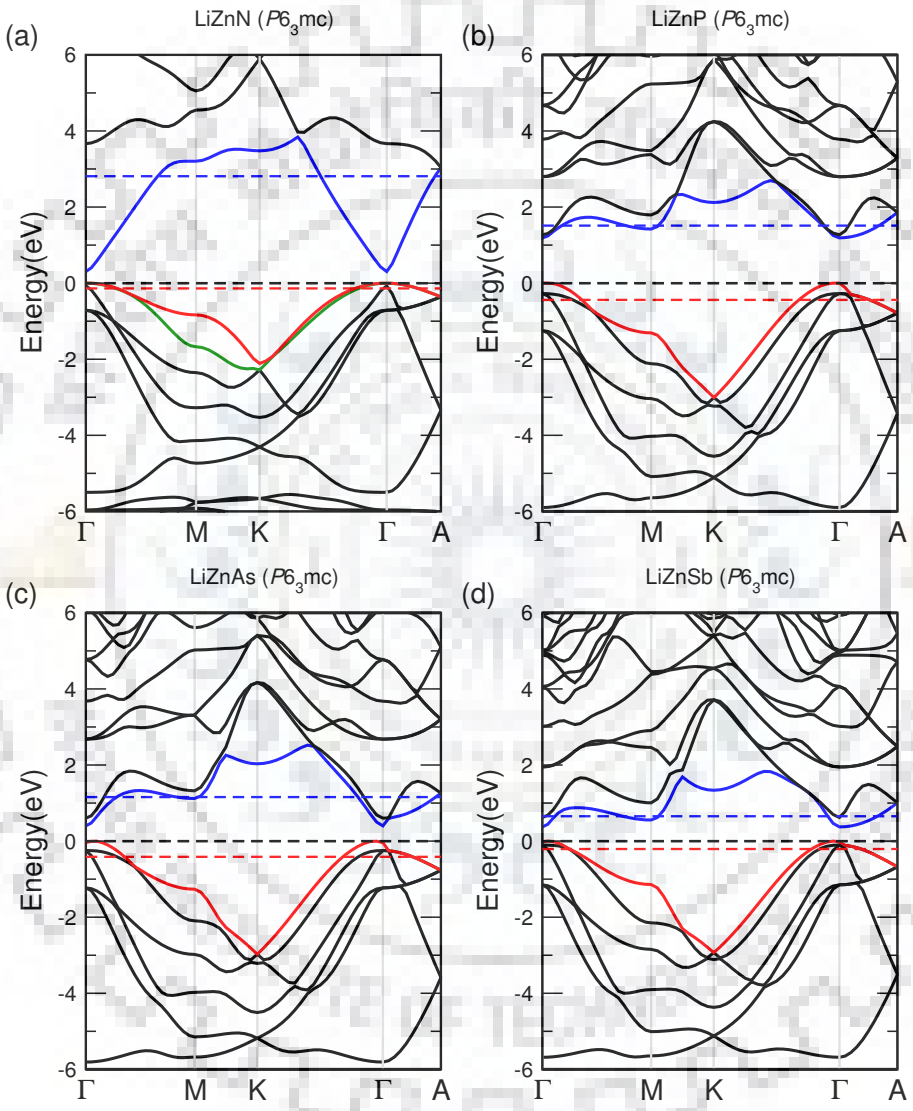

Figure 5.7: Calculated electronic band structures of LiZnX (X = N, P, As, Sb) systems in $P6_3mc$ symmetry. The valence band edge is set at zero on the energy axis and represented by a black dashed line. The shift of Fermi level at optimal hole and electron doping at 700 K is highlighted by red and blue dashed line, respectively.

electrons from Γ pocket maximizes the PF. Secondly, the contribution of electron pocket of the CBM-1 band at X point was more as compared to LiZnP and LiZnAs.

Similar to cubic symmetry, the VBM of all the systems was more or less same in hexagonal symmetry also. The evaluation of CBM features will be more usable in governing the doping type. In case of *h*-LiZnN, once again the single dispersed band was indicative of low PF on electron doping, as proven in the previous section. The VBM of *h*-LiZnN was twofold degenerate at Γ. The heavy hole contribution was expected from pockets in Γ-A region. In rest of all cases, the CBM had a flat band in Γ-X direction which became more dispersed along the direction M-K-Γ-A. The heavy electrons contribution from flat band region and lighter ones from dispersed band region suggest that *n*-type doping was more favorable. In comparison, the bands at VBM were relatively more dispersed and flat region responsible for better Seebeck coefficient was missing. Except for *h*-LiZnN, the electron pockets at Γ and M points were responsible for high PF in *h*-LiZnX systems. A description of electronic features of *h*-LiZnSb can be also be found in Madsen's work [99].

5.6 Discussion and Conclusions

Different polytypes in many cases are known to exhibit different properties. In a recent major advance, LiZnSb was found to be polytypic and the thermoelectric efficiency of recently found cubic analogue and hitherto hexagonal LiZnSb were quite magnificent. In order to understand the driving force behind polytypism and its possible existence in other Li based Nowotny-Juza phases with particular emphasis on thermoelectric properties, the LiZnX (X = N, P, As, Sb, and Bi) systems in cubic and hexagonal symmetry were investigated in this chapter.

The detailed theoretical investigations of polytypism in LiZnX systems and its effect on transport properties revealed some interesting features. In addition to polytypic LiZnSb, LiZnBi turned out to be the most probable system to exhibit the phenomenon. It was found that the cubic phase of LiZnBi, similar to LiZnSb, had lower energy in comparison to existing hexagonal phase. The other cubic members LiZnP and LiZnAs were also likely to undergo cubic to hexagonal phase transition under a certain degree of pressure. Likewise, the cubic LiZnSb and LiZnBi could be pressure driven to respective hexagonal phases. It was found that the pressure driven phase transition could be aided by internal pressure. The combined effect may also bring out polytypism in LiZnN.

Focussing on transport properties, the most promising candidate to emerge out was LiZnSb. The benefits of LiZnSb were twofold. First, both cubic and hexagonal *n*-

LiZnSb had impressive power factor and thus ZT values at 700 K. Since the amount of pressure required for the phase transition was not that great (4.3 GPa), there may be chances of phase transition on exposure to realistic robust application conditions. This is where the significance of high efficiency of the two phases comes into play by ensuring that the performance of the device may not be affected much even when the symmetry changes its color (cubic-hexagonal).

Secondly, as stated by White et al., the constituent elements and low-temperature synthesis make LiZnSb promising from both a cost and a toxicity perspective. Standing on the shoulders of LiZnSb, the power factor and ZT values of hexagonal n-LiZnP and n-LiZnAs were equally promising. The improved values of transport coefficients in hexagonal variants of prevailing cubic LiZnP and LiZnAs were the best instances of polytypism induced thermoelectric performance in LiZnX systems, the prime interest of the chapter. The current research was limited by two factors, constant relaxation time and estimated lattice thermal conductivity. The relaxation time may vary depending on the actual dopants, temperature, and doping levels. On similar grounds, the values of κ_l are expected to change. However, as discussed in preceding section, the chosen relaxation time and lattice thermal conductivity are in light of previous theoretical and experimental evidence. Also, the values are on a conservative side and not unreasonably optimistic. It is believed that inculcating the exact values would further improve the proposed results.

Further, it cannot be denied that theoretical predictions are way too easier than experimental realization. To give an illustration, in response to Madsen's prediction of better thermoelectric properties in LiZnSb on n-type doping, Toberer's experimental investigation was limited to p-type LiZnSb samples. The experimentalists may face challenges in synthesizing ordered compositions with controlled doping levels. However, with recent advances in synthesis techniques, the experimental realization of aforementioned LiZnX systems with optimal doping levels is hopeful.

In conclusion, utilizing *ab initio* approach, this chapter gave an account of polytypism and its impact on thermoelectric properties in LiZnX (X = N, P, As, Sb, and Bi) systems. In addition to LiZnSb, it was found that LiZnBi was most favorable of polytypic behavior whereas the phenomenon could be driven by pressure to attain hexagonal variants of cubic LiZnP and LiZnAs. The improved transport properties on cubic to hexagonal phase transition validates that polytypism may affect better thermoelectric performance. The ZT values in cubic and hexagonal LiZnSb at 700 K on n-type doping were highly impressive, i.e 1.27 and 1.95, respectively. The other promising values of ZT at 700 K were 1.96 and 1.45 of hexagonal LiZnP and LiZnAs, respectively, on n-type doping. These findings would

serve as a base for experimentalists to explore this new potential class of thermoelectric materials.

Concluding Remarks

Utilizing *ab initio* approach, semi-classical Boltzmann transport theory, and constant relaxation time approach, systematic investigation of the ground state properties, structural stability, electronic features (band structure and DOSs), and thermal and electrical transport properties of cobalt-based (CoVSn, CoNbSn, CoTaSn, CoCrIn, CoMoIn, and CoWIn), iron-based (FeTaSb and FeMnTiSb) Heusler alloys, and a special derivative of half-Heusler alloys, LiZnX (X = N, P, As, Sb, and Bi) family, has been carried out. Remarkably, LiZnX family exhibited the polytypism phenomenon in cubic and hexagonal symmetry. The electronic structure calculations revealed the semiconducting behavior of all the cobalt-based systems (except CoCrIn), iron-based systems in $F\bar{4}3m$ symmetry and LiZnX systems (except LiZnBi) in $F\bar{4}3m$ and $P6_3mc$ symmetry. The cobalt-based systems were found to have better thermoelectric properties than the well-known CoTiSb, on p-type doping. Interestingly, CoNbSn, a previously known n-type half-Heusler alloy, turn out to be more promising in its counterpart i.e. p-type CoNbSn. The maximum figure of merit, ZT, obtained was 0.57 for 0.03 hole-doped CoWIn at 900 K, which is an underestimated value. In case of iron-based systems, the thermoelectric performance of p-type FeTaSb at 1100 K was found of the order of best performing Heusler alloy FeNbSb. Notably, the low-cost FeMnTiSb could be used as both p-type and n-type legs in a thermoelectric module. On the other hand, the polytypism investigations showed some interesting features in the LiZnX family. The last member of the family, LiZnBi, was found to be the most favorable candidate for polytypism. The phenomenon can be achieved in other members of the family by application of hydrostatic or internal pressure. Some of the impressive ZT values obtained at 700 K were 1.27 and 1.95 for cubic and hexagonal n-type LiZnSb, respectively. The other promising values at 700 K were 1.96 and 1.45 of hexagonal n-type LiZnP and LiZnAs, respectively.

Despite the extensive research in Heusler alloys for the past two decades, the highest figure of merit achieved is 1.6 for FeNbSb. However, for practical applications, $ZT \sim$ 3-4 is much needed. Thus, in addition to tailoring the thermoelectric properties of existing Heusler alloys, the search of new potential Heusler alloys becomes crucial. In this direction, the present work can be seen as a step toward the search of new potential Heusler alloys. The proposed systems cannot be regarded as completely hypothetical as the search is centered around well-reported systems. Further, the proposed doping levels are quite pragmatic and could be achieved experimentally. This will help experimentalists to narrow down the target window of new compositions. Certainly, the manifesting challenges for experimentalists are to synthesize the ordered compositions and the vulnerability of these alloys for antisite disorder. Further, one cannot deny the fact that theoretical predictions

are way too easier than experimental realization. However, the interplay between theory and experiment has been fruitful in designing new materials in recent past. Keeping this in mind, this work will hopefully motivate the experimentalists to synthesize the proposed materials for the quest of materials with the better figure of merit.

Bibliography

[1] E. Altenkirch. Über den nutzeffekt der thermosäulen. *Physikalische Zeitschrift*, **10**:560, 1911.

[2] M. Ameri, A. Touia, R. Khenata, Y. A.-Douri, and H. Baltache. Structural and optoelectronic properties of NiTiX and CoVX (X = Sb and Sn) half-Heusler compounds: An ab initio study. *Optik*, **124**:570, 2013.

[3] R. Bacewicz and T. F. Ciszek. Preparation and characterization of some $A^{I}B^{II}C^{V}$ type semiconductors. *Appl. Phys. Lett.*, **52**:1150, 1988.

[4] A. Banik, U. S. Shenoy, S. Anand, U. V. Waghmare, and K. Biswas. Mg alloying in SnTe facilitates valence band convergence and optimizes thermoelectric properties. *Chem. Mater.*, **27**:581, 2015.

[5] A. Beleanu, M. Mondeshki, Q. Juan, F. Casper, C. Felser, and F. Porcher. Systematical, experimental investigations on LiMgZ (Z = P, As, Sb) wide band gap semiconductors. *J. Phys. D: Appl. Phys.*, **44**:475302, 2011.

[6] T. Berry, C. Fu, G. Auffermann, G. H. Fecher, W. Schnelle, F. S.-Sanchez, Y. Yue, H. Liang, and C. Felser. Enhancing thermoelectric performance of TiNiSn half-Heusler compounds via modulation doping. *Chem. Mater.*, **29**:7042, 2017.

[7] S. Bhattacharya and G. K. H. Madsen. A novel p-type half-Heusler from high-throughput transport and defect calculations. *J. Mater. Chem. C*, **4**:11261, 2016.

[8] W. Bi, Y. Meng, R. S. Kumar, A. L. Cornelius, W. W. Tipton, R. G. Hennig, Y. Zhang, C. Chen, and J. S. Schilling. Pressure-induced structural transitions in europium to 92 GPa. *Phys. Rev. B*, **83**:104106, 2011.

[9] F. Birch. Finite elastic strain of cubic crystals. *Phys. Rev.*, **71**:809, 1947.

[10] C. S. Birkel, W. G. Zeier, J. E. Douglas, B. R. Lettiere, C. E. Mills, G. Seward, A. Birkel, M. L. Snedaker, Y. Zhang, G. J. Snyder, T. M. Pollock, R. Seshadri, and G. D. Stucky. Rapid microwave preparation of thermoelectric TiNiSn and TiCoSb half-Heusler compounds. *Chem. Mater.*, **24**:2558, 2012.

[11] K. Biswas, J. He, I. D. Blum, C.-I. Wu, T. P. Hogan, D. N. Seidman, V. P. Dravid, and M. G. Kanatzidis. High-performance bulk thermoelectrics with all-scale hierarchical architectures. *Nature*, **489**:414, 2012.

[12] L. Bjerg, G. K. H. Madsen, and B. B. Iversen. Enhanced thermoelectric properties in zinc antimonides. *Chem. Mater.*, **23**:3907, 2011.

[13] P. Blaha, K. Schwarz, G. K. H. Madsen, D. Kvasnicka, J. Luitz, R. Laskowski, F. Tran, and L. D. Marks. Available at http://susi.theochem.tuwien.ac.at/ (2018/09/14).

[14] M. L. C. Buffon, G. Laurita, N. Verma, L. Lamontagne, L. Ghadbeigi, D. L. Llyod, T. D. Sparks, T. M. Pollock, and R. Seshadri. Enhancement of thermoelectric properties in the Nb-Co-Sn half-Heusler/Heusler system through spontaneous inclusion of a coherent second phase. *J. Appl. Phys.*, **120**:075104, 2016.

[15] D. G. Cahill, S. K. Watson, and R. O. Pohl. Lower limit to the thermal conductivity of disordered crystals. *Phys. Rev. B*, **46**:6131, 1992.

[16] S.-G. Cao, Y. Li, H.-H. Wu, J. Wang, B. Huang, and T.-Y. Zhang. Stress-induced cubic-to-hexagonal phase transformation in perovskite nanothin films. *Nano Lett.*, **17**:5148, 2017.

[17] F. Casper, C. Felser, R. Seshadri, C. P. Sebastian, and R. Pöttgen. Searching for hexagonal analogues of the half-metallic half-Heusler XYZ compounds. *J. Phys. D*, **41**:035002, 2008.

[18] F. Casper, T. Graf, S. Chadov, B. Balke, and C Felser. Half-Heusler compounds: novel materials for energy and spintronic applications. *Semicond. Sci. Technol.*, **27**:063001, 2012.

[19] F. Casper, R. Seshadri, and C. Felser. Semiconducting half-Heusler and LiGaGe structure type compounds. *Phys. Status Solidi A*, **206**:1090, 2009.

[20] P. Chakraborty, L. Cao, and Y. Wang. Ultralow lattice thermal conductivity of the random multilayer structure with lattice imperfections. *Sci. Rep.*, **7**:8134, 2017.

[21] L. Chaput, P. Pècheur, J. Tobola, and H. Scherrer. Transport in doped skutterudites: Ab initio electronic structure calculations. *Phys. Rev. B*, **72**:085126, 2005.

[22] J. R. Chelikowsky and S. G. Louie. *P. B. Allen: Boltzmann theory and resistivity of metals in Quantum Theory of Real Materials*. Kluwer, Boston, 1996.

[23] B. Chen, Z. Deng, W. Li, M. Gao, J. Zhao, G. Zhao, S. Yu, X. Wang, Q. Liu, and C. Jin. Li(Zn,Co,Mn)As: A bulk form diluted magnetic semiconductor with Co and Mn co-doping at Zn sites. *AIP Advances*, **6**:115014, 2016.

[24] S. Chen and Z. Ren. Recent progress of half-Heusler for moderate temperature thermoelectric applications. *Mater. Today*, **16**:387, 2013.

[25] Z.-G. Chen, G. Han, L. Yang, L. Cheng, and J. Zou. Nanostructured thermoelectric materials: Current research and future challenge. *Pro. Nat. Sci-Mater.*, **22**:535, 2012.

[26] D.-Y. Chung, T. Hogan, P. Brazis, M. R.-Lane, C. Kannewurf, M. Bastea, C. Uher, and M. G. Kanatzidis. $CsBi_4Te_6$: A high-performance thermoelectric material for low-temperature applications. *Science*, **287**:1024, 2000.

[27] C. Çoban, K. Çolakoğlu, and Y. Ö. Çiftçi. First principles study of the structural, mechanical, phonon, optical, and thermodynamic properties of half-Heusler (HH) compound NbFeSb. *Phys. Scr.*, **90**:095701, 2015.

[28] S. Cottenier. *Density Functional Theory and the family of (L)APW-methods: a step-by-step introduction.* ISBN 978-90-807215-1-7, Ghent University, Belgium, 2 edition, 2013.

[29] F. A. Cotton and G. Wilkinson. *Advanced Inorganic Chemistry.* Wiley, New York, 3 edition, 1988.

[30] S. R. Culp, S. Joseph Poon, N. Hickman, T. M. Tritt, and J. Blumm. Effect of substitutions on the thermoelectric figure of merit of half-Heusler phases at 800 ^{0}C. *Appl. Phys. Lett.*, **88**:042106, 2006.

[31] S. R. Culp, W. Simonson, S. J. Poon, V. Ponnambalam, J. Edwards, and T. M. Tritt. (Zr,Hf)Co(Sb,Sn) half-Heusler phases as high-temperature ($>$ 700 ^{0}C) p-type thermoelectric materials. *Appl. Phys. Lett.*, **93**:022105, 2008.

[32] M. Cutler and M. F. Mott. Observation of anderson localization in an electron gas. *Phys. Rev.*, **181**:1336, 1969.

[33] S. Das, R. Chetty, K. Wojciechowski, S. Suwas, and R. C. Mallik. Thermoelectric properties of Sn doped BiCuSeO. *Appl. Surf. Sci.*, **418**:238, 2017.

[34] A. Date, A. Date, C. Dixon, and A. Akbarzadeh. Progress of thermoelectric power generation systems: Prospect for small to medium scale power generation. *Renew. Sustain. Energy Rev.*, **33**:371, 2014.

[35] C. Dhital, M. A. Khan, M. Saghayezhian, W. A. Phelan, D. P. Young, R. Y. Jin, and J. F. DiTusa. Effect of negative chemical pressure on the prototypical itinerant magnet MnSi. *Phys. Rev. B*, **95**:024407, 2017.

[36] P. A. M. Dirac. Note on exchange phenomena in the thomas atom. *Proc. Cambridge Phil. Soc.*, **26**:376, 1930.

[37] J.-M. Dubious, E. B.-Ferre, and M. Feuerbacher. *Complex Metallic Alloys: Fundamentals and Applications.* Wiley, New York, 2010.

[38] Z. H. Dughaish. Lead telluride as a thermoelectric material for thermoelectric power generation. *Physica B*, **322**:205, 2002.

[39] R. S. Elliott, N. Triantafyllidis, and J. A. Shaw. Stability of crystalline solids–I: Continuum and atomic lattice considerations. *J. Mech. Phys. Solids*, **54**:161, 2006.

[40] T. Fang, S. Zheng, H. Chen, H. Cheng, L. Wang, and P. Zhang. Electronic structure and thermoelectric properties of p-type half-Heusler compound NbFeSb: a first-principles study. *RSC Adv.*, **6**:10507, 2016.

[41] T. Fang, S. Zheng, L. Yan T. Zhou, and P. Zhang. Computational prediction of high thermoelectric performance in p-type half-Heusler compounds with low band effective mass. *Phys. Chem. Chem. Phys.*, **19**:4411, 2017.

[42] G. H. Fecher, H. C. Kandpal, S. Wurmehl, C. Felser, and G. Schönhense. Slater-Pauling rule and Curie temperature of Co_2-based Heusler compounds. *J. Appl. Phys.*, **99**:08J106, 2006.

[43] C. Felser, G. H. Fecher, and B. Balke. Spintronics: A challenge for materials science and solid-state chemistry. *Angew. Chem. Int. Ed.*, **46**:668, 2007.

[44] M. Fratini, R. Caivano, A. Puri, A. Ricci, Z.-A. Ren, X.-L. Dong, J. Yang, W. Lu, Z.-X. Zhao, L. Barba, G. Arrighetti, M. Polentarutti, and A. Bianconi. The effect of internal pressure on the tetragonal to monoclinic structural phase transition in ReOFeAs: the case of NdOFeAs. *Supercond. Sci. Technol.*, **21**:092002, 2008.

[45] C. Fu, S. Bai, Y. Liu, Y. Tang, L. Chen, X. Zhao, and T. Zhu. Realizing high figure of merit in heavy-band p-type half-Heusler thermoelectric materials. *Nat. Commun.*, **6**:8144, 2015.

[46] C. Fu, H. Wu, Y. Liu, J. He, X. Zhao, and T. Zhu. Enhancing the figure of merit of heavy-band thermoelectric materials through hierarchical phonon scattering. *Adv. Sci.*, **3**:1600035, 2016.

[47] C. Fu, H. Xie, Y. Liu, T. J. Zhu, J. Xie, and X. B. Zhao. Thermoelectric properties of FeVSb half-Heusler compounds by levitation melting and spark plasma sintering. *Intermetallics*, **32**:39, 2013.

[48] C. Fu, H. Xie, T. J. Zhu, J. Xie, and X. B. Zhao. Enhanced phonon scattering by mass and strain field fluctuations in Nb substituted FeVSb half-Heusler thermoelectric materials. *J. Appl. Phys.*, **112**:124915, 2012.

[49] C. Fu, T. Zhu, Y. Liu, H. Xie, and X. Zhao. Band engineering of high performance p-type FeNbSb based half-Heusler thermoelectric materials for figure of merit zT $>$ 1. *Energy Environ. Sci.*, **8**:216, 2015.

[50] C. Fu, T. Zhu, Y. Pei, H. Xie, H. Wang, G. J. Snyder, Y. Liu, Y. Liu, and X. Zhao. High band degeneracy contributes to high thermoelectric performance in p-type half-Heusler compounds. *Adv. Energy Mater.*, **4**:1400600, 2014.

[51] G. Fugallo, M. Lazzeri, L. Paulatto, and F. Mauri. Ab initio variational approach for evaluating lattice thermal conductivity. *Phys. Rev. B*, **88**:045430, 2013.

[52] I. Galanakis, P. H. Dederichs, and N. Papanikolaou. Origin and properties of the gap in the half-ferromagnetic Heusler alloys. *Phys. Rev. B*, **66**:174429, 2002.

[53] I. Galanakis, Ph Mavropoulos, and P. H. Dederichs. Electronic structure and Slater-Pauling behaviour in half-metallic Heusler alloys calculated from first principles. *J. Phys. D*, **39**:765, 2006.

[54] R. Gautier, X. Zhang, L. Hu, L. Yu, Y. Lin, T. O. L. Sunde, D. Chon, K. R. Poeppelmeier, and A. Zunger. Prediction and accelerated laboratory discovery of previously unknown 18-electron ABX compounds. *Nat. Chem.*, **7**:308, 2015.

[55] S. Ghosh, A. Bisht, A. Karati, G. Rogl, P. Rogl, B. S. Murty, S. Suwas, and R. C. Mallik. Thermoelectric properties of Co_4Sb_{12} with Bi_2Te_3 nanoinclusions. *J. Phys.: Condens. Matter*, **30**:095701, 2018.

[56] P. Giannozzi. Available at https://www.quantum-espresso.org/ (2018/09/14).

[57] P. Giannozzi, O. Andreussi, T. Brumme, O. Bunau, M. Buongiorno Nardelli, M. Calandra, R. Car, C. Cavazzoni, D. Ceresoli, M. Cococcioni, N. Colonna, I. Carnimeo, A. Dal Corso, S. de Gironcoli, P. Delugas, R. A. DiStasio Jr., A. Ferretti, A. Floris, G. Fratesi, G. Fugallo, R. Gebauer, U. Gerstmann, F. Giustino, T. Gorni, J. Jia, M. Kawamura, H.-Y Ko, A. Kokalj, E. Käçäkbenli, M. Lazzeri, M. Marsili, N. Marzari, F. Mauri, N. L. Nguyen, H.-V Nguyen, A. Otero de-la Roza, L. Paulatto, S. Poncè, D. Rocca, R. Sabatini, B. Santra, M. Schlipf, and A. P. Seitsonen. Advanced capabilities for materials modelling with Quantum ESPRESSO. *Journal of Physics: Condensed Matter*, **29**:465901, 2017.

[58] P. Giannozzi, S. Baroni, N. Bonini, M. Calandra, R. Car, C. Cavazzoni, D. Ceresoli, G. L. Chiarotti, M. Cococcioni, I. Dabo, A. Dal Corso, S. de Gironcoli, S. Fabris, G. Fratesi, R. Gebauer, U. Gerstmann, C. Gougoussis, A. Kokalj, M. Lazzeri, L. Martin-Samos, N. Marzari, F. Mauri, R. Mazzarello, S. Paolini, A. Pasquarello, L. Paulatto, C. Sbraccia, S. Scandolo, G. Sclauzero, A. P. Seitsonen, A. Smogunov, P. Umari, and R. M. Wentzcovitch. QUANTUM ESPRESSO: a modular and open-source software project for quantum simulations of materials. *Journal of Physics: Condensed Matter*, **21**:395502, 2009.

[59] T. Graf, C. Felser, and S. S. P. Parkin. Simple rules for the understanding of Heusler compounds. *Progr. Solid State Chem.*, **39**:1, 2011.

[60] V. K. Gudelli, V. Kanchana, G. Vaitheeswaran, A. Svane, and N. E. Christensen. Thermoelectric properties of chalcopyrite type $CuGaTe_2$ and chalcostibite $CuSbS_2$. *J. Appl. Phys.*, **114**:223707, 2013.

[61] J. He and T. M. Tritt. Advances in thermoelectric materials research: Looking back and moving forward. *Science*, **357**:1369, 2017.

[62] R. He, L. Huang, Y. Wang, G. Samsonidze, B. Kozinsky, Q. Zhang, and Z. Ren. Enhanced thermoelectric properties of n-type NbCoSn half-Heusler by improving phase purity. *APL Mater.*, **4**:104804, 2016.

[63] R. He, H. S. Kim, Y. Lan, D. Wang, S. Chen, and Z. Ren. Investigating the thermoelectric properties of p-type half-Heusler $Hf_x(ZrTi)_{1-x}$ $CoSb_{0.8}Sn_{0.2}$ by reducing Hf concentration for power generation. *RSC Adv.*, **4**:64711, 2014.

[64] O. Hellman, I. A. Abrikosov, and S. I. Simak. Lattice dynamics of anharmonic solids from first principles. *Phys. Rev. B*, **84**:180301, 2011.

[65] J. P. Heremans, V. Jovovic, E. S. Toberer, A. Saramat, K. Kurosaki, A. Charoenphakdee, S. Yamanaka, and G. J. Snyder. Enhancement of thermoelectric efficiency in PbTe by distortion of the electronic density of states. *Science*, **321**:554, 2008.

[66] M. Hichour, D. Rached, R. Khenata, M. Rabah, M. Merabet, A. H. Reshak, S. B. Omran, and R. Ahmed. Theoretical investigations of NiTiSn and CoVSn compounds. *J. Phys. Chem. Solids*, **73**:975, 2012.

[67] L. D. Hicks and M. S. Dresselhauss. Effect of quantum-well structures on the thermoelectric figure of merit. *Phys. Rev. B*, **47**:12727, 1993.

[68] L. D. Hicks and M. S. Dresselhauss. Thermoelectric figure of merit of a one-dimensional conductor. *Phys. Rev. B*, **37**:16631, 1993.

[69] A. I. Hochbaum, R. Chen, R. D. Delgado, W. Liang, E. C. Garnett, M. Najarian, A. Majumdar, and P. Yang. Enhanced thermoelectric performance of rough silicon nanowires. *Nature*, **451**:163, 2007.

[70] P. Hohenberg and W. Kohn. Inhomogeneous electron gas. *Phys. Rev.*, **136**:B864, 1964.

[71] A. J. Hong, L. Li, R. He, J. J. Gong, Z. B. Yan, K. F. Wang, J.-M. Liu, and Z. F. Ren. Full-scale computation for all the thermoelectric property parameters of half-Heusler compounds. *Sci. Rep.*, **6**:22778, 2016.

[72] S. Horiuchi, Y. Okimoto, R. Kumai, and Y. Tokura. Quantum phase transition in organic charge-transfer complexes. *Science*, **299**:229, 2003.

[73] C. E. Housecroft and A. G. Sharpe. *Inorganic Chemistry*. Prentice Hall, Upper Saddle River, New Jersey, 2 edition, 2004.

[74] K. F. Hsu, S. Loo, F. Guo, W. Chen, J. S. Dyck, C. Uher, T. Hogan, E. K. Polychroniadis, and M. G. Kanatzidis. Cubic $AgPb_mSbTe_{2+m}$: Bulk thermoelectric materials with high figure of merit. *Science*, **303**:818, 2004.

[75] L. Huang, Q. Zhang, B. Yuan, X. Lai, X. Yan, and Z. Ren. Recent progress in half-Heusler thermoelectric materials. *Mater. Res. Bull.*, **76**:107, 2016.

[76] A. Huon, D. Lee, A. Herklotz, M. R. Fitzsimmons, H. N. Lee, and S. J. May. Effect of chemical pressure on the electronic phase transition in $Ca_{1-x}Sr_xMn_7O_{12}$ films. *APL Mater.*, **5**:096105, 2017.

[77] F. Jensen. *Intoduction to Computational Chemistry*. Wiley, England, 2010.

[78] H. Jiang, W. Wang, C. Zhang, X.-N. Hu, G.-H. Zhong, X.-Q. Lu, and Y.-H. Su. Phase transitions of actinium dihydride: Pressure-induced charge transfer driving effect. *Int. J. Hydrogen Energy*, **39**:15827, 2014.

[79] L. Jodin, J. Tobola, P. Pecheur, H. Scherrer, and S. Kaprzyk. Effect of substitutions and defects in half-Heusler FeVSb studied by electron transport measurements and KKR-CPA electronic structure calculations. *Phys. Rev. B*, **70**:184207, 2004.

[80] G. Joshi, R. He, M. Engber, G. Samsonidze, T. Pantha, E. Dahal, K. Dahal, J. Yang, Y. Lan, B. Kozinsky, and Z. Ren. NbFeSb-based p-type half-Heuslers for power generation applications. *Energy Environ. Sci.*, **7**:4070, 2014.

[81] G. Joshi, X. Yan, H. Z. Wang, W. S. Liu, G. Chen, and Z. F. Ren. Enhancement in thermoelectric figure-of-merit of an n-type half-Heusler compound by the nanocomposite approach. *Adv. Energy Mater.*, **1**:643, 2011.

[82] S. Kacimi, H. Mehnane, and A. Zaoui. I-II-V and I-III-IV half-Heusler compounds for optoelectronic applications: Comparative ab initio study. *J. Alloys Compd.*, **587**:451, 2014.

[83] F. Kalarasse and B. Bennecer. Optical properties of the filled tetrahedral semiconductors LiZnX (X = N, P, and As). *J. Phys. Chem. Solids*, **67**:1850, 2006.

[84] FIZ Karlsruhe. Inorganic crystal structure database (ICSD). Available at http://www2.fiz-karlsruhe.de/icsd_home.html (2018/09/14).

[85] Y. Kimura, T. Tamura, and Y. Kita. Thermoelectric properties of directionally solidified half-Heusler compound NbCoSn alloys. *Appl. Phys. Lett.*, **92**:012105, 08.

[86] K. Kishimoto and T. Koyanagi. Preparation and thermal conductivities of filled tetrahedral $Li_xIn_{1-x}Zn_xSb$ and the related compounds. *J. Alloys Compd.*, **463**:89, 2008.

[87] W. Kohn and L. J. Sham. Self-consistent equations including exchange and correlation effects. *Phys. Rev.*, **140**:A1133, 1965.

[88] J. Kübler. First principle theory of metallic magnetism. *Physica B+C*, **127**:257, 1984.

[89] K. Kuriyama, T. Kato, T. Kato, and H. Matsuno. Growth and photoluminescence properties of the filled tetrahedral semiconductor LiZnAs. *J. Cryst. Growth*, **166**:631, 1996.

[90] K. Kuriyama, T. Kato, and T. Tanaka. Optical band gap of the filled tetrahedral semiconductor LiZnN. *Phys. Rev. B*, **49**:4511, 1994.

[91] K. Kuriyama and T. Katoh. Optical band gap of the filled tetrahedral semiconductor LiZnP. *Phys. Rev. B*, **37**:7140, 1988.

[92] K. Kuriyama, T. Katoh, and N. Mineo. Crystal growth and characterization of the filled tetrahedral semiconductor LiZnP. *J. Cryst. Growth*, **108**:37, 1991.

[93] K. Kuriyama and F. Nakamura. Electrical transport properties and crystal structure of LiZnAs. *Phys. Rev. B*, **36**:4439, 1987.

[94] K. Kuriyama, R. Taguchi, K. Kushida, and K. Ushiyama. Growth and band gap of the filled tetrahedral semiconductor LiZnN. *J. Cryst. Growth*, **198**:802, 1999.

[95] M.-S. Lee, F. P. Poudeu, and S. D. Mahanti. Electronic structure and thermoelectric properties of Sb-based semiconducting half-Heusler compounds. *Phys. Rev. B*, **83**:085204, 2011.

[96] W. Li, G. Yang, and J. Zhang. Optimization of the thermoelectric properties of FeNbSb-based half-Heusler materials. *J. Phys. D*, **49**:195601, 2016.

[97] W. Liu, H. S. Kim, Q. Jie, and Z. Ren. Importance of high power factor in thermoelectric materials for power generation application: A perspective. *Scr. Mater.*, **111**:3, 2016.

[98] C. S. Lue, Y. Öner, D. G. Naugle, and Jr. J. H. Ross. Magnetism of new semi-Heusler compounds FeVSn and CoVSn. *IEEE Trans. Magn.*, **37**:2138, 2001.

[99] G. K. H. Madsen. Automated search for new thermoelectric materials: The case of LiZnSb. *J. Am. Chem. Soc.*, **128**:12140, 2006.

[100] G. K. H. Madsen and D. J. Singh. BoltzTraP. a code for calculating band-structure dependent quantities. *Comput. Phys. Commun.*, **175**:67, 2006.

[101] A. Majumdar. Thermoelectricity in semiconductor nanostructures. *Science*, **303**:777, 2004.

[102] R. C. Mallik, E. Mueller, and I.-H. Kim. Thermoelectric properties of indium filled and germanium doped Co_4Sb_{12} skutterudites. *J. Appl. Phys.*, **111**:023708, 2012.

[103] F. J. Manjón and D. Errandonea. Pressure-induced structural phase transitions in materials and earth sciences. *Phys. Status Solidi B*, **246**:9, 2009.

[104] G. Melnyk, E. Bauer, P. Rogl, R. Skolozdra, and E. Seidl. Thermoelectric properties of ternary transition metal antimonides. *J. Alloys and Compd.*, **296**:235, 2000.

[105] B. W. Montag, M. A. Reichenberger, M. Sunder, P. B. Ugorowski, K. A. Nelson, and D. S. McGregor. Bulk crystal growth, and high-resolution X-ray diffraction results of LiZnP semiconductor material. *J. Cryst. Growth*, **419**:143, 2015.

[106] Y. Noda, M. Shimada, and M. Koizumi. Synthesis of high-pressure phases of VCoSb and VFeSb with a Ni_2In ($B8_2$) type structure. *Inorganic Chemistry*, **18**:3245, 1979.

[107] S. Ouardi, G. H. Fecher, C. Felser, M. Schwall, S. S. Naghavi, A. Gloskovskii, B. Balke, J. Hamrle, K. Postava, J. Pištora, S. Ueda, and K. Kobayashi. Electronic structure and optical, mechanical, and transport properties of the pure, electron-doped, and hole-doped Heusler compound CoTiSb. *Phys. Rev. B*, **86**:045116, 2012.

[108] K. Özdoğan, E. Şaşioğlu, and I. Galanakis. Slater-Pauling behavior in LiMgPdSn-type multifunctional quaternary Heusler materials: Half-metallicity, spin-gapless and magnetic semiconductors. *J. Appl. Phys.*, **113**:193903, 2013.

[109] D. Parker and D. J. Singh. High-temperature thermoelectric performance of heavily doped PbSe. *Phys. Rev. B*, **82**:035204, 2010.

[110] L. Paulatto, F. Mauri, and M. Lazzeri. Anharmonic properties from a generalized third-order ab initio approach: Theory and applications to graphite and graphene. *Phys. Rev. B*, **87**:214303, 2013.

[111] J. C. A. Peltier. Nouvelles expèriences sur la caloricitè des courants èlectrique. *Ann. Chim. et Phys.*, **56**:371, 1834.

[112] J. P. Perdew, K. Burke, and M. Ernzerhof. Generalized gradient approximation made simple. *Phys. Rev. Lett.*, **77**:3865, 1996.

[113] J. P. Perdew, A. Ruzsinszky, G. I. Csonka, O. A. Vydrov, G. E. Scuseria, L. A. Constantin, X. Zhou, and K. Burke. Restoring the density-gradient expansion for exchange in solids and surfaces. *Phys. Rev. Lett.*, **100**:136406, 2008.

[114] P. Pichanusakorn and P. Bandaru. Nanostructured thermoelectrics. *Mater. Sci. Eng. R*, **67**:19, 2010.

[115] S. J. Poon, D. Wu, S. Zhu, W. Xie, T. M. Tritt, P. Thomas, and R. Venkatasubramanian. Half-Heusler phases and nanocomposites as emerging high-ZT thermoelectric materials. *J. Mater. Res.*, **26**:2795, 2011.

[116] P. Qiu, X. Huang, X. Chen, and L. Chen. Enhanced thermoelectric performance by the combination of alloying and doping in TiCoSb-based half-Heusler compounds. *J. Appl. Phys.*, **106**:103703, 2009.

[117] P. Roy, V. Waghmare, and T. Maiti. Environmentally friendly $Ba_xSr_{2-x}TiFeO_6$ double perovskite with enhanced thermopower for high temperature thermoelectric power generation. *RSC Adv.*, **6**:54636, 2008.

[118] B. Saha, T. D. Sands, and U. V. Waghmare. Thermoelectric properties of HfN/ScN metal/semiconductor superlattices: a first-principles study. *J. Phys.: Condens. Matter*, **24**:415303, 2012.

[119] S. Sakurada and N. Shutoh. Effect of Ti substitution on the thermoelectric properties of (Zr,Hf)NiSn half-Heusler compounds. *Appl. Phys. Lett.*, **86**:082105, 2005.

[120] M. Samanta and K. Biswas. Low thermal conductivity and high thermoelectric performance in $(GeTe)_{1-2x}(GeSe)_x(GeS)_x$: Competition between solid solution and phase separation. *J. Am. Chem. Soc.*, **139**:9382, 2017.

[121] G. Samsonidze and B. Kozinsky. Materials for thermoelectric energy conversion. *International patent application WO 2015/130364 A2*, 2015.

[122] M. Saxena and T. Maiti. Metal-like electrical conductivity in La_xSr_{2-x} $TiMoO_6$ oxides for high temperature thermoelectric power generation. *Dalton Trans.*, **46**:5872, 2017.

[123] T. J. Seebeck. Ueber die magnetische polarisation der metalle und erze durch temperatur-differenz. *Ann. Phys.*, **82**:133, 1826.

[124] T. Sekimoto, K. Kurosaki, H. Muta, and S. Yamanaka. Thermoelectric and thermophysical properties of TiCoSb, ZrCoSb, HfCoSb prepared by SPS. In *24^{th} International Conference on Thermoelectrics (ICT)*, page 335. IEEE, Clemson, SC, USA, USA, 2005.

[125] T. Sekimoto, K. Kurosaki, H. Muta, and S. Yamanaka. Thermoelectric properties of Sn-doped TiCoSb half-Heusler compounds. *J. Alloys Compd.*, **407**:326, 2006.

[126] H. Sevinçli, C. Sevik, T. Çağin, and G. Cuniberti. A bottom-up route to enhance thermoelectric figures of merit in graphene nanoribbons. *Sci. Re.*, **3**:1228, 2013.

[127] H. Shi, W. Ming, D. S. Parker, M. H. Du, and D. J. Singh. Prospective high thermoelectric performance of the heavily p-doped half-Heusler compound CoVSn. *Phys. Rev. B*, **95**:195207, 2017.

[128] G. A. Slack. Some new materials for thermoelectric cooling. In *Proceedings of the 1992 1st National Thermogenic Cooler Conference*, page 171. Unpublished, 1992.

[129] G. A. Slack. *CRC Handbook of Thermoelectrics*. CRC Press, Boca Raton, Florida, 1 edition, 1995.

[130] G. J. Snyder. Available at http://www.thermoelectrics.caltech.edu/thermoelectrics/history.html (2018/09/14).

[131] G. J. Snyder and E. S. Toberer. Complex thermoelectric materials. *Nature*, **7**:105, 2008.

[132] A. Tavassoli, F. Failamani, A. Grytsiv, G. Rogl, P. Heinrich, H. Muller, E. Bauer, M. Zehetbauer, and P. Rogl. On the half-Heusler compounds Nb_{1-x} (Ti,Zr,Hf)$_x$FeSb: Phase relations, thermoelectric properties at low and high temperature, and mechanical properties. *Acta Mater.*, **135**:263, 2017.

[133] W. Thomson. On the dynamical theory of heat. *R. Soc. Edinburgh: Earth Sci.*, **3**:91, 1851.

[134] C. Tiburtius and H.-U. Schuster. LiBeSb and LiZnBi, ternary compounds with a wurtzit-type lattice. *Z. Naturforsch.*, **33**:35, 1977.

[135] E. S. Toberer, A. F. May, C. J. Scanlon, and G. J. Snyder. Thermoelectric properties of p-type LiZnSb: Assessment of ab initio calculations. *J. Appl. Phys.*, **105**:063701, 2009.

[136] J. Tobola and J. Pierre. Electronic phase diagram of the XTZ (X=Fe, Co, Ni; T=Ti, V, Zr, Nb, Mn; Z=Sn, Sb) semi-Heusler compounds. *J. Alloys and Compd.*, **296**:243, 2000.

[137] A. Togo and I. Tanaka. First principles phonon calculations in materials science. *Scr. Mater.*, **108**:1, 2015.

[138] G. C. Trigunayat. A survey of the phenomenon of polytypism in crystals. *Solid State Ionics*, **48**:3, 1991.

[139] T. M. Tritt. Thermoelectric phenomena, materials, and applications. *Annu. Rev. Mater. Res.*, **41**:433, 2011.

[140] M. V. Vedernikov and E. K. Iordanishvili. A. F. Ioffe and origin of modern semiconductor thermoelectric energy conversion. *17th Int. Conf. on Thermoelectrics*, **1**:37, 1998.

[141] M. A. White, G. J. Miller, and J. Vela. Polytypism and unique site preference in LiZnSb: A superior thermoelectric reveals its true colors. *J. Am. Chem. Soc.*, **138**:14574, 2016.

[142] M. A. White, M. J. Thompson, G. J. Miller, and J. Vela. Got LiZnP? Solution phase synthesis of filled tetrahedral semiconductors in the nanoregime. *Chem. Commun.*, **52**:3497, 2016.

[143] L. Wollmann, A. K. Nayak, S. S. P. Parkin, and C. Felser. Heusler 4.0: Tunable materials. *Annu. Rev. Mater. Res.*, **47**:247, 2017.

[144] T. Wu, W. Jiang, X. Li, S. Bai, S. Liufu, and L. Chen. Effects of Ge doping on the thermoelectric properties of TiCoSb-based p-type half-Heusler compounds. *J. Alloys Compd.*, **467**:590, 2009.

[145] T. Wu, W. Jiang, X. Li, Y. Zhou, and L. Chen. Thermoelectric properties of p-type Fe-doped TiCoSb half-Heusler compounds. *J. Appl. Phys.*, **102**:103705, 2007.

[146] F. Xiao, C. Hangarter, B. Yoo, Y. Rheem, K.-H. Lee, and N. V. Myung. Recent progress in electrodeposition of thermoelectric thin films and nanostructures. *Electrochim. Acta*, **53**:8103, 2008.

[147] H.-H. Xie, C. Yu, T.-J. Zhu, C.-G. Fu, G. J. Snyder, and X.-B. Zhao. Increased electrical conductivity in fine-grained (Zr,Hf)NiSn based thermoelectric materials with nanoscale precipitates. *Appl. Phys. Lett.*, **100**:254104, 2012.

[148] W. Xie, A. Weidenkaff, X. Tang, Q. Zhang, J. Poon, and T. M. Tritt. Recent advances in nanostructured thermoelectric half-Heusler compounds. *Nanomaterials*, **2**:379, 2012.

[149] M. K. Yadav and B. Sanyal. First principles study of thermoelectric properties of Li-based half-Heusler alloys. *J. Alloys Compd.*, **622**:388, 2015.

[150] X. Yan, W. Liu, H. Wang, S. Chen, J. Shiomi, K. Esfarjani, H. Wang, D. Wang, G. Chen, and Z. Ren. Stronger phonon scattering by larger differences in atomic mass and size in p-type half-Heuslers $Hf_{1-x}Ti_xCoSb_{0.8}Sn_{0.2}$. *Energy Environ. Sci.*, **5**:7543, 2012.

[151] G. Yang, J. Yang, Y. Yan, and Y. Wang. The relationship between the electronic structure and thermoelectric properties of Zintl compounds $M_2Zn_5As_4$ (M = K, Rb). *Phys. Chem. Chem. Phys.*, **16**:5661, 2014.

[152] J. Yang, H. Li, T. Wu, W. Zhang, L. Chen, and J. Yang. Evaluation of half-Heusler compounds as thermoelectric materials based on the calculated electrical transport properties. *Adv. Funct. Mater.*, **18**:2880, 2008.

[153] J. Yang, L. Xi, W. Qiu, L. Wu, X. Shi, L. Chen, J. Yang, W. Zhang, C. Uher, and D. J. Singh. On the tuning of electrical and thermal transport in thermoelectrics: an integrated theory-experiment perspective. *npj comput. mater.*, **2**:15015, 2016.

[154] D. P. Young, P. Khalifah, R. J. Cava, and A. P. Ramirez. Thermoelectric properties of pure and doped FeMSb (M=V,Nb). *J. Appl. Phys.*, **87**:317, 2000.

[155] C. Yu, T.-J. Zhu, R.-Z. Shi, Y. Zhang, X.-B. Zhao, and J. He. High-performance half-Heusler thermoelectric materials $Hf_{1-x}Zr_xNiSn_{1-y}Sb_y$ prepared by levitation melting and spark plasma sintering. *Acta Mater.*, **57**:2757, 2009.

[156] J. Yu, C. Fu, Y. Liu, K. Xia, U. Aydemir, T. C. Chasapis, G. J. Snyder, X. Zhao, and T. Zhu. Unique role of refractory Ta alloying in enhancing the figure of merit of NbFeSb thermoelectric materials. *Adv. Energy Mater.*, **8**:1701313, 2018.

[157] A. Zakutayev, X. Zhang, A. Nagaraja, L. Yu, S. Lany, T. O. Mason, D. S. Ginley, and A. Zunger. Theoretical prediction and experimental realization of new stable inorganic materials using the inverse design approach. *J. Am. Chem. Soc.*, **135**:10048, 2013.

[158] M. Zeeshan, H. K. Singh, J. van den Brink, and H. C. Kandpal. Ab initio design of new cobalt-based half-Heusler materials for thermoelectric applications. *Phys. Rev. Materials*, **1**:075407, 2017.

[159] M. Zeeshan, J. van den Brink, and H. C. Kandpal. Hole-doped cobalt-based Heusler phases as prospective high-performance high-temperature thermoelectrics. *Phys. Rev. Materials*, **1**:074401, 2017.

[160] G. Zhang, Q. Yu, and X. Li. Wet chemical synthesis and thermoelectric properties of V-VI one- and two-dimensional nanostructures. *Dalton Trans.*, **39**:993, 2010.

[161] L. Zhang, M.-H. Du, and D. J. Singh. Zintl-phase compounds with $SnSb_4$ tetrahedral anions: Electronic structure and thermoelectric properties. *Phys. Rev. B*, **81**:075117, 2010.

[162] X. Zhang, Y. Wang, Y. Yan, C. Wang, G. Zhang, Z. Cheng, F. Ren, H. Deng, and J. Zhang. Origin of high thermoelectric performance of $FeNb_1 - xZr/Hf_xSb_{1-y}Sn_y$ alloys: A first-principles study. *Sci. Rep.*, **6**:33120, 2016.

[163] L. D. Zhao, S. H. Lo, Y. S. Zhang, H. Sun, G. J. Tan, C. Uher, C. Wolverton, V. P. Dravid, and M. G. Kanatzidis. Ultralow thermal conductivity and high thermoelectric figure of merit in SnSe crystals. *Nature*, **508**:373, 2014.

[164] J.-C. Zheng. Recent advances on thermoelectric materials. *Front. Phys. China*, **3**:269, 2008.

[165] M. Zhou, L. Chen, C. Feng, D. Wang, and J.-F. Li. Moderate-temperature thermoelectric properties of TiCoSb-based half-Heusler compounds $Ti_{1-x}Ta_xCoSb$. *J. Appl. Phys.*, **101**:113714, 2007.

[166] M. Zhou, C. Feng, L. Chen, and X. Huang. Effects of partial substitution of Co by Ni on the high-temperature thermoelectric properties of TiCoSb-based half-Heusler compounds. *J. Alloys Compd.*, **391**:194, 2005.

[167] T. Zhu, C. Fu, H. Xie, Y. Liu, and X. Zhao. High efficiency half-Heusler thermoelectric materials for energy harvesting. *Adv. Energy Mater.*, **5**:1500588, 2015.

[168] T. J. Zhu, C. G. Fu, H. H. Xie, Y. T. Liu, B. Feng, J. Xie, and X. B. Zhao. Lattice thermal conductivity and spectral phonon scattering in FeVSb-based half-Heusler compounds. *EPL*, **104**:46003, 2013.

[169] J. M. Ziman. *Electrons and Phonons*. Oxford University Press, London, 1960.

[170] M. Zou, J.-F. Li, and T. Kita. Thermoelectric properties of fine-grained FeVSb half-Heusler alloys tuned to p-type by substituting vanadium with titanium. *J. Solid State Chem.*, **198**:125, 2013.